UNIVERSIDADE Ð COIMBRA

Francisco Gameiro Casalinho

Probing the vacuum with di-Higgs production at the FCC

September 2023

Francisco Gameiro Casalinho

Probing the vacuum with di-Higgs production at the FCC

Master degree in Nuclear and Particle Physics

Master Dissertation submitted to the University of Coimbra

Advised by Professor Doctor José Ricardo Morais Silva Gonçalo and Professor Doctor Filipe Manuel Almeida Veloso

September 2023

Acknowledgements

Abstract

Since its discovery in 2012, the Higgs boson has been a significant focus of study in Physics. This boson contains the key to a better understanding of the electroweak symmetry-breaking mechanism. This key is known as the triple Higgs boson coupling. The LHC has sought to measure this property of the Higgs boson through direct measurement, which means, by studying the production of pairs of Higgs bosons, it is possible to have direct access to this constant. Unfortunately, producing a pair of Higgs bosons in a hadron accelerator is a significant challenge and is beyond the reach of this hadron accelerator.

The construction of a circular accelerator with ~ 100 km in perimeter in the Geneva area is being analyzed by CERN. The future lepton accelerator (FCC-ee) is expected to operate at 91, 161, 240, 350/365 GeV to study the Z, W, and Higgs bosons and top-quark particles with high precision. At 240 and 365 GeV, FCC-ee will have as its main focus the study of the Higgs boson acting at an integrated luminosity of 5.0 and 1.5 ab^{-1}, respectively.

This work focuses on the study of improving the accuracy of the triple coupling of the Higgs boson. With this in mind, a direct search was first made where pairs of Higgs bosons were used for the measurement of these coupling. After this approach was shown to be inefficient, an indirect search was followed by production samples of simple Higgs production channels. From this approach and restrict the regions where the m$_{recoil} \in 3\sigma$ and the MET < 40 GeV, the signal significance is maximized and the FCC-ee will be able to observe the quantum effects from the loop process in E$_{b-jets}$ and M$_{b-jets}$ at 2.3σ and 1.5σ at 240 and 365 GeV with an integrated luminosity of 5.0ab^{-1} and 1.5ab^{-1}, respectively.

Keywords

Resumo

Desde da sua descoberta em 2012, o bosão de Higgs tem sido um dos principais focos de estudo na física. Neste bosão está contida a chave para um melhor entendimento sobre o mecanismo de quebra de simetria eletrofraca. Esta chave é conhecida como o acoplamento triplo do bosão de Higgs.

O LHC tem procurado medir esta propriedade do bosão de Higgs através da sua medição direta, ou seja, ao se estudar a produção de pares de bosões de Higgs, é possível ter um acesso direto a esta constante. Infelizmente, a produção de um par de bosões de Higgs num acelerador hadronico é um grande desafio ficando fora do alcance deste acelerador de hadrões.

A construção de um acelerador circular com $\sim$ 100 km de perímetro na área de Genebra está a ser analisada pelo CERN. É esperado que o futuro acelerador leptónico (FCC-ee) funcione a 91, 161, 240, 350/365 GeV para estudar os bosões Z, W e Higgs, e partículas top-quark com alta precisão. A 240 e 365 GeV, o FCC-ee vai ter como principal foco o estudo sobre o bosão de Higgs atuando a uma luminosidade integrada de 5.0 e 1.5 ab^{-1}, respetivamente

Este trabalho tem como objetivo o estudo para melhorar a precisão do acoplamento triplo do bosão de Higgs. Com isso em mente, uma abordagem direta foi feita inicialmente, tendo sido gerados processos com a produção de pares de bosões de Higgs para a medição deste acoplamento. Depois desta abordagem se ter mostrado ineficience, uma abordagem de medição indireta foi seguida onde processos de produção de um bosão de Higgs foram considerados. Seguindo esta abordagem e restringindo as regiões onde a m$_{recoil} \in 3\sigma$ e o MET < 40 GeV, a significância de sinal é maximizada e o FCC-ee conseguirá observar os efeitos quânticos provenientes dos processos de loop em E$_{b-jets}$ e M$_{b-jets}$ com devios padrões de 2.3σ e 1.5σ a 240 e 365 GeV com uma luminosidade integrada de 5.0 e 1.5 ab^{-1}, respetivamente.

Palavras-chave

Future Circular Collider, FCC-ee, pares de bosões de Higgs, produção de bosões de Higgs, acoplamento triplo do bosão de Higgs

Contents

Acronyms

CLD CLIC-Like Detector.

DCH Drift CHamber.

ECAL Electromagnetic Calorimeter.

FCC Future Circular Collider.

HCAL Hadron Calorimeter.

IDEA International Detector for Electron-positron Accelerator.

LEP Large Electron Positron Collider.

LHC Large Hadron Collider.

LO Leading Order.

MG5 MadGraph 5.

MPGD Micro Pattern Gas Detector.

NLO Next Leading Order.

NP New Physics.

OR Overlap Removal.

PDF Parton Distribution Function.

PDG Paticle Data Group.

QCD Quantum Chromodynamics.

QED Quantum Electrodynamics.

SR Synchrotron Radiation.

SSB Spontatneous Symmetry Breaking.

List of Figures

List of Tables

Chapter 1

Introduction

What is physics? Well, physics is the scientific field that searches for the understanding of the universe from cosmic to quantum scale. Of the many possible fields to study in physics, particle physics's primary goal is to discover and understand all of Nature's fundamental particle and their interactions. To do so, models that describe particle dynamics and properties must be created and probed at collider experiments, such as the Large Hadron Collider (LHC).

Since the 1930s, thousands of physicists have developed many theories, resulting in many of them being probed by experiments. This knowledge about particles and their interaction is compacted into one brilliant model, the Standard Model (SM) of particle physics, developed in the early 1970s. The SM describes three fundamental forces at work in the universe: the strong, weak, and electromagnetic, which result from the exchange of force-carrier particles called "bosons". According to this model, all the matter around us is made of elementary particles, divided into leptons and quarks. Each type comprises six particles, split into pairs, or "generations". The last of these twelve particles, the top quark, was discovered in 1995, and with all the force carriers already detected, only one unique particle remained to be discovered. Why is that particle called unique? Well, it is possible to answer this question with a simple word: Mass. The Standard Model calls for all the electroweak force carriers to have the same zero mass to unite the electromagnetic and weak forces into the electroweak force (EW). However, the photon is the only EW carrier with zero mass. According to Ref[1], a mechanism known as the Spontaneous Symmetry Breaking (SSB) in electroweak interactions, or Electroweak Symmetry Breaking (EWSB), can generate the masses that we observe via interaction with a scalar boson known as the Higgs boson. Through Yukawa couplings, the Higgs boson is also responsible for the masses of the fermions. Finally, after a long path, in July 2012, the CMS [2] and ATLAS [3] collaborations at the LHC announced the discovery of a new particle with a mass close to 125 GeV, being revealed to be the Higgs boson. Since this date, many analyses have been carried out to study the properties of this new particle. We have now observed all the particles predicted by SM, so is this the end? Fortunately no. There are many experimental evidences of physics that it cannot explain.

When the current theory is not enough to explain something, the motivation to construct models that extend the SM and still be able to deliver predictions compatible with experimental data is born. However, to develop new results to confirm these new models, we need to keep increasing the precision of our measurements and search for some discrepancies with the SM or hints that some new phenomena are occurring. A

larger integrated luminosity is required to improve the precision, and an increase in the center of mass energy leads to new kinematics regimes.

There are three possible ways to search for New Physics: increase the integrated luminosity, the center of mass energy, or both. CERN plans to upgrade the LHC to its High-Luminosity (HL) version. With a run plan of ten years, the HL-LHC is designed to increase the integrated luminosity by a factor of ten to beyond the LHC's design value and to extend the experimental reach of the LHC. Nevertheless, the CERN future extends to more than just the HL-LHC. A plan to construct a new collider has already begun. The Future Circular Collider (FCC) project is designed to have a total of seven decades for implementation and operation starting in 2033. This project will increase the integrated luminosity and the center of mass energy to a new extreme. The FCC program will be split into three stages depending on the beam particle used. The first stage is an electron-positron collider (FCC-ee), the second is a hadronic collider (FCC-hh), and the last is an electron-hadron collider (FCC-eh).

At the moment, the project focus is on the Future $e^+ e^-$ Circular Collider (FCC-ee), where the feasibility study report needs to be completed in 2025, in time for the next update to the European Strategy for Particle Physics in 2026-2027. The highest priority for the FCC-ee is the Higgs factory, where it is predicted to deliver 10^6 (180 000) events at 240 (365) GeV with an integrated luminosity of 5.0 (1.5) ab^{-1}. With larger luminosities delivered to several detectors, the FCC-ee offers a unique opportunity to improve the precision of previous measurements around the Higgs boson. One of these properties is the self-coupling constant, λ_{hhh}. In the past, the measurement of λ_{hhh} relied on the measurement of the double Higgs production rate that directly depends on its value. However, it was proposed by Ref.[4] to measure this propriety at lepton colliders via the quantum corrections present in single Higgs channels.

The main objective of this work is to improve the measurement precision of λ_{hhh} at the FCC-ee, where di-Higgs production samples with four b-quarks and an electron-positron pair in the final state were used. Due to the expected low cross-section of this process at CM energies between 280-600 GeV, single Higgs boson samples were used. These samples were generated through the MadGraph program at 240 and 365 GeV. The configuration of the Delphes simulator with the IDEA detector, one of the FCC-ee detectors, was used for the detector response. In order to retrieve the signal significance maximized, a optimized analysis through kinematic variables was made. The main goal of this work is to use these optimized samples to search for corrections induced by the Higgs self-coupling constant in single Higgs channels by comparing them with the Tree-level sample.

Chapter 2 reviews the SM of particle physics, outlining its fundamental particles and force carriers, followed by the mathematical description of QED and QCD. The mathematical formulation of the SSB and the Higgs mechanism is also emphasized here. Finally, the interaction between the Higgs boson and the fermions is provided.

In Chapter 3, after a brief discussion about jet algorithms, the Future Colliders in the run for the Higgs physics are discussed. The design, the run plan for the FCC-ee, and the IDEA detector configuration are described. In Chapter 4, we describe the Monte Carlo program used for the sample generation and the detector response.

We produce the samples described in Chapter 5 using those programs, while the analysis strategy and optimization are introduced in Chapter 6.

In Chapter 7, we present and discuss the main results. We focus on increasing the signal significance. To finalize this work, we debate our results in Chapter **??**.

Chapter 2

Standard Model

For many years, humankind has tried to understand the Nature of the Universe: how matter interacts with itself, what matter is made of, and many other questions. Nowadays, we have a theory that describes some of the Nature of the Universe and matter, known as the Standard Model (SM). This theory is currently the one that better describes matter in terms of elementary particles and interactions via the strong, weak, and electromagnetic forces; only the gravitational interaction is not included in the theory.

As listed in Table 2.1, elementary particles are divided into quarks and leptons, where both types of particles are split into three different generations, all being fermions. The first generation has the model's lightest and, therefore, most stable particles. In contrast, the second and third-generation particles are unstable and decay into lighter particles.

	Lepton/Quark	Mass [MeV]	Electric charge
First Generation	e^-	0.511	-1
	ν_e	$<1.1\times10^{-6}$	0
	u	2.16	2/3
	d	4.67	-1/3
Second Generation	μ^-	105.66	-1
	ν_μ	<0.19	0
	c	1.27×10^3	2/3
	s	93.4	-1/3
Third Generation	τ^-	1776.86	-1
	ν_τ	18.2	0
	t	172.69×10^3	2/3
	d	4.18×10^3	-1/3

Table 2.1: Elementary particles: quarks and leptons [5].

This gauge theory is based on three symmetry groups: $SU(3)_C \otimes SU(2)_L \otimes U(1)_Y$, where:

- $SU(3)_C$ [6–8]: leads to Quantum Chromodynamics (QCD), the theory that de-

scribes strong interactions and the letter 'C' stands for the color quantum number. This is a Non-Abelian gauge group with eight gauge bosons (eight massless gluons);

- $SU(2)_L \otimes U(1)_Y$ [9, 10] describes the electroweak gauge sector of the Standard Model, which unifies the electromagnetic interactions, mediated by photons, and weak interactions, mediated by three massive bosons; the letters 'L' and 'Y' stand for left-, involving only left-handed fermion fields, and weak hypercharge, respectively; This symmetry gets broken down to the $U(1)_{QED}$ subgroup by the Higgs mechanism, leading to the three massive bosons mediators $W^{\pm}$ and Z, and the massless photon γ, Table 2.2;

In order to generate the masses of the gauge bosons and of all the other elementary particles in the theory, the SM introduces the Spontatneous Symmetry Breaking (SSB) that gives rise to the appearance of a physical scalar particle called Higgs boson.

Bosons	Mass [GeV]	Charge [Q/e-]	Force
gluon	0	0	Strong
photon	$<10^{-27}$	0	Electromagnetic
W	80.377	± 1	Weak
Z	91.188	0	Weak
Higgs	125.25	0	

Table 2.2: Bosons [5].

2.1 Quantum Electrodynamics

Considering the free Dirac fermion Lagrangian:

$$\mathcal{L}_0 = i\bar{\phi}(x)\gamma^{\mu}\partial_{\mu}\phi(x) - m\bar{\phi}(x)\phi(x), \tag{2.1}$$

where γ^{μ}, $\phi(x)$ and m are the Dirac matrices, the spinor field, and the fermion mass, respectively. We see that it is invariant under a *global U(1)* transformation

$$\phi(x) \rightarrow \phi'(x) \equiv e^{iq\chi}\phi(x), \tag{2.2}$$

where $q\chi$ is an arbitrary real constant. Assuming the phase χ can be different at all points in space-time $q\chi \rightarrow q\chi(x)$, i.e, under *local* phase transformation, an extra term will arise from the derivative

$$\partial_{\mu}\phi(x) \rightarrow e^{iq\chi(x)}[\partial_{\mu} + iq\partial_{\mu}\chi(x)]\phi(x), \tag{2.3}$$

and the previous Lagrangian will no longer be invariant:

$$\mathcal{L}_0 \rightarrow \mathcal{L}' \equiv \mathcal{L}_0 - \bar{\phi}(x)\gamma^{\mu}q\partial_{\mu}\chi(x)\phi(x). \tag{2.4}$$

According to the 'gauge principle', the theory should remain invariant under local phase transformations and to guarantee this principle, an extra term needs to be added

to the Lagrangian such that its transformation cancels out the $\partial_\mu \chi(x)$ term in Eq.(2.3). For that, a new field $\mathcal{A}_\mu$ is introduced, transforming as

$$\mathcal{A}_\mu \to \mathcal{A}'_\mu = \mathcal{A}_\mu - \frac{1}{e}\partial_\mu \chi(x), \tag{2.5}$$

and replacing the derivative for the covariant derivative:

$$\partial_\mu \to D_\mu = \partial_\mu + iqe\mathcal{A}_\mu, \tag{2.6}$$

which has the following transformation:

$$D_\mu \phi(x) \to D'_\mu \phi'(x) \equiv e^{iq\chi(x)} D_\mu \phi_\mu(x). \tag{2.7}$$

Only with all of those transformations, the Lagrangian:

$$\mathcal{L} = i\bar{\phi}(x)\gamma^\mu D_\mu \phi(x) - m\bar{\phi}(x)\phi(x) = \mathcal{L}_0 - qe\bar{\phi}(x)\gamma^\mu \mathcal{A}_\mu \phi(x), \tag{2.8}$$

is then invariant under local $U(1)$ transformations.

The QED Lagrangian is:

$$\mathcal{L}_{QED} = i\bar{\phi}(x)(\gamma^\mu \partial_\mu - m)\phi(x) - qe\bar{\phi}(x)\gamma^\mu \mathcal{A}_\mu \phi(x) - \frac{1}{4}\mathcal{F}^{\mu\nu}\mathcal{F}_{\mu\nu}, \tag{2.9}$$

where the first term describes the free propagation of the ϕ fermion field, the second term describes the interaction between the Dirac fermion and the gauge field $\mathcal{A}_\mu$, which is the vertex of Quantum Electrodynamics (QED) Figure 2.1, while the third term describes the free propagation of the gauge field (photons). This last term is the kinematic term for the new spin-1 field $\mathcal{A}_\mu$, where $\mathcal{F}_{\mu\nu} = \partial^\mu \mathcal{A}^\nu - \partial^\nu \mathcal{A}^\mu$ is the electromagnetic field strength. The new gauge field must to be massless to preserve the local $U(1)$ gauge invariance.
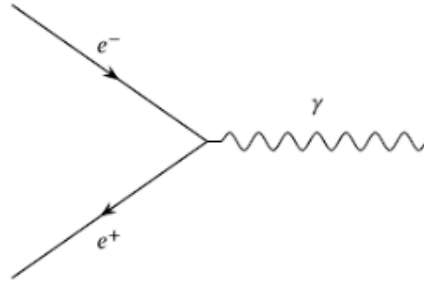
Figure 2.1: Example of a QED vertex: electron-positron annihilation.

2.2 Quantum Chromodynamics

To describe the strong interactions between quarks mediated by gluons, a non-Abelian quantum gauge field theory was created, the Quantum Chromodynamics or QCD, in which the gauge group is an $SU(3)_C$, acting on the degree of freedom 'color'.

Let's consider the following free Lagrangian for a quark field, q_f^α, of color α and flavor f:

$$\mathcal{L}_0 = \sum_f \bar{q}_f (i\gamma^\mu \partial_\mu - m_f) q_f, \tag{2.10}$$

using a vector notation in color space: $q_f^T \equiv (q_f^1, q_f^2, q_f^3)$. The Lagrangian in Eq.(2.10) is invariant under global $SU(3)_C$ transformations in color space,

$$q_f^\alpha \to (q_f^\alpha)' = U^\alpha_{\ \beta} q_f^\beta, \text{ being } U = e^{ig_s \frac{\lambda^a}{2} \theta_a}, \tag{2.11}$$

where λ^a (a = 1, 2, 3, ..., 8) denotes the generators of the fundamental representation of the $SU(3)_C$ algebra, θ_a are arbitrary phase parameters and the indices α and β run over the color quantum numbers. The matrices λ^a are traceless and satisfy the commutation relations:

$$[\lambda^a, \lambda^b] = 2if^{abc}\lambda^c, \tag{2.12}$$

with f^{abc} the $SU(3)_C$ structure constants which are real and totally antisymmetric matrices.

Like in Section 2.1, the Lagrangian need to be invariant under *local* $SU(3)_C$ transformations, $\theta_a = \theta_a(x)$. In order to make this possible, the quark derivatives need to be changed to covariant derivatives and extra terms added, more precisely, eight different gauge bosons $G_a^\mu(x)$, called gluons, leading to:

$$D^\mu q_f \equiv \left[\partial^\mu + ig_s \frac{\lambda^a}{2} G_a^\mu(x) \right] q_f \equiv [\partial^\mu + ig_s G^\mu(x)] q_f, \tag{2.13}$$

with the compact notation of:

$$[G^\mu(x)]_{\alpha\beta} \equiv \left(\frac{\lambda^a}{2} \right)_{\alpha\beta} G_a^\mu(x). \tag{2.14}$$

To be invariant, the covariant derivative and the gauge fields need to have the following transformations:

$$D^\mu \to (D^\mu)' = U D^\mu U^\dagger; \quad G^\mu \to (G^\mu)' = U G^\mu U^\dagger + \frac{i}{g_s}(\partial^\mu U) U^\dagger, \tag{2.15}$$

which, under the infinitesimal local $SU(3)_C$ transformations, the fields transform as:

$$q_f^\alpha \to (q_f^\alpha)' = q_f^\alpha + ig_s \left(\frac{\lambda^a}{2} \right)_{\alpha\beta} \delta\theta_a q_f^\beta, \tag{2.16}$$

$$G_a^\mu \to (G_a^\mu)' = G_a^\mu - \partial^\mu(\delta\theta_a) - g_s f^{abc} \delta\theta_b G_c^\mu. \tag{2.17}$$

The non-Abelian property of the $SU(3)_C$ matrices bring up an extra term involving interactions between the gluon fields.

To have a kinematic term for the gluon fields that keeps the local invariant for the Lagrangian, the field strengths can be defined as:

$$G^{\mu\nu}(x) \equiv -\frac{i}{g_s}[D^\mu, D^\nu] = \partial^\mu G^\nu - \partial^\nu G^\mu + ig_s[G^\mu, G^\nu] \equiv \frac{\lambda^a}{2} G_a^{\mu\nu}(x), \tag{2.18}$$

with

$$G_a^{\mu\nu}(x) = \partial^\mu G_a^\nu - \partial^\nu G_a^\mu - g_s f^{abc} G_b^\mu G_c^\nu, \tag{2.19}$$

such that

$$G^{\mu\nu} \rightarrow (G^{\mu\nu})' = UG^{\mu\nu}U^{\dagger}, \tag{2.20}$$

and the color trace, $\text{Tr}(G^{\mu\nu}G_{\mu\nu}) = \frac{1}{2}G_a^{\mu\nu}G_{\mu\nu}^a$, remains invariant.

From all of the transformations on the fields and with the proper normalization for the gluon kinetic term, is possible to write the gauge-invariant version of the Lagrangian of Quantum Chromodynamics,

$$\mathcal{L}_{QCD} \equiv -\frac{1}{4}G_a^{\mu\nu}G_{\mu\nu}^a + \sum_f \bar{q}_f(i\gamma^\mu D_\mu - m_f)q_f. \tag{2.21}$$

Like in QED, the $SU(3)_C$ symmetry forbids the existence of the mass term for the gluon fields since this term will make the invariance of the Lagrangian impossible, so these gluon fields are massless spin-1 particles.

The decompose Lagrangian is:

$$\begin{aligned}
\mathcal{L}_{QCD} = &-\frac{1}{4}(\partial^\mu G_a^\nu - \partial^\nu G_a^\mu)(\partial_\mu G_\nu^a - \partial_\nu G_\mu^a) + \sum_f \bar{q}_f(i\gamma^\mu\partial_\mu - m_f)q_f \\
&- g_s G_a^\mu \sum_f \bar{q}_f^\alpha \gamma_\mu \left(\frac{\lambda^a}{2}\right)_{\alpha\beta} q_f^\beta \\
&- \frac{g_s^2}{4}f^{abc}f_{ade}G_b^\mu G_c^\nu G_\mu^d G_\nu^e + \frac{g_s}{2}f^{abc}(\partial^\mu G_a^\nu - \partial^\nu G_a^\mu)G_\mu^b G_\nu^c.
\end{aligned} \tag{2.22}$$

In this final form of the QCD Lagrangian, is possible to describe the following interactions:

- The **first line** contains the kinetic terms for the different fields, which give rise to the corresponding propagators;

- The **second line** describe the interaction between quarks and gluons, involving the $SU(3)_C$ matrices λ^a;

- The **third line** terms generates the cubic and quartic gluon self-interaction and the strength of these interactions is given by the strong coupling constant g_s;

2.3 Weak and Electroweak Theory

In Sections 2.1 and 2.2 were shown the $U(1)$ and $SU(3)_C$ local gauge symmetries. To describe weak interactions, a more complex structure is needed, with several fermionic flavors and different properties for left- and right-handed fields, where the left-handed fermions should appear in doublets. This type of interaction is associated with invariance under $SU(2)$ local phase transformations,

$$\psi(x) \rightarrow \psi'(x) = U\psi(x) \text{ being } U \equiv exp[i\boldsymbol{\alpha}(x) \cdot \mathbf{T}], \tag{2.23}$$

where, $\boldsymbol{\alpha}(x)$ are the three functions which specify the local phase at each point in space-time and $\mathbf{T}$ are the three generators of the $SU(2)$ group that can be written in terms of the Pauli spin matrices,

$$\mathbf{T} = \frac{1}{2}\sigma.$$

To achieve the local gauge invariance, three gauge fields, W_μ^k with $k = 1, 2, 3$, corresponding to three gauge bosons W^1, W^2 and W^3, need to be introduced and since the $SU(2)$ generators are the 2x2 Pauli matrices, the field in Eq.(2.23) must be written in terms of two components known as a *weak isospin doublet*, like left-handed (LH) particles or right-handed (RH) antiparticles. To accomplish this, RH particles and LH antiparticles states are placed in weak isospin singlets and are therefore unaffected by the $SU(2)$ local gauge transformation.

So, in order to include electromagnetic interaction with weak interactions, the $U(1)$ group needs to be added forming the symmetry group:

$$G \equiv SU(2)_L \otimes U(1)_Y, \tag{2.24}$$

where L stands for left-handed fields and Y for weak hypercharge.

Let's consider the free Lagrangian for massless fermions:

$$\mathcal{L}_0 = \sum_{j=1}^{3} i\bar{\psi}_j(x)\gamma^\mu \partial_\mu \psi(x)_j \tag{2.25}$$

with: ψ_1 as a doublet field while $\psi_{2/3}$ are singlet fields. The Lagrangian $\mathcal{L}_0$ is invariant under global G transformations in flavor space:

$$\begin{aligned}
\psi_1(x) &\rightarrow \psi_1'(x) \equiv exp\{iy_1\beta\}U_L\psi_1(x) \\
\psi_k(x) &\rightarrow \psi_k'(x) \equiv exp\{iy_k\beta\}\psi_k(x) \text{ with } k = 2, 3,
\end{aligned} \tag{2.26}$$

with y_i (i = 1, 2, 3) as hypercharges and the $SU(2)_L$ transformation:

$$U_L \equiv exp\{i\frac{\sigma_i}{2}\alpha^i\} \quad i = 1, 2, 3 \tag{2.27}$$

is a non-Abelian transformation like in QCD.

As was done in the previous Sections, the Lagrangian is required to be invariant under local $SU(2)_L \otimes U(1)_Y$ transformations, and for that, four different gauge bosons fields are needed: a weak isospin triplet W^1, W^2, W^3 ($SU(2)_L$) and a weak hypercharge singlet B ($U(1)_Y$) in addition to the replacement of the derivative to the covariant derivative[1]:

$$D_\mu^j \psi_j(x) \equiv \left[\partial_\mu + ig'y_j B_\mu(x) + i\delta_{1j}g_w \widetilde{W}_\mu(x)\right]\psi_j(x) \quad (j = 1, 2, 3), \tag{2.28}$$

where

$$\widetilde{W}_\mu(x) = \frac{\sigma_i}{2}W_\mu^i(x). \tag{2.29}$$

For D_μ^j to transform in the same way as the fields, the gauge fields need to have the following transformations:

$$B_\mu \rightarrow B_\mu' = B_\mu - \frac{1}{g'}\partial_\mu\beta(x), \tag{2.30}$$

$$\widetilde{W}_\mu \rightarrow \widetilde{W}_\mu' = U_L\widetilde{W}_\mu U_L^\dagger + \frac{i}{g_w}(\partial^\mu U_L)U_L^\dagger, \tag{2.31}$$

---

[1]The δ_{1j} in Eq.(2.28) is a notation that I use just for this equation to refer to the fact that the $\tilde{W}_\mu$ only interact with $SU(2)_L$ doublet field $\psi_1(x)$.

where U_L is the transformation in Eq.(2.27) but with $\alpha^i = \alpha^i(x)$. Despite the differences between coupling constants, it is possible to observe that the transformation of B is identical to the QED gauge boson in Eq.(2.5), while the W field transforms in a way analogous to the gluons field in QCD Eq.(2.15). The difference between the last two fields is the number of generators in each representation and the structure constant, wherein $SU(2)_L$ is known as the Levi-Civita tensor, ϵ^{ikj}. The same happens for the field strengths structures and transformations.

The Electroweak Lagrangian is:

$$\mathcal{L}_{EW} = \sum_{j=1}^{3} i\bar{\psi}_j(x)\gamma^\mu D_\mu \psi(x)_j - \frac{1}{4} W_{\mu\nu}^i W_i^{\mu\nu} - \frac{1}{4} B^{\mu\nu} B_{\mu\nu}, \tag{2.32}$$

where the first term corresponds to the fermion propagator and the fermion interaction with the gauge bosons, while the last two terms describe the EW free field propagation with the kinematics terms for both W_μ and B_μ fields. Like in QCD, the field strength $W_{\mu\nu}^i$ contains a quartic piece that gives rise to cubic and quartic self-interaction among the gauge fields with the strength of the $SU(2)_L$ coupling constant g_W. The gauge symmetry not only forbids again the mass terms for the gauge bosons but also forbids the fermionic masses because they would provide a relationship between left- and right-handed fields, which have different transformation properties and therefore would break explicit the gauge symmetry.

2.4 Spontaneous Symmetry Breaking: Higgs Mechanism

To generate masses, the gauge symmetry needs to be spontaneous broken keeping a fully symmetric Lagrangian to preserve renormalization, so let's consider a Lagrangian that:

1 Is invariant under a group G of transformations.

2 Has a degenerate set of states with minimal energy.

Selecting one of those states as the ground state of the system, the symmetry is said to be spontaneously broken.

So let's consider a Lagrangian for a complex scalar field $\phi(x)$:

$$\mathcal{L} \equiv T - V = \partial_\mu \phi^\dagger \partial^\mu \phi - (\mu^2 \phi^\dagger \phi + \lambda(\phi^\dagger \phi)^2), \tag{2.33}$$

where $\lambda > 0$, in order to have a ground state, and the Lagrangian is invariant under global phase transformations of the scalar field:

$$\phi(x) \rightarrow \phi'(x) \equiv e^{ig\chi}\phi(x). \tag{2.34}$$

The potential will show two possible shapes, depending on the sign of the quartic term, μ^2 [11]:

1. $\boldsymbol{\mu^2 > 0}$, the potential has only the trivial minimum $\phi = 0$, the ground state, describing a massive scalar field with mass μ and quartic coupling λ, Figure 2.2a;
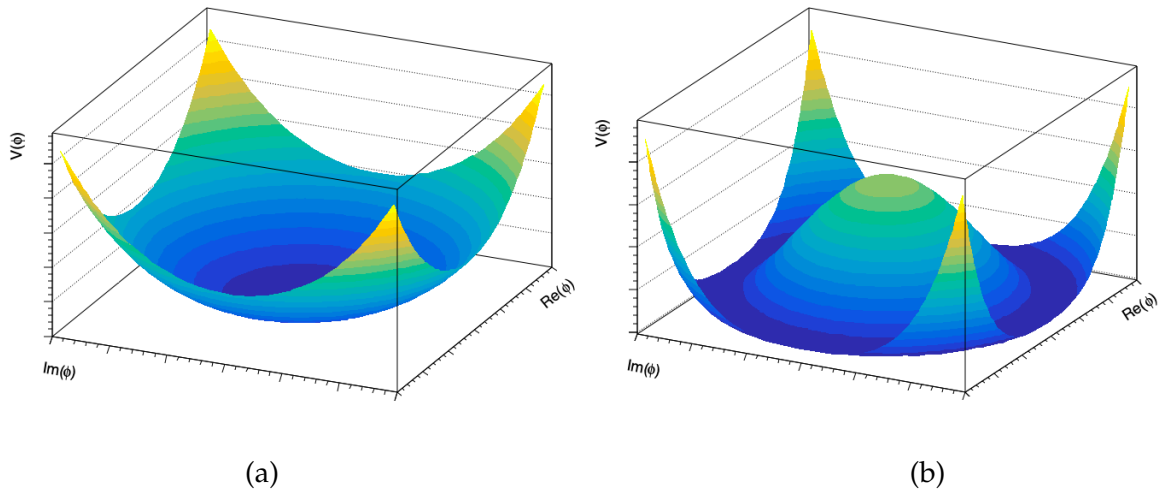
Figure 2.2: Higgs potential for $\mu^2 > 0$ (a) and $\mu^2 < 0$ (b).

2. $\boldsymbol{\mu^2 < 0}$, the associated term in the Lagrangian can no longer be interpreted as a mass, given an infinite number of degenerate states of minimum energy satisfying:

$$| \phi_0 |= \pm\sqrt{\frac{-\mu^2}{2\lambda}} = \pm\frac{v}{\sqrt{2}}, \qquad (2.35)$$

where v is the vacuum mean value of the field, also called the vacuum expectation value (vev). The choice of the vacuum state breaks the symmetry of the Lagrangian, having a *spontaneous symmetry breaking*, Figure 2.2b.

If the perturbation of the ground state is parametrized in terms of two real field, φ_1 and φ_2, as:

$$\phi(x) \equiv \frac{1}{\sqrt{2}}[v + \varphi_1(x) + i\varphi_2(x)], \qquad (2.36)$$

the potential becomes:

$$V(\phi) = V(\phi_0) - \mu^2\varphi_1^2 + \lambda v\varphi_1(\varphi_1^2 + \varphi_2^2) + \frac{\lambda}{4}(\varphi_1^2 + \varphi_2^2)^2, \qquad (2.37)$$

where the φ_1 describes a massive state with mass $m_{\varphi_1} = -2\mu^2$, while φ_2 is a massless state. The particles described by this massless state correspond to excitations in the direction where the potential does not change, i.e., into states with the same energy as the chosen ground state. This massless scalar particle is known as a Goldstone boson [12].

2.5 Higgs Mechanism

Let's consider the following Lagrangian, which is invariant under local $SU(2)_L \otimes U(1)_Y$ transformations:

$$\mathcal{L} = (D_\mu\phi)^\dagger D^\mu\phi - \mu^2\phi^\dagger\phi - \lambda\left(\phi^\dagger\phi\right)^2 \quad ,\lambda > 0 , \qquad (2.38)$$

with

$$D^\mu \phi \equiv \left[\partial^\mu + ig' y_\phi B^\mu(x) + ig_w \widetilde{W}^\mu(x)\right]\phi, \quad y_\phi = Q_\phi - T_3 \qquad (2.39)$$

where the g' and g_w are the $U(1)_Y$ and $SU(2)_L$ coupling constants and the hypercharge, y_ϕ, depends on the electric charge, Q_ϕ, of the $SU(2)_L$ doublet of the complex scalar field:

$$\phi = \begin{pmatrix} \phi^+ \\ \phi^0 \end{pmatrix} = \frac{1}{\sqrt{2}}\begin{pmatrix} \phi_1 + i\phi_2 \\ \phi_3 + i\phi_4 \end{pmatrix}. \qquad (2.40)$$

This scalar Lagrangian is very similar to the Lagrangian in Eq.(2.33). So, when $\mu^2 < 0$, there is not a single minimum but an infinite set of degenerate states with minimum energy, or *vacuum*, at:

$$\phi^\dagger \phi = \phi_1^2 + \phi_2^2 + \phi_3^2 + \phi_4^2 = -\frac{\mu^2}{2\lambda} = \frac{v^2}{2}. \qquad (2.41)$$

The choice of the particular ground state implies the spontaneous breaking of the $SU(2)_L \otimes U(1)_Y$ symmetry to the electromagnetic subgroup $U(1)_{QED}$, which remain at symmetric the vacuum. Since the electric charge is a conserved quantity, the scalar field that will acquire a vacuum expectation value must be neutral[2]:

$$\left|\langle 0 \mid \phi^0 \mid 0 \rangle\right| = \sqrt{\frac{-\mu^2}{2\lambda}} = \frac{v}{\sqrt{2}}. \qquad (2.42)$$

The fields can be expanded in around the minimum, v:

$$\phi(x) = \frac{1}{\sqrt{2}}\begin{pmatrix} \phi_1(x) + i\phi_2(x) \\ v + \rho(x) + i\phi_4(x) \end{pmatrix}. \qquad (2.43)$$

After the spontaneous breaking of the symmetry, and according to the Goldstone theorem [12, 13], there will be one new massive boson, $\rho(x)$, and three massless bosons. It is possible to eliminate these massless bosons by gauge transformation to have the scalar doublet in the general form:

$$\phi(x) = \frac{1}{\sqrt{2}}\begin{pmatrix} 0 \\ v + \rho(x) \end{pmatrix} = \frac{1}{\sqrt{2}}\begin{pmatrix} 0 \\ v + h(x) \end{pmatrix} \quad \textit{(unitary gauge)}, \qquad (2.44)$$

where the field $\rho(x)$ has been written as the Higgs field *h(x)*.

Now is possible to generate the W and Z gauges masses using the Higgs mechanism and the term that generates the masses is $(D_\mu \phi)^\dagger D^\mu \phi$. Expanding the covariant derivative product:

$$\begin{aligned}(D_\mu \phi)^\dagger D^\mu \phi =& \frac{1}{2}(\partial_\mu h)(\partial^\mu h) + \frac{1}{8}g_W^2(W_\mu^{(1)} + iW_\mu^{(2)})(W^{(1)\mu} - iW^{(2)\mu})(v+h)^2 \\ & + \frac{1}{8}(g_W W_\mu^{(3)} - g'B_\mu)(g_W W^{(3)\mu} - g'B^\mu)(v+h)^2\end{aligned} \qquad (2.45)$$

where the charged vector bosons, $W^\pm$ are defined as:

$$W_\mu^\pm = \frac{1}{\sqrt{2}}(W_\mu^{(1)} \mp iW_\mu^{(2)}) \text{ with } m_W = \frac{1}{2}vg_W \qquad (2.46)$$

---

[2]The hypercharge is $y_{\phi^0} = \frac{1}{2}$.

and the two remaining neutral gauge bosons, Z and A, are defined as:

$$Z_\mu = \frac{1}{\sqrt{g_W^2 + g'^2}} (g_W W_\mu^{(3)} - g' B_\mu) \text{ with } m_Z = \frac{1}{2} v \sqrt{g_W^2 + g'^2}$$

$$A_\mu = \frac{1}{\sqrt{g_W^2 + g'^2}} (g_W W_\mu^{(3)} + g' B_\mu) \text{ with } m_A = 0 \tag{2.47}$$

where the measured masses are in Table 2.2. Instead of using two different couplings constants, one from $U(1)_Y$ and the other from $SU(2)_L$, is possible to relate them using the ratio,

$$\frac{g'}{g_W} = \tan \theta_W \tag{2.48}$$

and using this relation, is possible to relate the W and Z bosons masses:

$$\frac{m_W}{m_Z} = \cos \theta_W \tag{2.49}$$

where with some trigonometric relations, the electroweak mixing angle is:

$$\sin^2 \theta_W = 1 - \frac{m_W^2}{m_Z^2} = 0.23121, \tag{2.50}$$

and

$$v = 246 \; GeV. \tag{2.51}$$

From the scalar Lagrangian in Eq.(2.38) a new scalar field is introduced: the Higgs boson. So, expanding this scalar Lagrangian in terms of the physical gauge fields it is possible to get the Higgs boson mass and the bosons interactions,

$$\begin{aligned} \mathcal{L} = &\frac{1}{2} (\partial_\mu h)(\partial^\mu h) - \frac{1}{2} m_h^2 - \frac{m_h^2}{2v} h^3 - \frac{m_h^2}{8v^2} h^4 \\ &+ m_W^2 W_\mu^+ W^{\mu-} \left\{ 1 + \frac{2}{v} h + \frac{h^2}{v^2} \right\} \\ &+ \frac{1}{2} m_Z^2 Z_\mu Z^\mu \left\{ 1 + \frac{2}{v} h + \frac{h^2}{v^2} \right\} \end{aligned} \tag{2.52}$$

where:

- the Higgs boson mass is $m_h = \sqrt{2\lambda} v$ being:

$$\text{CMS [14]} : 125.38 \pm 0.14 \; GeV \tag{2.53}$$

$$\text{ATLAS [15]} : 124.94 \pm 0.17(\text{stat}) \pm 0.03(\text{syst}) \; GeV \tag{2.54}$$

- the Higgs self-couplings $\lambda_{hhh} = \frac{m_h^2}{2v}$ and $\lambda_{hhhh} = \frac{m_h^2}{8v^2}$

- the second and the third line give the interactions between Higgs bosons and W/Z gauge bosons respectively, Figure 2.3;
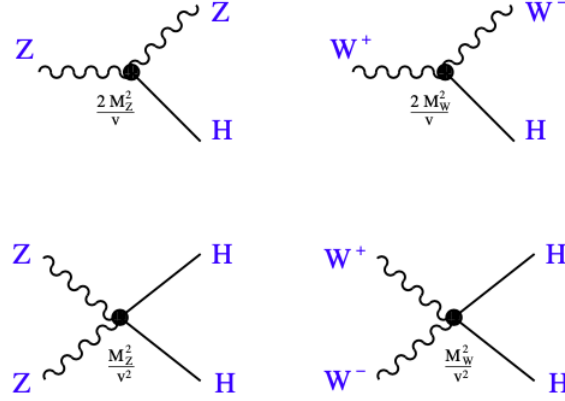
Figure 2.3: Couplings between Higgs boson and gauge bosons.

2.5.1 Fermion Masses

This mechanism is responsible for generating the W and Z boson masses but also the mass of the fermions. However, due to the different transformation properties of left- and right-handed chiral states, the fermion mass in the Dirac Lagrangian,

$$\mathcal{L} = -m\bar{\psi}\psi = -m(\bar{\psi}_L\psi_R + \bar{\psi}_R\psi_L), \tag{2.55}$$

where ψ_L is the left-handed fermion doublet, ψ_R is the right-handed fermion singlet, but the fermionic mass term does not respect the $SU(2)_L \otimes U(1)_Y$ gauge symmetry and therefore, cannot be present in the Lagrangian of the SM. However, we already have introduced an additional scalar doublet into our model, Eq.(2.40), so we can use the following gauge-invariant fermion-scalar coupling:

$$
\begin{aligned}
\mathcal{L}_{fermions} = &- c_1(\bar{u},\bar{d})_L \begin{pmatrix} \phi^{(+)} \\ \phi^{(0)} \end{pmatrix} d_R - c_2(\bar{u},\bar{d})_L \begin{pmatrix} \phi^{(0)*} \\ -\phi^{(-)} \end{pmatrix} u_R \\
&- c_3 (\bar{v}_e,\bar{e})_L \begin{pmatrix} \phi^{(+)} \\ \phi^{(0)} \end{pmatrix} e_R + hermitian\ conjugate,
\end{aligned}
\tag{2.56}
$$

where the second term is the complex-conjugate scalar field[3], and c_i are arbitrary parameters that can be written in terms of the fermion's mass and v. After the spontaneous symmetry breaking, this Lagrangian takes the form:

$$\mathcal{L} = \frac{1}{\sqrt{2}}(v + h)\left(c_1\bar{d}d + c_2\bar{u}u + c_3\bar{e}e\right). \tag{2.57}$$

This mechanism also can generate the fermion masses:

$$m_j = c_i\frac{v}{\sqrt{2}} \quad \text{with } (j,i) = (d,1),\ (u,2),\ (e,3). \tag{2.58}$$

so, the Lagrangian takes the form:

$$\mathcal{L} = -\left(1 + \frac{h}{v}\right)\left[m_d\bar{d}d + m_u\bar{u}u + m_e\bar{e}e\right]. \tag{2.59}$$

---

[3] $\phi^c \equiv i\sigma_2\phi^*$
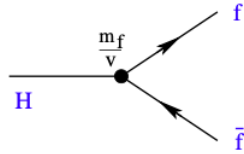
Figure 2.4: Couplings between Higgs boson and fermions.

The first term in Eq.(2.59) defines the fermion's mass, while the second term contains the interaction between the fermion and the Higgs field. This procedure can be extended to fundamental particles' second and third generations, where the c_i parameter from Eq.(2.58), known as the Yukawa couplings, Figure 2.4, for all fermions are given by:

$$c_{fermion} = \sqrt{2}\frac{m_{fermion}}{v}. \tag{2.60}$$

2.6 Higgs boson

The Higgs mechanism was proposed almost simultaneously by three independent groups in 1964: F. Englert and R. Brout [16], P. W. Higgs [17], and C. Guralnik, C. R. Hagen and T. Kibble [18]. However, the theory did not predict the mass of the Higgs boson. Many years after its formulation had to pass until a significant mass range could be probed first with Large Electron Positron Collider (LEP) at CERN [19] and then with the Tevatron proton-antiproton collider [20]. Only in July 2012 was the Higgs boson observed by the ATLAS and the CMS experiments at the LHC [2, 3].

Since its discovery, studying the Higgs boson has been one of the main focuses to understand the nature of electroweak symmetry breaking while searching for the SM effects from New Physics (NP). ATLAS and CMS experiments have as one of their primary focuses the precision measurement of properties of the Higgs boson, including the mass, couplings, and evidence for production mechanisms.

2.6.1 Higgs Boson Production at LHC

At hadron colliders, the main Higgs boson production channels are the following: by fusion of gluon (gluon-fusion or *ggF*), by vector-boson fusion (*VBF*), by Higgsstrahlung with a W or Z boson associated (*VH* with V being W or Z), and associated production with a single or a pair of top-quarks (*tH+ttH*). Figure 2.5 presents the cross-section of the different Higgs boson production channels at the LHC as a function of the center of mass energy (a) and the Higgs boson mass (b). The cross-section values of the Higgs production for each channel previously presented are in Table 2.3.

2.6.2 Higgs Boson: Decays

The *branching ratio* (*BR*) is the fraction of time a particle decays to a particular final state. This frequency is related to the partial and total decay rate, or width, (Γ) through:

$$BR(\mathrm{H} \to X_f) = \frac{\Gamma(\mathrm{H} \to X_f)}{\sum_f \Gamma(\mathrm{H} \to X_f)}. \tag{2.61}$$

(a)

(b)
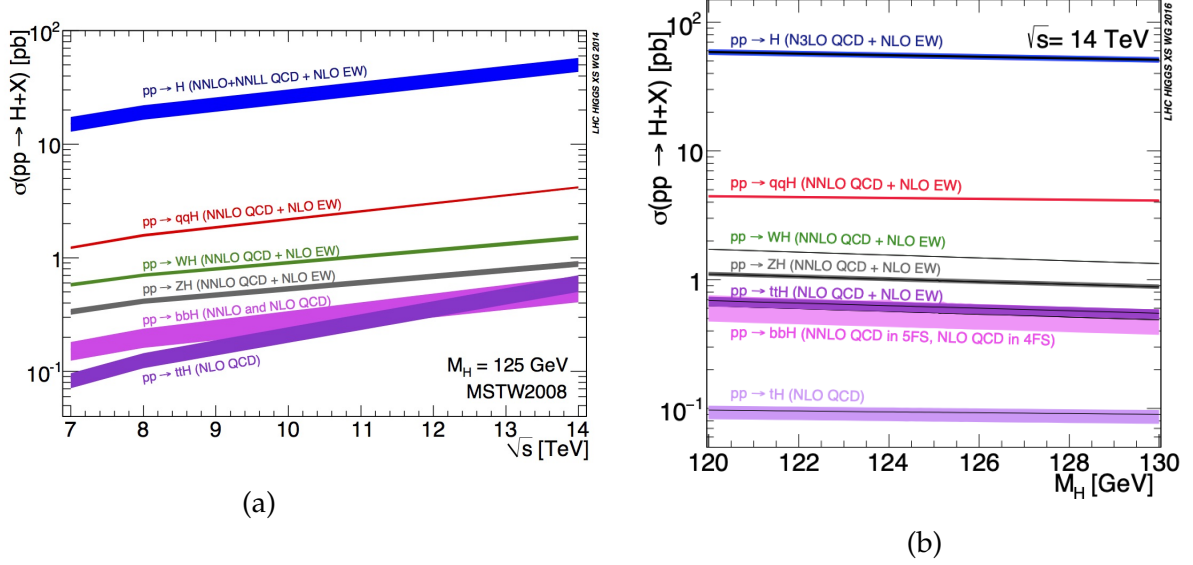
Figure 2.5: The SM Higgs boson production cross-section as a function of the LHC $\sqrt{s}$ (a) and as a function of the Higgs boson mass at $\sqrt{s}$=14 TeV (b). [21]

Channel	σ [pb]	Scale [%]
ggF	49.97	+7.5 -8.0
VBF	4.048	+0.8 -0.4
WH	1.504	+0.3 -0.6
ZH	0.883	+2.7 -1.8
ttH	0.6113	+5.9 -9.3

Table 2.3: SM Higgs production cross-section at $\sqrt{s}$=14 TeV with m_H=125 GeV. [22]

Following an SM prediction, the branching ratio of the different decays of the Higgs boson is shown in Figure 2.6, and in Table 2.4 are its values for a m_H=125 GeV. Since the Higgs boson gives mass to the particles, a heavier particle implies a stronger interaction and is more likely to decay into that heavy particle, such as the Z or W bosons. However, according to the SM predictions, at $m_H \sim$125 GeV, the most dominant decay channel is to a $b\bar{b}$ pair, accounting for $\sim$53% of the total decay. In the second most common decay channel, the W boson can decay into a pair of quark and antiquark or a charged lepton and a neutrino. Since the background is full of hadrons in a hadron collider, the first-mentioned W decay makes it very difficult to distinguish the signal from the background, and due to the presence of neutrinos in the second decay, $W^- \rightarrow e^- \bar{\nu}_e$ ($W^+ \rightarrow e^+ \nu_e$), this channel cannot be fully reconstructed. The decay H→ZZ, known as the "*golden channel*", is the best decay mode to detect the Higgs boson since the pair of Z bosons can turn into four leptons in total. Although this decay mode is rare, it is easy to spot in the middle of the background, as seen in Figure 2.7.
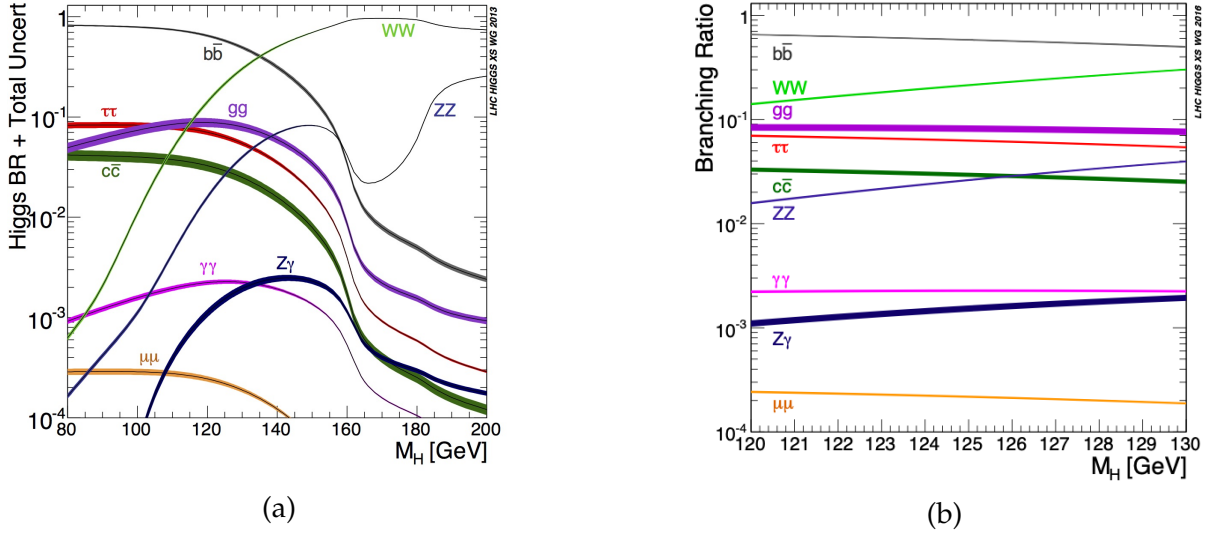
Figure 2.6: The SM Higgs boson branching ratios as a function of m_H for a range of [80,200] GeV and for a range of [120,130] GeV[21].

Channel	Branching ratio (%)
H → $b\bar{b}$	53
H → WW	25.7
H → ZZ	2.8
H → $\gamma\gamma$	0.25
H → $\mu\mu$	0.026
H → $\tau\tau$	6.0
H → gg [23]	8.57
Γ_H	$3.2^{+2.4}_{-1.7}$ MeV

Table 2.4: Higgs boson branching ratios for different channels and the Higgs total width, Γ_H, Ref.[5].

2.6.3 Di-Higgs Production

The production of pairs of Higgs bosons at hadron colliders provides unique information on the Higgs sector and the electroweak symmetry-breaking mechanism. Although the quartic Higgs coupling cannot be directly measured at the LHC, λ_{hhh} can be accessed directly by this pair boson production. At hadron colliders, a pair of Higgs bosons is dominantly produced in the loop-induced gluon-fusion mechanism, shown in Figure 2.9a, mainly mediated by top-quark loops, supplemented by a smaller contribution of b-quark loops, while *VBF*, *VHH*, and *ttHH* processes have a sub-leading role.

The QCD corrections in the production of Higgs boson pairs via *ggF* increase the total cross-section by a factor of two from LO to NLO and by 20% from NLO to NNLO to reach at 14 TeV [24]:

$$\sigma(gg \to HH)^{\text{NNLO,FTa}}_{ggF} = 36.69 \text{ fb}^{+2.1\%}_{-4.9\%}(\text{theory}) \pm 3\%(\alpha_s + \text{PDF}). \qquad (2.62)$$

However, with this cross-section and low signal-background discrimination, producing a pair of Higgs bosons remains a challenging channel to measure.

In 2019, the ATLAS experiment set new limits on the gluon fusion channel of the Higgs boson pair production process, exploiting up to 36.1 fb^{-1} of proton-proton collision data at $\sqrt{s}$=13 TeV. The combination of six analyses searching for Higgs boson pairs decaying into $b\bar{b}b\bar{b}$, $b\bar{b}W^+W^-$, $b\bar{b}\tau^+\tau^-$, $W^+W^-W^+W^-$, $b\bar{b}\gamma\gamma$ and $W^+W^-\gamma\gamma$ in the final states reached a combined observed (expected) limit at 95% confidence level on the non-resonant Higgs boson pair production cross-section of 6.9 (10) times the predicted SM cross-section [26]. The upper limits of the ggF HH cross-section for the individual decay modes and their combination are presented in Figure 2.10.
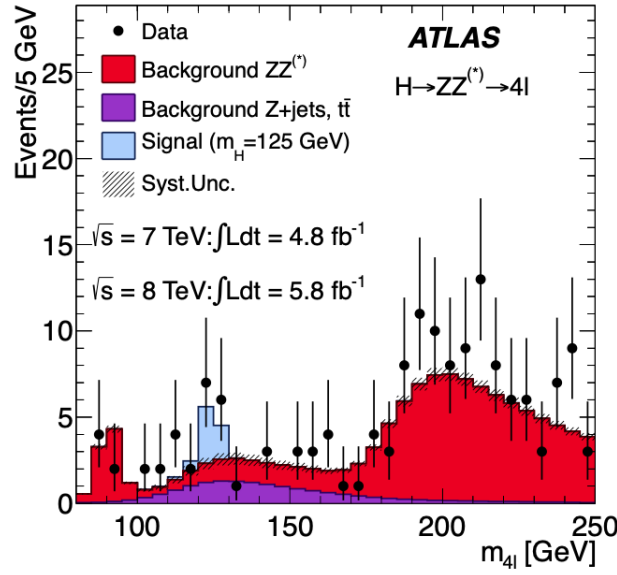
Figure 2.7: Distribution of the four-lepton invariant mass, m$_{4l}$, compared to the background, for the combination of the $\sqrt{s}$= 7 and 8 TeV data. (take from Ref [3])
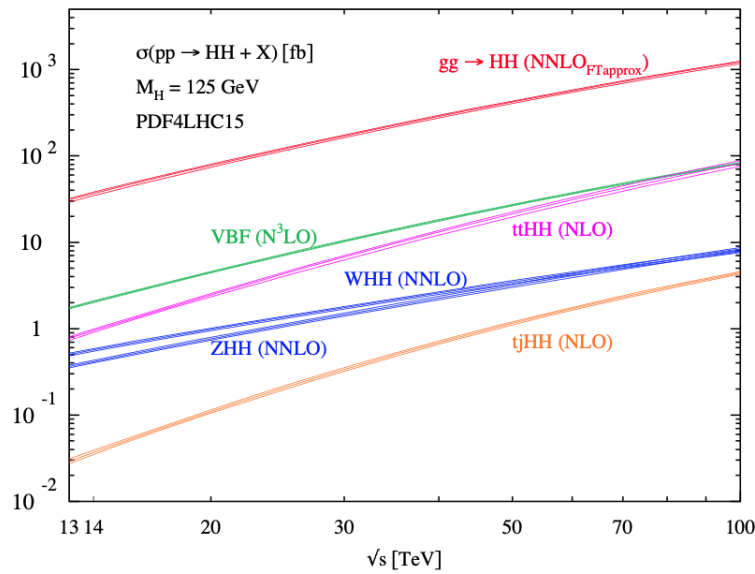
Figure 2.8: Total production cross-section for Higgs pairs within the SM.
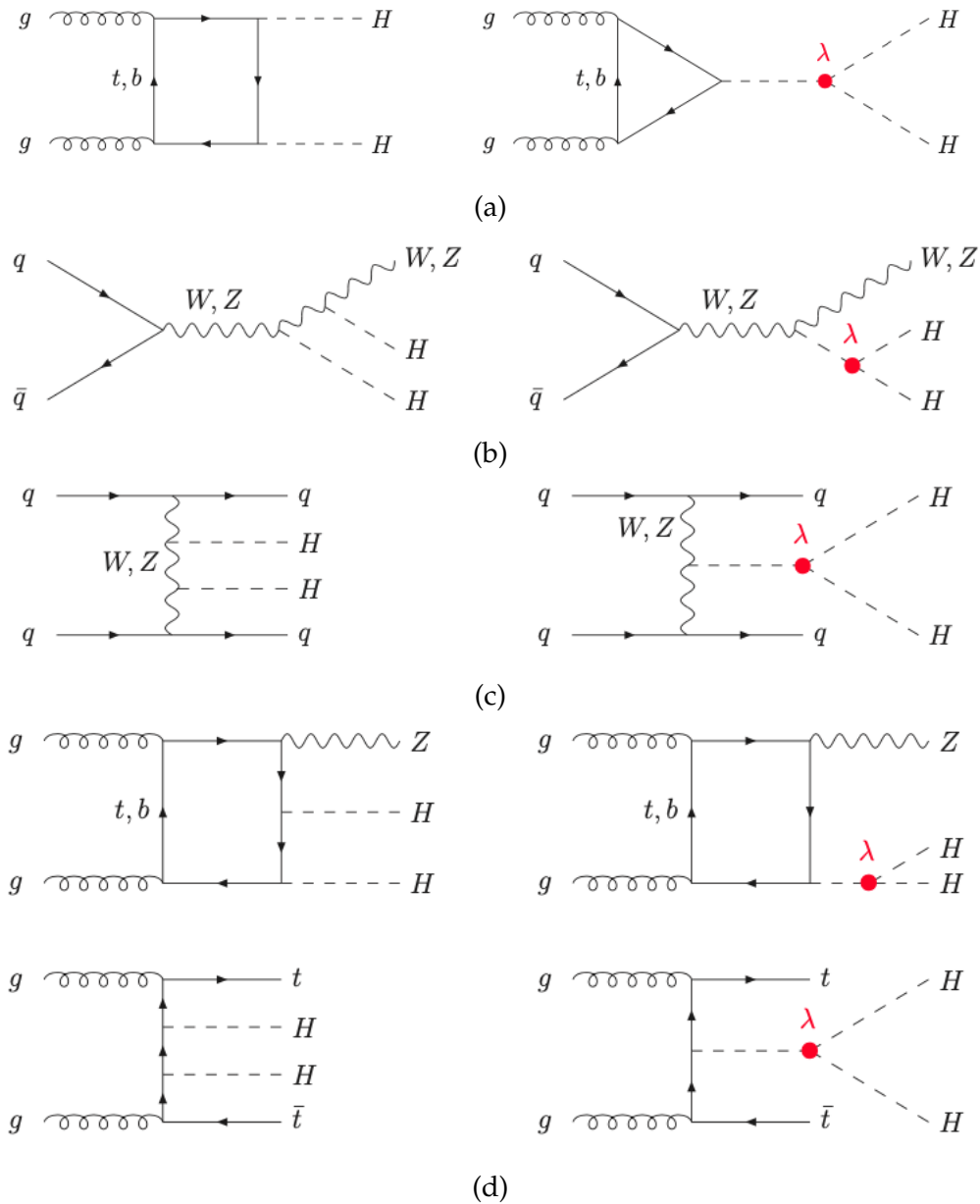
Figure 2.9: Higgs pair production diagrams for (a) gluon-fusion, (b) double Higgsstrahlung, (c) vector boson fusion processes, and (d) double Higgs bremsstrahlung off top quarks. The contribution from λ_{hhh} is marked in red [25].

2.6.4   Higgs self-coupling

From Eq.(2.38) and (2.52), it is possible to understand that the shape of the Higgs potential, responsible for the EWSB, is determined by the Higgs self-coupling constants λ_{hhh} and λ_{hhhh}. A precise measurement of these coupling constants is fundamental to understanding the structure of the potential, in which the exact shape can have profound theoretical consequences. For example, the shape of the Higgs potential, particularly the value of λ_{hhh}, controls the dynamics of the EW phase transition. This phase transition defines the viability of models of electroweak *baryogenesis* [27]. Another example is the stability of the vacuum. The possibility of the vacuum that we currently know is not stable but rather *metastable*, which implies the presence of a new minimum at very
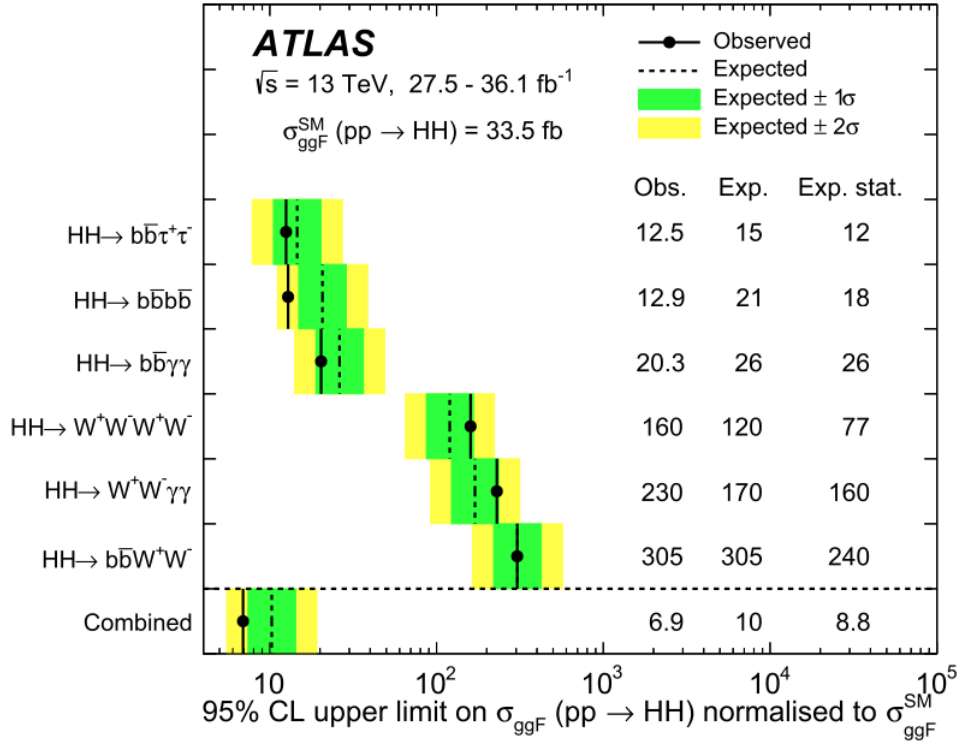
Figure 2.10: Upper limits at 95% CL on the σ_{ggF}(pp→HH) normalized to its SM expectation value from multiple HH decay searches and their statistical combination [26].

large values of the Higgs field, could be a potential source of a stochastic background of gravitational waves [28, 29]. To be able to shed some light on these questions, constraints to the trilinear self-coupling have been a long-term goal of the LHC.

The λ_{hhh} can be probed from direct searches for HH final states and indirectly via its effects on precision observables or from loop corrections to single Higgs production. However, due to the suppressing power of v, the quartic term is not currently accessible at LHC.

Recently, the ATLAS and CMS collaborations found new boundaries to λ_{hhh} performing at $\sqrt{s}$=13 TeV up to 36.1 fb^{-1} and 35.9 fb^{-1}, respectively, of the combine data from different Higgs decays. The results in Figure 2.11 are reported regarding the ratio between the Higgs boson self-coupling and its SM expectation value for each experiment, $\kappa_\lambda = \lambda_{hhh}/\lambda_{hhh}^{SM}$, reaching bounds of:

$$\text{ATLAS [26]} \quad -5.0 < \kappa_\lambda < 12.0\,\text{(observed)}, \quad -5.8 < \kappa_\lambda < 12.0\,\text{(expected)} \quad (2.63)$$

$$\text{CMS [30]} \quad -11.8 < \kappa_\lambda < 18.8\,\text{(observed)}, \quad -7.1 < \kappa_\lambda < 13.6\,\text{(expected)} \quad (2.64)$$

The results from Figure 2.11 show that the significance of the observation of the HH process reaches 4σ. The secondary minimum is expected to be excluded at 99.4% CL. The predicted precision on κ_λ is approximately 50% at HL-LHC.
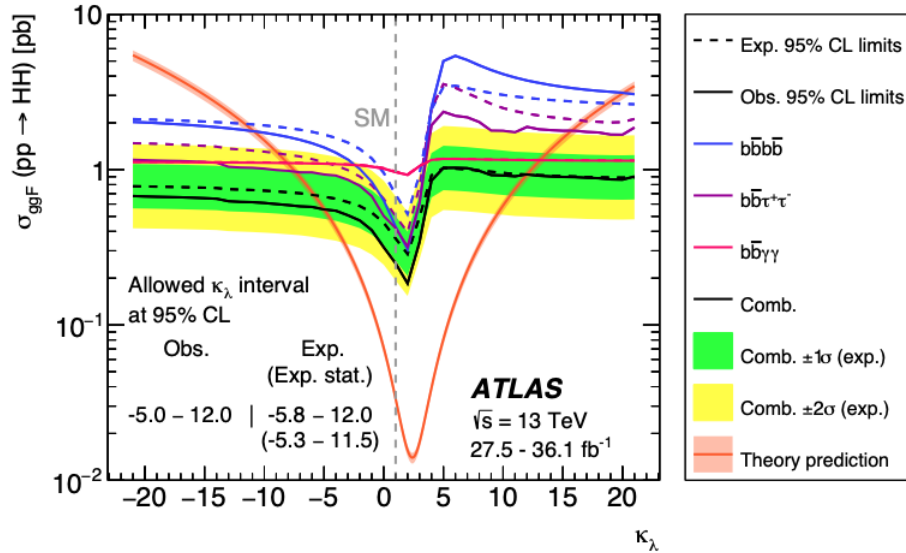
(a)
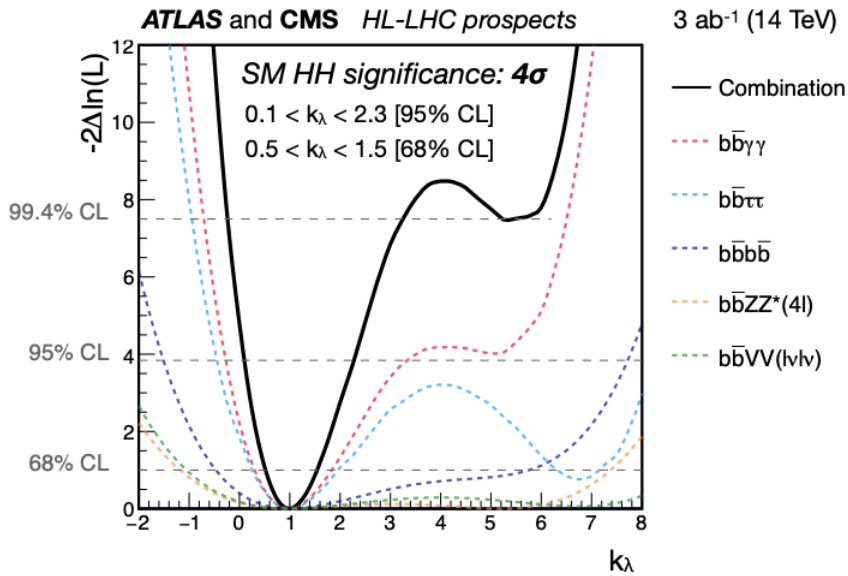
(b)

Figure 2.11: (a) Upper limit obtained by ATLAS on the cross-section of the ggF HH production as a function of κ_λ. The observed (expected) limits are shown as solid (dashed) lines.(b) Expected combined ATLAS and CMS likelihood for the searches for the HH production at the HL-LHC. [31]

Chapter 3

Collider Experiments

3.1 Luminosity

The two most essential features in particle accelerators are the center of mass energy, which determines the types of particles that can be produced in this facility, and its instantaneous luminosity, $L(t)$.

For a given process with cross-section σ, which gives the probability for the interaction to occur, the number of events that will be produced, N, over the lifetime of the operation of the machine, t, is:

$$\text{N} = \sigma \int L(t)dt, \tag{3.1}$$

where $L(t)$ measures the number of collisions per bunch crossing and is given by:

$$L = f\frac{n_1 n_2}{4\pi\sigma_x\sigma_y}, \tag{3.2}$$

where the number of particles in each brunch is n_1 and n_2, f is the bunch's collision frequency, and the transverse beam size in the horizontal and vertical directions are measured by σ_x and σ_y.

In the current particle accelerator experiments, the plan is always to maximize the statistical significance of an already measured process or increase the number of rare processes measured. For that we need to increase N as much as possible. To do so, we can increase the integrated luminosity, $\int L(t)dt$, or change the CM energy to maximize the process's cross-section compared to the ones of the relevant background.

As will be discussed later in Section 3.2, the FCC-ee is not alone in the quest to explore the properties of the Higgs boson and other SM particles with unprecedented precision: the International Linear Collider (ILC [32, 33]), the Compact Linear Collider (CLIC [34, 35]), and the Circular Electron Positron Collider (CEPC [36, 37]) are also in this race.

The baseline luminosities expected to be delivered in the four colliders are illustrated in Figure 3.1 at the Ref.[38, 39] time.

3.2 Future Colliders

Let's take a step backwards into the past, more precisely, on 4 July 2012. On that day, the ATLAS [3] and the CMS [2] collaborations made history by discovering a new particle: **the Higgs boson**. The discovery of the 125 GeV Higgs boson completes matrix of
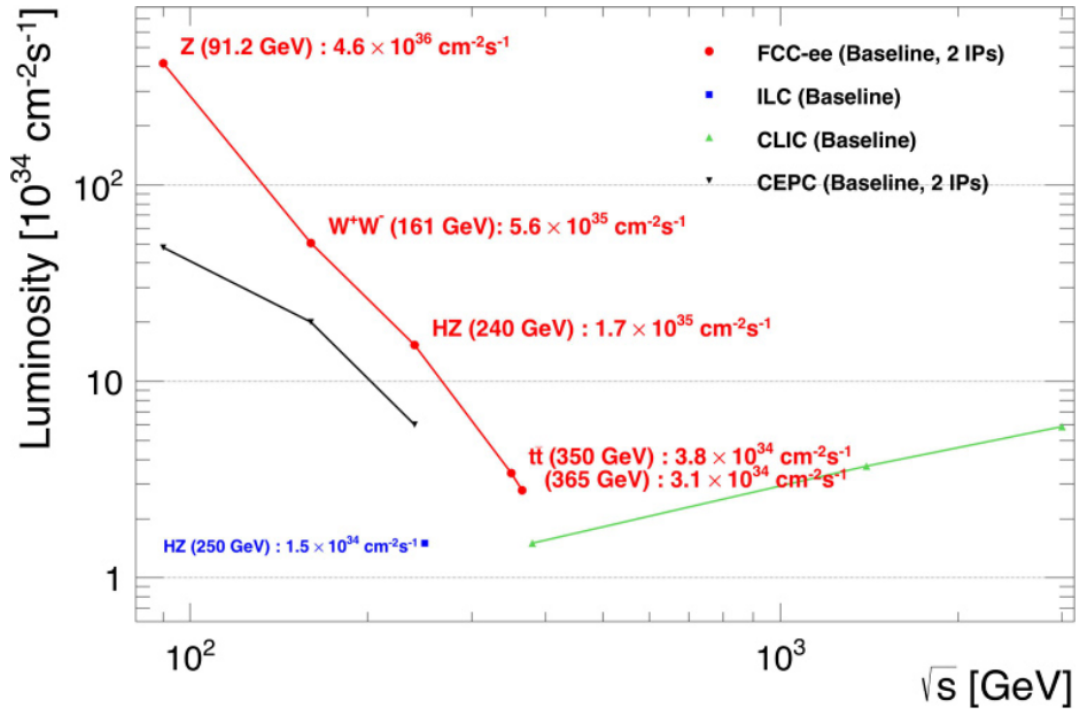
Figure 3.1: Baseline luminosities expected to be delivered as a function of the CM energy for each e+e- collider project (take from Ref.[38]).

particles and interaction constituting the Standard Model. As we know, this model has been a consistent and predictive theory, which has so far proven successful by colliders' experiments. Unfortunately, many experimental facts require the extension of the Standard Model, and explanations are needed for observations, like the domination of matter over antimatter, the evidence for dark matter and the non-zero neutrino masses.

Over ten years of physics, the LHC improved our knowledge about physics and the Standard Model, giving us a great legacy in our life that will be difficult to overcome. So, which type of machine can inherit its legacy?

The available choices are:

1. Hadron colliders: With those colliders, the mass range that can be reached in the final states is more extensive. Regardless of the signal-background ratio (S/B) being pretty low, the CM energy can only be accessed statistically via Parton Distribution Function (PDF) since they are not elementary particles but formed by them, more specifically, by quarks;

2. In Lepton colliders, the S/B ratio and the CM energy problems do not exist here and are more sensitive to electroweak states;

3. Circular colliders can have detectors in multiple Interaction Points (IPs) and reach high luminosity levels yet suffer energy loss via Synchrotron Radiation (SR);

4. Linear colliders are easy to upgrade in energy, and the beams are more smoothly polarized.

The Future Circular Collider (FCC) is arguably the leading candidate in this race. The FCC layout was published via the Conceptual Design Report (CDR) in 2018 [38],

Parameter	unit	2018 CDR [38]	2023 Optimised
Total circumference	km	97.75	90.657
Total arc length	km	83.75	76.93
Arc bending radius	km	13.33	12.24
Arc lengths (and number)	km	8.869 (8), 3.2 (4)	9.617 (8)
Number of surface site	-	12	8
Length (and number) of straights	km	1.4 (6), 2.8 (2)	1.4 (8), 2.031(4)
superperiodicity	-	2	4
Interaction Points (IP)	-	2	4

Table 3.1: FCC parameters in CDR and at FCCWeek2023[40]

presenting the last upgrades during FCCWeek2023 in Table 3.1. Nevertheless, the FCC project is one of many trying to study the Higgs properties:

- The International Linear Collider (ILC) [32, 33] will study the Higgs boson with a center of mass energy of 250 GeV, collecting data near the Higgsstrahlung process;

- The Compact Linear Collider (CLIC) [34] will reduce the CM energy from 500 to 380 GeV;

- The Circular Electron Positron Collider (CEPC) [36] with a plan to study the Higgs boson at 240 GeV;

- The Future e+e- Circular Collider (FCC-ee) [39] with a $\sim$ 90-100 km tunnel designed to be also a Higgs boson factory at 240 GeV;

Between the four Lepton colliders, the FCC-ee program is designed to deliver the highest rates in each CM energies, as seen in Figure 3.1, and achieve extreme statistical precision and experimental accuracy for its measurements. It can be said that the FCC-ee is the "*chosen one*" for this work.

3.3   Future Circular Collider

The FCC is designed to have a total of three phases: the first one consists of an e+ e- collider (FCC-ee CDR [39]) that will operate at multiple center of mass energies between 2045-2063, and the pp collider (FCC-hh CDR [41]) designed to run around 100 TeV, collecting a total luminosity of 20 ab^{-1} between 2070-2095. This last phase would be able to provide heavy-ion collisions, and its 50 TeV protons beams, with 60 GeV electron from an energy-recovery linac, would generate approximately 2 ab^{-1} of 3.5 TeV ep collisions at the FCC-eh. In general, the FCC program is estimated to last over seven decades for construction and operation, and over this time, is expected to improve results already known and reach new limits of physics.

In this work, we focus on FCC-ee at two different centers of mass energies and the IDEA detector, where both of these topics will be discussed in the next Section.

3.4   Future Circular Collider e+ e-

This FCC phase consists of using leptons, more precisely, electrons and positrons, as beam particles to answer open questions in physics. For that, the FCC-ee will run at five different center of mass energies to reach the maximum statistics possible of Z, W and Higgs bosons and top quarks.

Phase	Duration (years)	E_{CM} (GeV)	Integrated Luminosity (ab^{-1})	Event statistics
Z	4	88-95	150	10^{12} visible Z decays
WW	2	158-162	12	10^8 WW events
H	3	240	5	10^6 ZH events
tt(1)	1	340-350	0.2	$t\bar{t}$ threshold scan
tt (2)	4	365	1.5	10^6 $t\bar{t}$ events

Table 3.2: FCC-ee Run plan [38–40]

Each phase, Table 3.2, will focus on studying a specific physics scale, improving the results of already known observables, where[38, 39]:

- At the Z peak, they will improve the precision for the measurement of $\sin^2(\theta_W^{eff})$, QED coupling constant ($\alpha_{QED}(m_Z^2)$), both from the forward-backwards asymmetry, the Z mass (m_Z), from direct measurement, and the strong coupling constant ($\alpha_s(m_Z^2)$), from the ratio between the Z hadronic and leptonic widths [42–45];

- At the WW and tt threshold, the direct measurement of the W and the top masses using the respective cross-section[45–47];

- At the Higgs phase, the precision of the Higgs boson couplings (g_{HXX}) and total decay width (Γ_H) will reach new levels [48];

However, why do we need this FCC electron-positron phase? Can we skip this Lepton phase and move on to the hadron phase? Well, FCC-ee will indeed focus on improving previous measurements and increasing to another level those statistics. However, it is still a way to explore physics, digging into the physics we already know to search for new evidence about New Physics (NP). The best way to understand the importance of the FCC-ee is with this question: "How well do we know a certain result?" The answer is "straightforward": we must keep digging into the physics using a more powerful collider. If we observe some deviations from the results compared to the SM predictions, we are on the right path to discovering New Physics.

In our case, we want to study the Higgs properties and, find ways to improve the measurement of the Higgs self-coupling constant on this collider so, for that, we will focus on the phases that will study this boson, which means that we will use the center of mass energies of 240 GeV and 365 GeV.

3.5 FCC-ee Detector: IDEA detector

FCC-ee is expected to have a total of four interaction points, where a detector is placed at each IP: the CLIC-Like Detector (CLD) [49, 50], the International Detector for Electron-positron Accelerator (IDEA) [49, 51], and the other will be a Noble Liquid ECAL based but is still under study [49]. We have chosen the IDEA detector to use in our study.

The IDEA detector,Figure 3.2, is a 13mx11m detector composed of a silicon pixel vertex detector, a wire chamber surrounded by a layer of silicon micro-strip detectors, a thin, low-mass superconducting solenoid coil, a pre-shower detector, a dual-readout calorimeter, and muon chambers within the magnet return yoke, but this design is still under study.
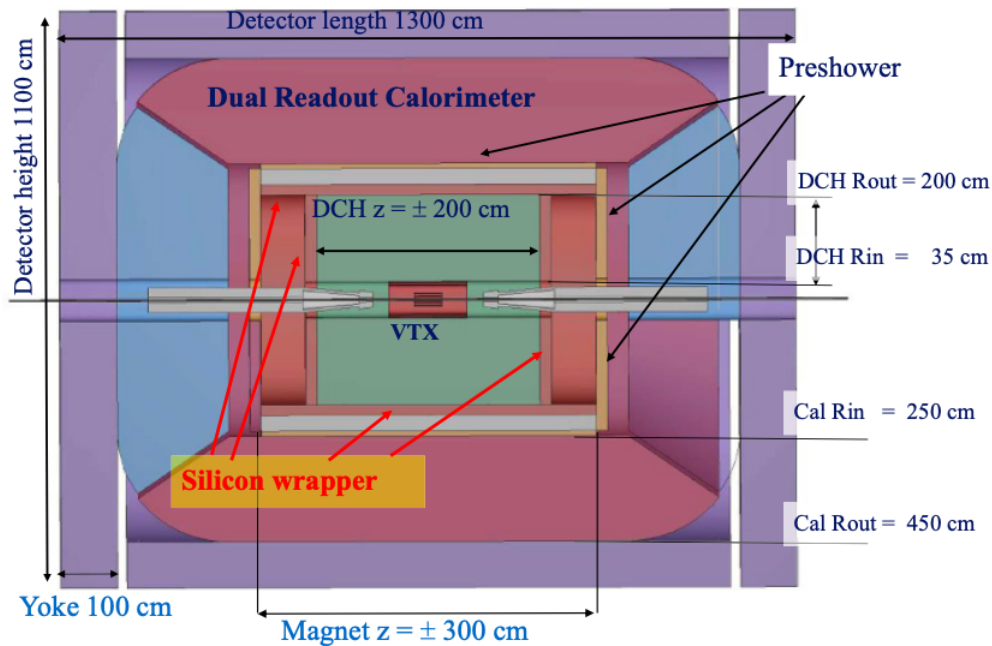
Figure 3.2: IDEA detector schematics [39].

For a precise determination of the impact parameter of the charged particle tracks, the innermost detector is a silicon pixel detector, based on monolithic pixel sensors, having a 0.3(1.0)% X_0[1] per innermost (outermost) layer. The results from the ALICE inner tracker upgrade [52] will be used for the vertex detector improvement.

From the detectors built for the KLOE[53] and MEG2[54, 55] experiments, the IDEA drift chamber will be a unique volume full-stereo, wire cylindrical chamber, high granularity, co-axial with the 2 T solenoid field, with low mass and short drift path. This detector's primary and most remarkable feature is its high transparency in terms of radiation lengths, where the total amount of material in the radial direction is of the order of 1.6%X_0, reaching about in the forward direction, 5.0%X_0. This drift chamber is 4m long, with an inner (outer) radius of 0.35 (2)m, filled with a gas mixture of 90%He-10%iC_4H_{10}, and a maximum drift time of $\sim$400ns.

In the simulations to study the performance of the IDEA tracking system present on the FCC-ee CDR[39], a seven-layer cylindrical vertex detector and a two-layer silicon

---

[1]X_0 corresponds to the mean length of the material at which the energy of an electron is reduced by the factor of 1/e, known as *Radiation length*.

wrapper, booth with a phi pitch of 20µm, were placed inside and around the Drift CHamber (DCH). The results of this study are presented in Table 3.3.

Parameter	Resolution
$\sigma(1/p_T)$	$a \oplus b/p_T$, $a \simeq 3 \times 10^{-5} GeV^{-1}$, $b \simeq$ -6$\times 10^{-3}$
σ_{d_0}	$a \oplus b/\sin^{3/2}\theta$, $a=3\mu m$ $b=15\mu m GeV$
angular resolution	better than 0.1mrad in both azimuthal and polar angle
σ_E/E	$10\%/\sqrt{E}$ for isolated e-, and $30\%/\sqrt{E}$ for isolated π

Table 3.3: IDEA resolution parameters[39, 56]

The IDEA has the preshower detector located between the magnet and the calorimeter in the barrel region and between the drift chamber and the end-cap calorimeter in the forward region. In the barrel region, the magnet coil works as an absorber of about $1X_0$, followed by one layer of Micro Pattern Gas Detector (MPGD), where the second layer of chambers follows after another $1X_0$ lead. At the forward region, a similar construction occurs where both absorber layers are made of lead. Surrounding the second layer is a 2m deep lead-fiber dual-readout calorimeter. This calorimeter provides exceptional intrinsic discrimination between muons, electrons/photons and hadrons for isolated particles, and, with that, the fine transverse granularity allows the separation of close showers, providing a high-quality matching to tracks in the inner and the outer detector elements, making this calorimeter excellent for particle-flow reconstruction.

3.6 FCC-ee: Higgs factory

According to the baseline run plan [39], the FCC-ee is designed to operate as a Higgs factory for seven years, of which three are at 240 GeV and four at 365 GeV. During this period, the FCC-ee will measure the various cross-section times branching ratios at these energies from the Higgsstrahlung process, $e^+e^- \rightarrow$ ZH, and the W fusion process, $e^+e^- \rightarrow \bar{\nu}_e\nu_e$H.

From the one million ZH events expected from the FCC-ee, the total σ_{ZH} can be determined with a statistical precision of 0.1%, if the ZH events selection is 100% efficient and pure. By counting the ZH events with a leptonic Z decay, Z$\rightarrow l^+l^-$, for which the recoil mass against the lepton pair is around the Higgs boson mass (Section 6.3), the total ZH cross-section is determined in a model-independent fashion. Assuming that the coupling structure is identical in form to the SM, the σ_{ZH} and $\sigma_{\bar{\nu}_e\nu_e H}$ are proportional to the square of the Higgs boson coupling to the Z, g_{HZZ}, and to W,g_{HWW}, respectively. Once the g_{HZZ} has been determined, all other couplings can be accessed by measuring the cross-section for each exclusive Higgs boson decay,

$$\sigma_{ZH} \times BR(H \rightarrow X\overline{X}) \propto \frac{g_{HZZ}^2 \times g_{HXX}^2}{\Gamma_H} \quad (3.3)$$

$$\sigma_{\bar{\nu}_e\nu_e H} \times BR(H \rightarrow X\overline{X}) \propto \frac{g_{HWW}^2 \times g_{HXX}^2}{\Gamma_H} \quad (3.4)$$

For example, the ratio of W fusion to Higgsstrahlung cross-sections for the same Higgs boson decay yields g_{HWW}, and the Higgsstrahlung rate with H→ZZ decay provides a

$\sqrt{s}$ [GeV]	240		365	
Integrated Luminosity [ab^{-1}]	5.0		1.5	
Channel	ZH	$\bar{\nu}_e\nu_e$H	ZH	$\bar{\nu}_e\nu_e$H
H $\to$ any	±0.5		±0.9	
H $\to$ b$\bar{\text{b}}$	±0.3	±3.1	±0.5	±0.9
H $\to$ c$\bar{\text{c}}$	±2.2		±6.5	±10
H $\to$ gg	±1.9		±3.5	±4.5
H $\to$ W$^+$W$^-$	±1.2		±2.6	±3.0
H $\to$ ZZ	±4.4		±12	±10
H $\to$ $\tau^+\tau^-$	±0.9		±1.8	±8
H $\to$ $\gamma\gamma$	±9.0		±18	±22
H $\to$ $\mu^+\mu^-$	±19		±40	
H $\to$ invisible	< 0.3		< 0.6	

Table 3.4: Relative uncertainty (in %) on $\sigma_{\text{ZH}} \times BR(\text{H} \to \text{X}\overline{\text{X}})$ and $\sigma_{\nu_e\bar{\nu}_e\text{H}} \times BR(\text{H} \to \text{X}\overline{\text{X}})$, as expected from the FCC-ee data at 240 and 365 GeV [39, 57, 58]

determination of the Higgs total decay width Γ_H. The expected statistical uncertainties for the cross-section times branching ratio are listed in Table 3.4, while Table 3.5 yields the precision of a few Higgs couplings.

Coupling	Precision (κ framework/EFT)
g_{HZZ}	0.17 / 0.26
g_{HWW}	0.41 / 0.27
g_{Hbb}	0.64 / 0.56
g_{Hcc}	1.3 / 1.2
g_{Hgg}	0.89 / 0.82
$g_{\text{H}\tau\tau}$	0.66 / 0.57
$g_{\text{H}\mu\mu}$	3.9 / 3.8
$g_{\text{HZ}\gamma}$	10 / 9.3
$g_{\text{H}\gamma\gamma}$	1.3 / 1.2
g_{Htt}	3.1 / 3.1
Γ_H	1.1

Table 3.5: Precision on g_{HXX} and on Γ_H at FCC-ee, in the κ framework and in a global Effective Field Theory fit [57, 58].

Being the lepton collider with the highest luminosity delivered at 240 and 365 GeV, the FCC-ee has the sensibility to measure the quantum corrections from loops at single Higgs observables, such as the cross-sections of ZH and W fusion processes in Fig-
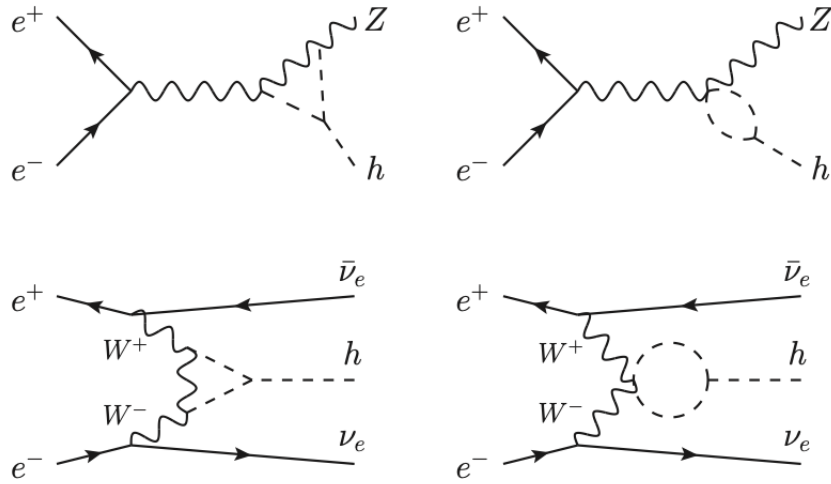
Figure 3.3: Higgsstrahlung and W fusion at NLO involving the Higgs self-coupling..

ure 3.3. Through the dependence of σ_{ZH} with the center of mass energy, it is possible to determine the g_{HHH} and g_{HZZ} couplings through a global (Higgs and EW) fit, with a relative precision presented in Figure 3.4. By including all the energies in the fit, a precision of $\pm 33\%$ is achieved [39, 57, 58].
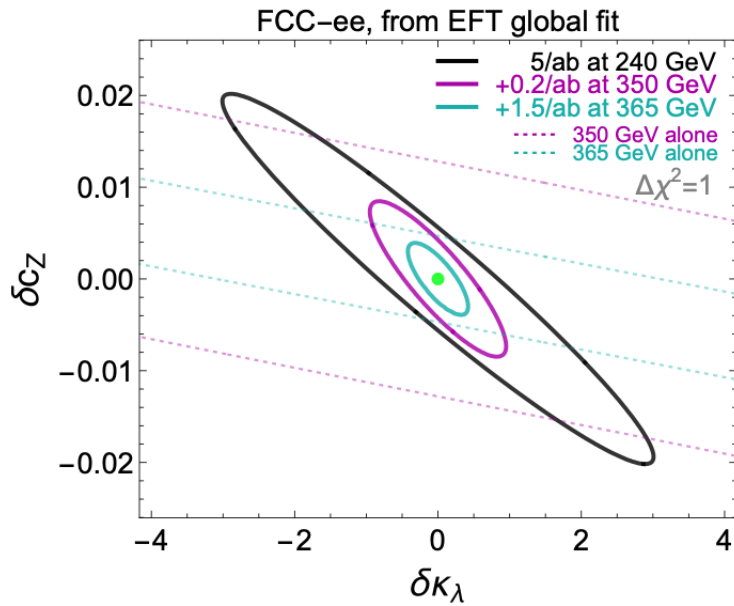
Figure 3.4: Relative precision in the simultaneous determination of the Higgs self-coupling (denoted as κ_λ) and the HZZ/HWW coupling (denoted as c_z) at FCC-ee, with 240 GeV (black ellipse), 350 and 365 GeV (purple and greed chased) data, and by the combination of the data at 240 and 350 GeV (purple ellipse), and at 240, 350, and 365 GeV (green ellipse) [39]

Chapter 4

Analysis Tools and Event Reconstruction

In the previous Section, we discussed the collider and the detector we want to use in our study. Since the FCC-ee is still in the approval phase, and it will take a long time to be built, only samples generated via a Monte Carlo program was analyzed. The programs used in this study will be discussed in this Section.

This Section introduces the programs used in this study from the sample generations to analysis.

4.1 MadGraph5

In this study, we use the following programs. For the Monte Carlo samples, we have MadGraph5_aMC@NLO [59], Pythia8 [60] for the showering and hadronization, and the detector response is parameterized using Delphes [61].

MadGraph 5 (MG5) is a framework designed to provide all SM and BSM phenomenology elements, such as cross-sections and the generation of hard events. This matrix-element generator allows the user to specify the desired process in terms of the initial and final states. It is a very straightforward program for those that want the cross-section. However, the MG5 allows the user to do much more than specify the process, like giving the user freedom to impose additional constraints, such as forcing and forbidden channel resonances, excluding internal particles, forced decay chains of final state particles, and the type of order (tree-level, NLO or Loop-induced) process.

In addition to the process and its type, the MadGraph5 has many physical models, such as the Standard Model, Two-Higgs-doublet model (**2HDM**) and Higgs Effective Field Theory (**heft**). It also permits the user to impose restrictions on the same models. Each model has its own set of particles and parameters, so to compare different models, we need to pay attention to the parameters' values and change them. We use the MadGraph5 default model **sm**, for the tree-level process, with its own set of parameters, and the **loop_qcd_qed_sm** for the NLO [62] process. In order to have coherence between simulations, when **loop_qcd_qed_sm** model was used, the parameters listed in Table 4.1 were changed to their values in **sm** model.

According to the Paticle Data Group (PDG) database [5], the Higgs total width is about 3.2 MeV. However, a 6.382 MeV Higgs total width was used in both models. In Subsection 5.2.1, a justification is presented for not changing this parameter.

After the MadGraph5 simulation, its output will go through the user's preferred

Parameter	Value at MG5 model	
	sm	**loop_qcd_qed_sm**
M_Z [GeV]	91.188	
α_{EW}^{-1}	132.507	128.993
Γ_Z [GeV]	2.441	2.4889
Γ_H [GeV]	6.382×10^{-3}	4.187×10^{-3}

Table 4.1: MG5 parameters for the **sm** and the **loop_qcd_qed_sm** models.

shower simulated, which, in our case, is the Pythia8.

4.2 Pythia8

Like MadGraph5, Pythia8 [63] is a standard tool for high-energy collision simulations incorporating physical models for the evolution from a few-body high-energy scattering process to a complex multihadronic final state. These particles are produced in vacuum. However, implementing the interaction with detector material is only included in Pythia with external detector-simulation codes.

Pythia8 was used only in this work to simulate the showering, the hadronization process. Getting the MadGraph5 output file as an input, the Pythia8 program can decay the unstable particles, simulate the initial and final state showers, and the partons' hadronization. A log file with the showering and hadronization history is created, where each particle has a status code that describes the reason for being added to the process, if they are a decay product, and to which particle it decays.

After Pythia8 is done with the simulation, a HepMC file [64] is created and ready to pass through a detector simulator like Delphes.

4.3 Delphes: Detector simulation and event reconstruction

Delphes [61] was designed to perform a fast and realistic simulation of a general-purpose collider detector for phenomenological studies. Its framework comprises a simulation of a track propagation system embedded in a magnetic field, electromagnetic and hadron calorimeters, and a muon identification system. Physical objects, such as tracks and energy deposits, leptons, jets, and missing energy, can be reconstructed from the detector response. For the output, a ROOT [65, 66] file is created.

A uniform axial magnetic field parallel to the beam direction deflects the long-lived charged particles. Depending on the particle charge, they can follow a helicoidal trajectory from the interaction point to a calorimeter cell if they are charged particles or have a straight-line trajectory if they are neutral. The user can define the probability of a charged particle being reconstructed as a track. The track system takes advantage of the trajectory of charged particles to reconstruct their momentum, optimal for low p_T. The user can specify the tracking efficiency, energy, and momentum resolutions, and the transverse momentum and pseudo-rapidity dependent on the particle type.

In Delphes, the calorimeters are described by a (η, ϕ) plane with the cell size defined in a configuration file. The user defines the amount of particle energy deposited in the Electromagnetic Calorimeter (ECAL), responsible for the electrons and photons energy measurements, and in the Hadron Calorimeter (HCAL), responsible for measuring the energy of long-lived charged and neutral hadrons. Although in Delphes, depending on the type of particle, all energy is deposited in ECAL or HCAL, the user is allowed to control the deposited energy fraction to simulate a more realistic detector. The energy resolutions of ECAL and HCAL are parameterized as a function of η and include the stochastic, noise, and constant terms (S, N, and C):

$$\left(\frac{\sigma}{E}\right)^2 = \left(\frac{S(\eta)}{\sqrt{E}}\right)^2 + \left(\frac{N(\eta)}{E}\right)^2 + C(\eta)^2. \tag{4.1}$$

A log-normal distribution independently smears both energy deposits. The coordinate where the energy is deposited is called the tower, and the ECAL and HCAL cells are grouped in a calorimeter tower.

For electrons and muons, the user can specify the efficiency of being reconstructed. This reconstruction probability is null outside the tracker acceptance and for a particle momentum below some threshold. Besides this reconstruction, Delphes enables the user to change the isolation parameterization. The activity in its vicinity describes the isolation of a particle candidate. To determine if a reconstructed particle P ($P = e, \mu, \gamma$) is isolated or not, Delphes divides the sums of the transverse momentum above p_T^{min} of all particles that are inside a cone of radius R around the particle P, except P, by its transverse momentum. If the result of this division, $I(P)$, is lower than I_{min}, the particle is isolated.

4.3.1 Jet Algorithms

In a particle accelerator, the particle beam consists of particle clusters split into bunches colliding with the other bunches coming from opposite directions, producing clusters of leptons and partons. However, due to the QCD confinement property, allowing only colorless states to be free, the partons must be confined inside hadrons produced via hadronization processes. Once produced, focused bunches of stable hadrons are referred to as jets.

Jets tend to be visually apparent structures when one looks at an experimental event display, being able to assemble the idea of the original parton that produced them with energy and direction measurements. These objects hold a significant role in physics analysis, so one needs rules that project a set of particles onto a set of jets. This projection is referred to as a jet algorithm.

It is possible to split jet algorithms into cone algorithms and sequential recombination algorithms. The first type of algorithm assumes that jets' particles are in conical angular regions, resulting in jets with rigid circular boundaries. In comparison, a sequential recombination algorithm consists of identifying the closest pair of particles in some distance measure, recombining them, and repeating this procedure until some stopping criterion is reached.

A crucial property of jet algorithms is that they need to be infrared and collinear safe. This safety means that the jet properties should not depend on the presence of soft partons (infrared safe) and be able to recognize the number of jets in an event regardless of the collinearity of the particles (collinear safe).

The most common jet algorithms used are the k_t [67], the anti-k_t [68], and the Cambridge/Aachen (C/A) [69]. They are based on the following distance measures:

$$d_{ij} = \min(p_{ti}^{2p}, p_{tj}^{2p})\frac{\Delta R_{ij}^2}{R^2} \tag{4.2a}$$

$$d_{iB} = p_{ti}^{2p}. \tag{4.2b}$$

For p=-1, 0, and 1, the above algorithm reduces to anti-k_t, Cambridge/Aachen, and k_t, respectively. The formula parameters are referred to as a distance measure, d_{ij}, between all pair of particles i and j, the distance between the particle i with the beam (B), d_{iB}, transverse momentum, and $\Delta R_{ij}^2 = (y_i - y_j)^2 + (\phi_i - \phi_j)^2$, with rapidity, y_i, and the azimuth ϕ_i of particle i, R is the jet-radius parameter, which determines its angular reach. The jet algorithm is formulated as follows:

1. for each pair of particles i,j work out d_{ij} and d_{iB} distances;

2. find the minimum between the two distances. If $d_{ij} < d_{iB}$ merges both particles into a single particle, often called a "pseudojet"; if $d_{iB} < d_{ij}$ then the particle i is declared as a final jet and removed from the list;

3. repeat this cycle until no particles are left;

4. only the ones above some transverse momentum, p_T^{min}, are used for the final jets;

Besides these jet algorithms, the `FastJet` package [70], integrated into Delphes, also includes jet algorithms for lepton collisions. The one used for this analysis is the **Generalised k_t algorithm for e^+e^- collisions** [71]. This jet algorithm is defined as follows:

$$d_{ij} = \min(E_i^{2p}, E_j^{2p})\frac{(1 - \cos\theta_{ij})}{(1 - \cos R)} \tag{4.3a}$$

$$d_{iB} = E_i^{2p}, \tag{4.3b}$$

for a general value of p and R. The new parameter, θ_{ij}, is the angle between the particles i and j. For R < π, this algorithm behaves in analogy with the previous algorithms. When an object is at an angle $\theta_{iX} > R$ from all other objects X, it forms an inclusive jet. For values of R> π, the factor is replaced by $(3 + \cos(R))$. The only time a d_{iB} will be relevant is for events with just a single particle, as long as R < 3π.

Jets are a crucial component in the analysis, so their reconstruction needs to be accurate. It is possible to produce jets after showering and hadronization, tracks, calorimeter towers, or particle-flow tracks and towers. They are called generated, track, calorimeter, or particle-flow jets. On the generated jets, no detector simulation nor reconstruction was considered. The user can decide the jet clustering algorithm, its parameters, and the minimum threshold for the jet transverse momentum to be stored in the final collection.

4.3.2 b and τ jets

Identifying b quark jet (b-jet) or a jet initiated by the hadronic decay of a τ lepton (tau-jet) is essential in many physics analyses. In Delphes, a jet becomes a potential b or τ

jet candidate if a generated b or τ, respectively, is found within some distance $\Delta R_{jet,b/\tau}$ of the jet axis. The user also can define the parameters for the tagging efficiency. The probability of mis-tagging, i.e., wrongly identifying a particle as a b or a τ, can be changed by the user.

4.3.3 Particle-flow Reconstruction

Delphes can reconstruct jets using only the information from HCAL+ECAL towers or a particle flow algorithm that combines the information from the tracking system and the HCAL+ECAL tower. In this work, we performed the analysis using the particle flow jets (or *eflow*), so we briefly describe them here. In actual experiments, the tracking resolution is better than the calorimeter resolution until some energy threshold. In Delphes, estimating charged particle momenta via the tracker is always assumed to be convenient.

For each calorimeter tower, the particle-flow[61] counts :

- the total energy deposited in ECAL, E_{ECAL}, and HCAL, E_{HCAL};

- $E_{ECAL,trk}$ and $E_{HCAL,trk}$, the total energy deposited respectively in ECAL and HCAL originating from charged particles for which the track has been reconstructed;

then defines;

$$\Delta_X = E_X - E_{X,trk}, \text{ with } X = ECAL, HCAL \tag{4.4}$$

$$E_{Tower}^{eflow} = \max(0, \Delta_{ECAL}) + \max(0, \Delta_{HCAL}) \tag{4.5}$$

Where each reconstructed track results in a particle-flow track. Suppose $E_{Tower}^{eflow} > 0$, a particle flow tower is created with energy E_{Tower}^{eflow}. The particle-flow tower and tracks are then input for the jet algorithms.

Considering, as an example of the algorithm, a single charged pion is reconstructed as a track with energy E and deposits some energy in the HCAL. If $E_{HCAL} \leq E_{HCAL,trk}$, only a particle-flow track with energy $E_{HCAL,trk}$ is created. However, if $E_{HCAL} > E_{HCAL,trk}$, a particle-flow track of energy $E_{HCAL,trk}$ and a particle-flow tower with energy E_{HCAL} are produced;

In that way, the particle-flow tracks contain charged particles estimated with a good resolution. In contrast, the particle-flow towers contain, in general, a combination of neutral particles, charged particles with no corresponding reconstructed tracks, and additional excess deposits induced by positive smearing of the calorimeters and are characterized by a lower resolution.

As a detector simulator program, Delphes allows the user to choose the detector to be used. Each detector has a specific file, a card, as Delphes calls it, to simulate the detector response. These cards contain all the detector information, from layout to efficiency formulas and jet algorithm.

Chapter 5

Sample Simulation

At Lepton colliders, the Higgs boson production strongly depends on the center of mass energy of the collider and, to some extent, on the Higgs boson mass. The cross-section of various production channels of this boson is displayed in Figure 5.1:
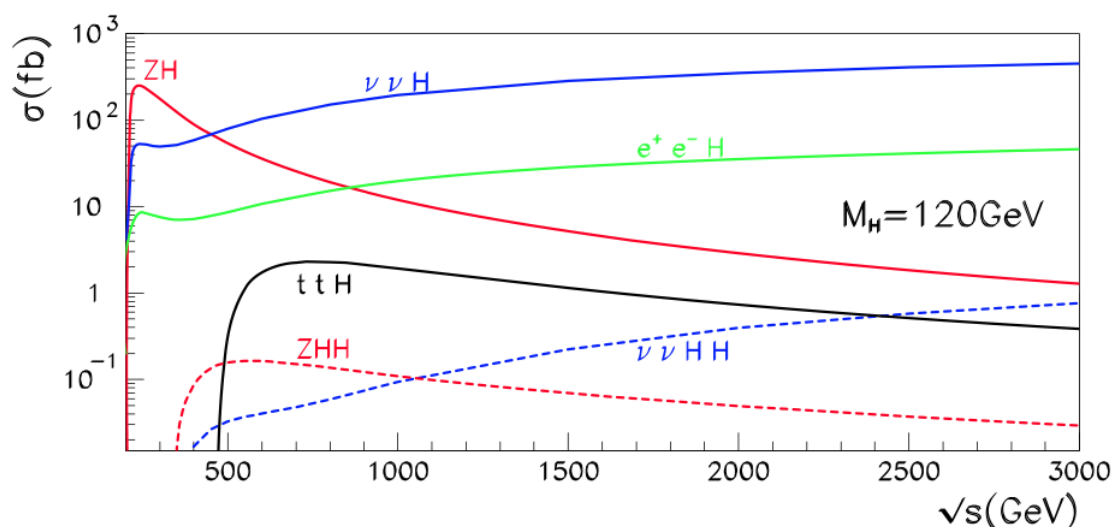
Figure 5.1: Main Higgs boson cross-sections as a function of $\sqrt{s}$ at e+e- collider [72].

Where the lines have the following correspondence with the channels: full red line to Higgsstrahlung, blue line to W fusion, green line to Z fusion, black to $t\bar{t}$ associated production, and the dashed lines represent the same production channel as the full lines but now refer to the production of Higgs boson pairs. More details about each production channel can be found in Ref.[73].

As shown in Figure 5.1, the Higgs boson is mainly produced via the Higgsstrahlung (ZH) and W fusion (WW-fusion) processes at energies below 900GeV. At the center of mass energies of 240 GeV, with a cross-section of 200 fb, as is shown in Figure 5.2, FCC-ee is expected to deliver about one million HZ events with an integrated luminosity of $5ab^{-1}$, which will be complemented with 180 000 HZ events and 45 000 WW-fusion events at 365 GeV , assuming an integrated luminosity of 1.5 ab^{-1} at that $\sqrt{s}$.

As presented at Ref.[74, 75], the Higgsstrahlung process is the primary process at Leptons colliders, mediated by a Z boson, to produce the Higgs boson. By increasing the center of mass energy, this s-channel process loses its dominance to the WW-fusion
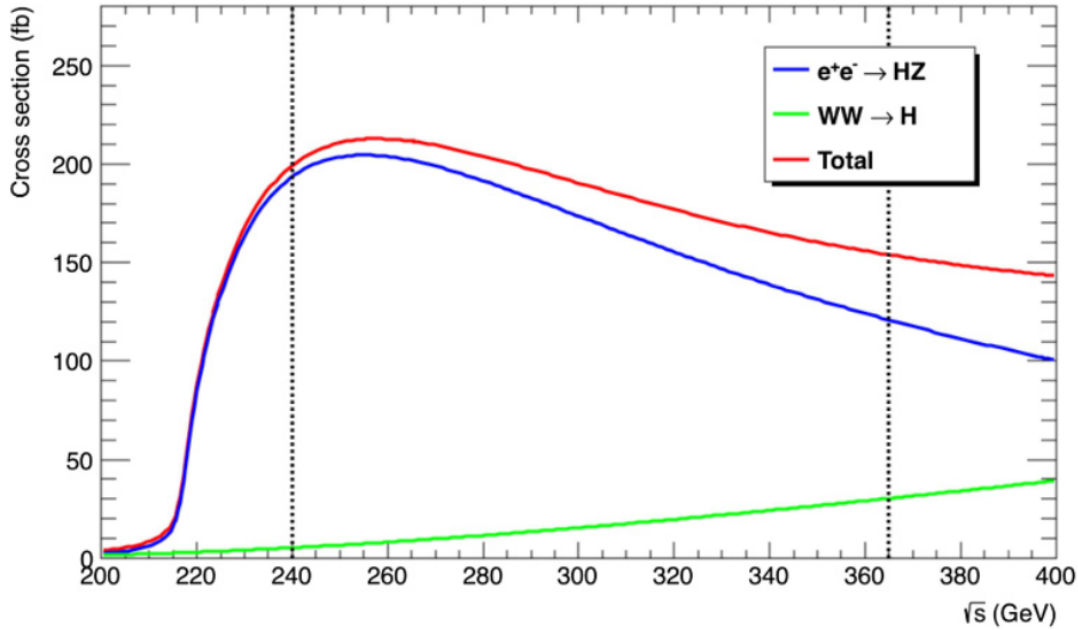
Figure 5.2: Higgs boson production cross-section as
a function of the CM energy (taken from Ref.[39]).

between 440-460 GeV, and, around 900 GeV, the Z-fusion channel exceeds its and becomes the second most dominant. This last exchange of dominance comes from the fact that the Higgsstrahlung cross-section is proportional to the inverse of the center of mass energy, $1/s$, while the cross-section of the t-channel is proportional to $\ln(s^2)$.

This work will only focus on the single Higgs and di-Higgs production channels mediated by the Z boson: the Higgsstrahlung process and Z-fusion at $\sqrt{s} = 240$ and 365 GeV. This last channel is the third most dominant channel to produce the Higgs boson, as seen in Figure 5.1 . However it can improve the amount of statistics at both energies.

5.1 Di-Higgs production

This thesis aims to study the Higgs boson self-coupling constant, λ_{hhh}, and observe ways to improve its measurement at the FCC-ee. So, for our first attempt, we simulate the process that can give us the desired coupling constant: the di-Higgs production:

$$e^+ e^- \rightarrow e^+ e^- h h \,, \text{with } h \rightarrow b\bar{b}$$

Using MG5, we generate this process for a CM energy range of [280,600] GeV while forcing the Higgs boson to decay to a pair of b quarks. Of all Higgs decays, this one holds the highest branching ratio. Only two of the eight Feynman diagrams are affected by λ_{hhh} (see Figures 5.3a and 5.3b).

As revealed in Figure 5.4, the cross-section will be $\mathcal{O} \propto (10^{-8} - 10^{-2})$ fb for the center of mass energies mentioned above. The FCC-ee will run at energies of 365 GeV, delivering 0.68 di-Higgs events for an expected integrated luminosity of 1.5 ab^{-1}, as stated in Table 5.1.

35

(a) s-channel

(b) t-channel

(c) without λ_{hhh}
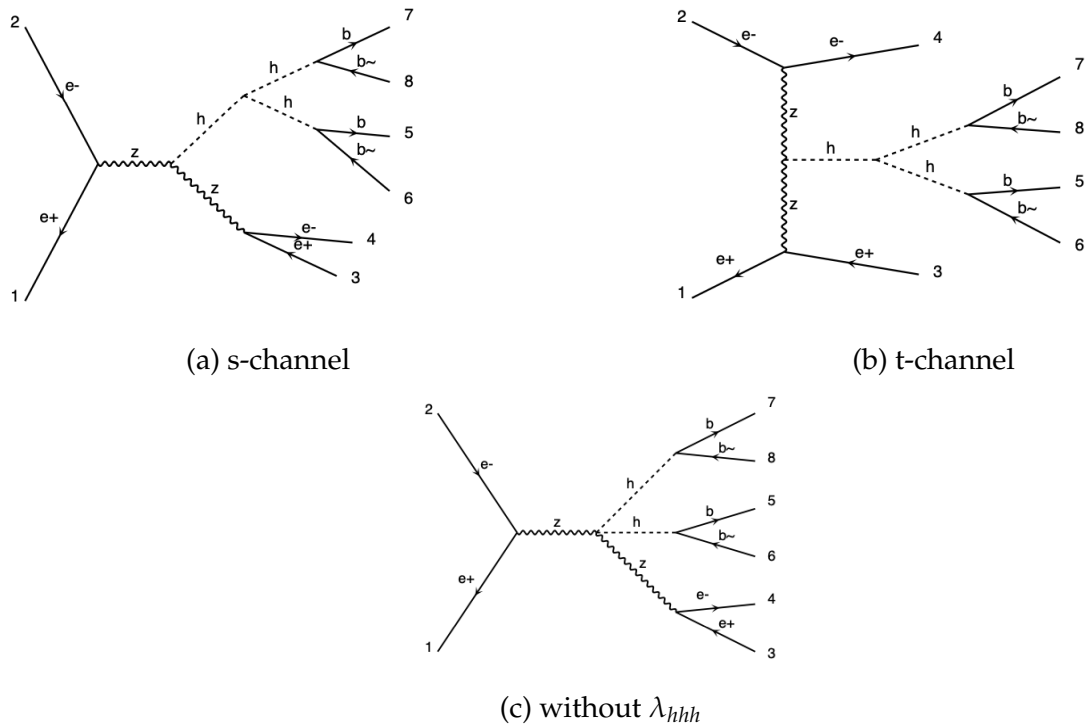
Figure 5.3: Di-Higgs production with Higgs decay into a b-quark pair.
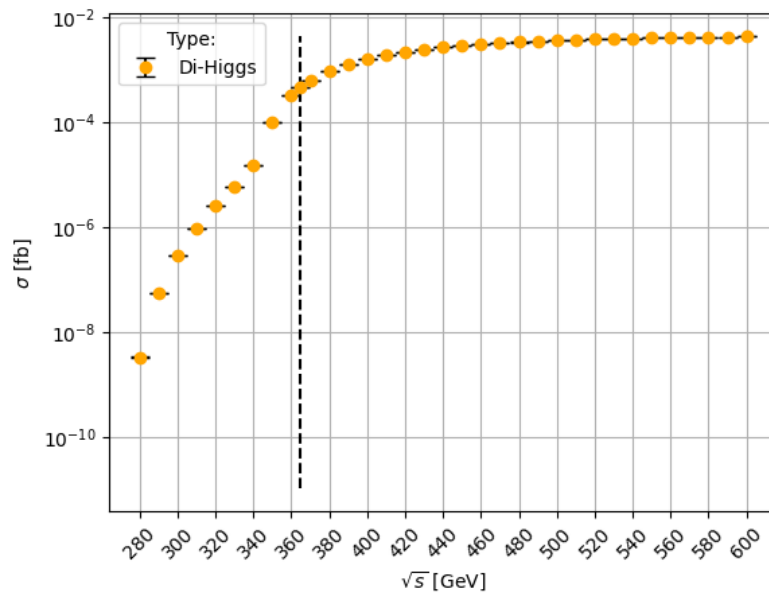
Figure 5.4: Di-Higgs cross-section for $\sqrt{s} \in [280, 600]$GeV.

Suppose we desire to acquire at least one event. The integrated luminosity must be at least 2.21 ab^{-1}, but even with that, we will only hold one event, which is negligible compared to the global statistics.

36

$\sqrt{s}$ [GeV]	$\mathcal{L}$ [ab^{-1}]	Process	σ [fb]	Events
365	1.5	$e^+\,e^- \to z\,h\,h$	$2.007(1)\times10^{-2}$	30.11
		$e^+\,e^- \to e^+\,e^-\,h\,h,\ h \to b\bar{b}$	$4.523(15)\times10^{-4}$	0.68

Table 5.1: Number of di-Higgs events at $\sqrt{s}$= 365
GeV, without and with Z $\to e^+e^-$ and H $\to b\bar{b}$ decay.

5.2 Single Higgs production

As shown in Table 5.1, the di-Higgs production in the FCC-ee is negligible, making it impossible to observe directly the λ_{hhh}. According to Ref.[76], Ref.[4] proposed to measure the Higgs self-coupling via the quantum corrections it induces in single Higgs channels. In addition to reinforcing this fact, Ref.[25, 57] shows that the loop contributions to the Higgsstrahlung process cross-section amounts to ~2% at 240 GeV and ~0.5% at 365 GeV. In order to improve the measurement and its precision of λ_{hhh}, this work will focus on the production channels mediated by the Z boson for the single Higgs production. For that, three samples were simulated: Higgsstrahlung, Z-fusion, and eeHee. The first two samples are the simulations corresponding to the Higgsstrahlung and Z-fusion channels, and the third one corresponds to both channels together plus the interference between them. These simulations were generated at Leading Order (LO), tree- and loop-level, using version 3.4.2 of MG5, while the eeHee was also generated at Next Leading Order (NLO) with MG5 version 3.5.1.

MadGraph5 version 3.4.2 was the first and the main version used in this work. In order to generate the λ_{hhh} in this version, we generate the desired process via a loop-induced process (loop-level) [77]. The loop-induced process is a process where their LO contribution already comes from loop amplitudes. An example of this process is the Higgs production via gluon fusion, see Figure 2.9a. In the most recent version, the MadGraph5 allows us to generate an NLO process, where the amplitude of tree-level and loop-induced processes and their interference are included [62, 78–81].

5.2.1 Signal

For the LO level, the three signal channels were simulated at 240 GeV and 365 GeV without any cuts at the MG5 level.

- **Higgsstrahlung**: e+ e- $\to$ z $\to$ e+ e- h [1]:

  - tree-level: Figure 5.5a;
  - Loop: Figures 5.6a and 5.6c;

- **Z-fusion**: e+ e- $\to$ e+ e- h \$\$z [1]:

  - tree-level:Figure 5.5b;
  - Loop: Figures 5.6b and 5.6d;

[1]Commands used to generate the process.

- **eeHee**[2]: e+ e- → e+ e- h [1]:

  – tree-level: Figure 5.5;

  – Loop: Figure 5.6 ;
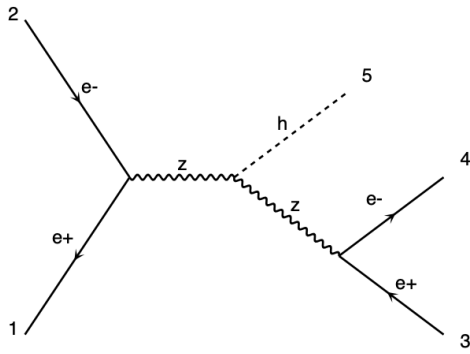
(a) Tree-level: s-channel
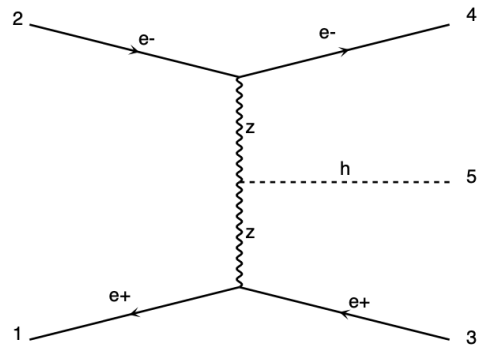
(b) Tree-level: t-channel

Figure 5.5: Tree-level: Single Higgs boson production via lepton collisions
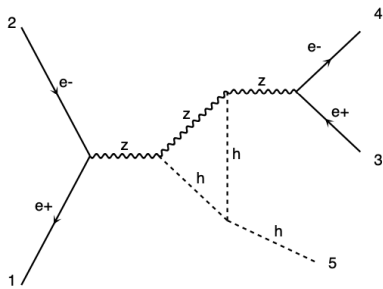
(a) Loop: s-channel with the
Higgs self-coupling constant
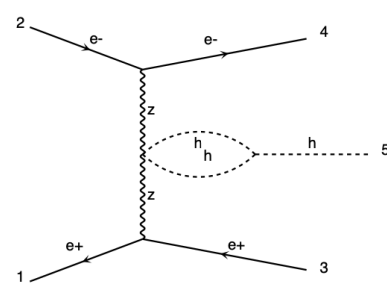
(b) Loop: t-channel with the
Higgs self-coupling constant
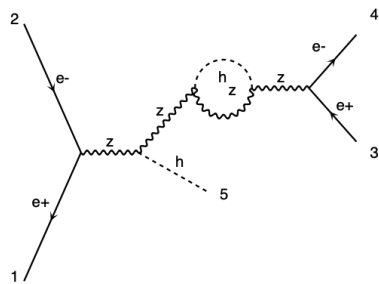
(c) Loop: s-channel without the
Higgs self-coupling constant
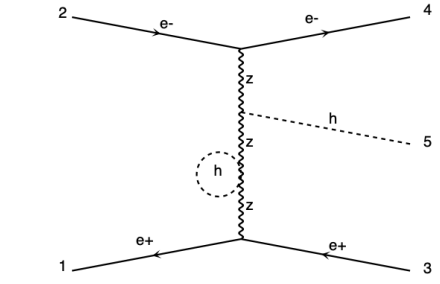
(d) Loop: t-channel without the
Higgs self-coupling constant

Figure 5.6: Loop: Single Higgs boson production via lepton collisions

As presented in Section 4.1, we used the MG5 default model, **sm**, for the tree-level process. For the loop and NLO processes, the model **loop_qcd_qed_sm** was used, where a change of parameters was needed to study these processes in different models. We also refer to the strangeness of changing Γ_H to 6.4 MeV instead of 3.2 MeV, as shown

---

[2]This will be our main signal. This process correspond to the combination of the Higgsstrahlung and Z-fusion processes with their interference.

in Table 4.1. This modification is because MadGraph5 uses the Breit-Wigner resonance formula, presented in Appendix.A, to calculate the cross-section, which considers the particle's mass, total width, and center of mass energy. So, if we use a value too small, the cross-section values will change and can make no physical sense, as demonstrated in Appendix.B.

To verify if the simulation was run appropriately, the tree-level cross-section dependency with $\sqrt{s}$ for Higgsstrahlung, Z-fusion, and the eeHee is the best way since their behavior with energy increase is known.
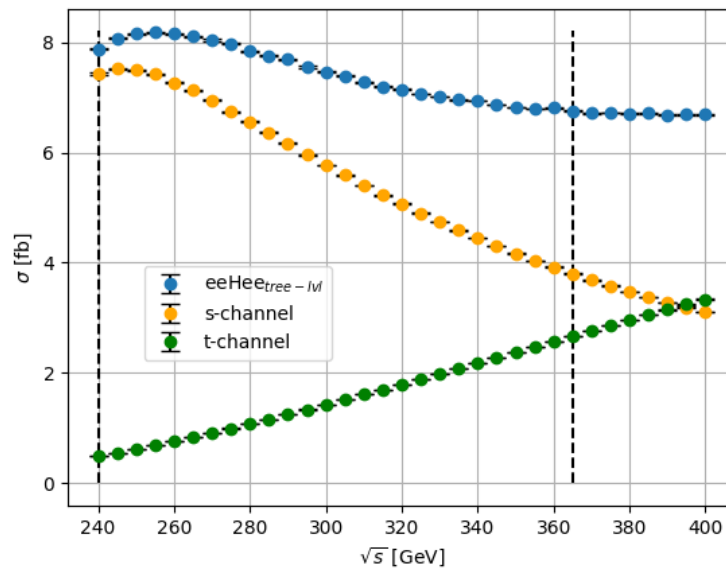
Figure 5.7: Higgsstrahlung and Z-fusion cross-section as a function of the CM energy.

As is possible to observe from Figure 5.7, our simulated channels show us a similar behavior as shown in Figure 5.2. At low energies, the s-channel is the primary process for the Higgs production, but for 365 GeV, both channels have cross-sections close to each other.

In Figure 5.8, it is shown the cross-section behavior through the increase of $\sqrt{s}$ for the sample eeHee at tree-level and NLO. The upper plot shows the variation of their cross-sections, while the lower plot corresponds to the quantum corrections from the loop diagrams being 7.32% and 10.91%, while the loop diagrams, alone, contribute 0.79% and 0.52% at 240 and 365 GeV, respectively.

In Tables 5.2 and 5.3, the cross-sections for each process and at each level for both energies, it is observed that the highest contribution to the cross-section of the eeHee comes from the s-channel, which makes sense since this is the leading channel for single Higgs production at lepton collisions.

5.2.2 Background

The main backgrounds for the Higgs production are $e^+ \; e^- \; \rightarrow \; e^+ \; e^- \; b \; \bar{b}$ (eebbee), Figure 5.9, and $e^+ \; e^- \rightarrow t \; \bar{t} \; (t\bar{t})$. The first background process was generated at 240 and 365 GeV, composed of all the processes with a $e^+e^-b\bar{b}$ in the final state. At CM energy of 365 GeV, the FCC-ee will be at the top quark phase, having the $t\bar{t}$ production as the
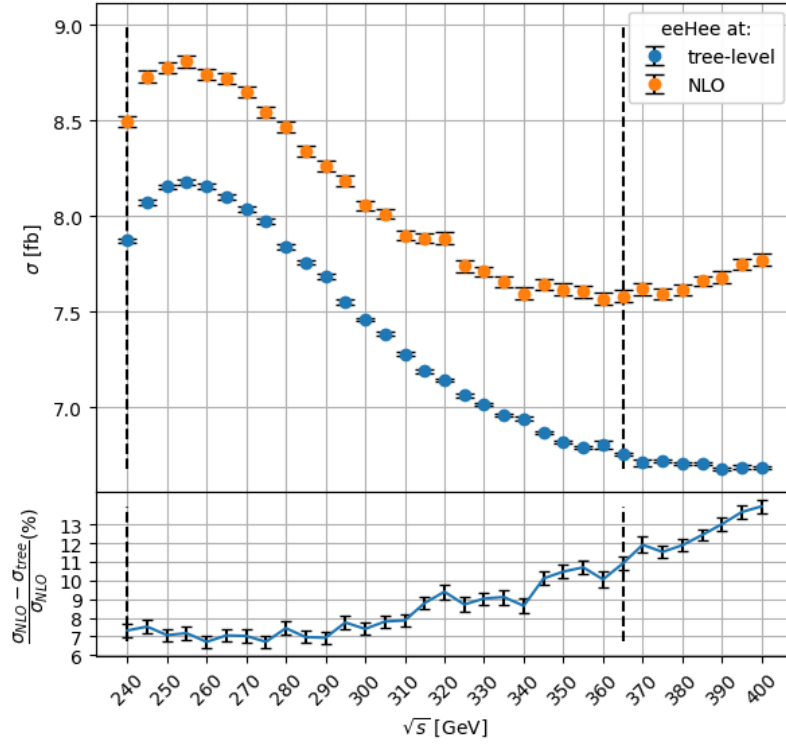
Figure 5.8: eeHee signal at tree-level and NLO and the quantum corrections from the lop diagrams as a function of the CM energy.

	eeHee	Higgsstrahlung	Z-fusion
	tree-level		
σ_{240GeV} [fb]	7.87(1)	7.43(1)	0.4936(5)
σ_{365GeV} [fb]	6.754(8)	3.801(5)	2.669(3)
	Loop		
σ_{240GeV} [fb]	$6.710(3)\times10^{-2}$	$6.702(6)\times10^{-2}$	$8.09(3)\times10^{-5}$
σ_{365GeV} [fb]	$3.964(6)\times10^{-2}$	$3.939(6)\times10^{-2}$	$3.27(1)\times10^{-4}$

Table 5.2: Cross-sections for Signal processes at tree-level and loop.

	eeHee NLO
σ_{240GeV} [fb]	8.50(3)
σ_{365GeV} [fb]	7.58(3)

Table 5.3: Cross-section for NLO process.

main production channel. For this work, using MadGraph5 we force the semileptonic decay on top quark, $t \rightarrow W^+ b$ where $W^+ \rightarrow e^+ \nu_e$, resulting in $e^+e^- b\bar{b}\nu_e\bar{\nu}_e$ in the final state, Figure 5.10.

(a)

(b)

(c)
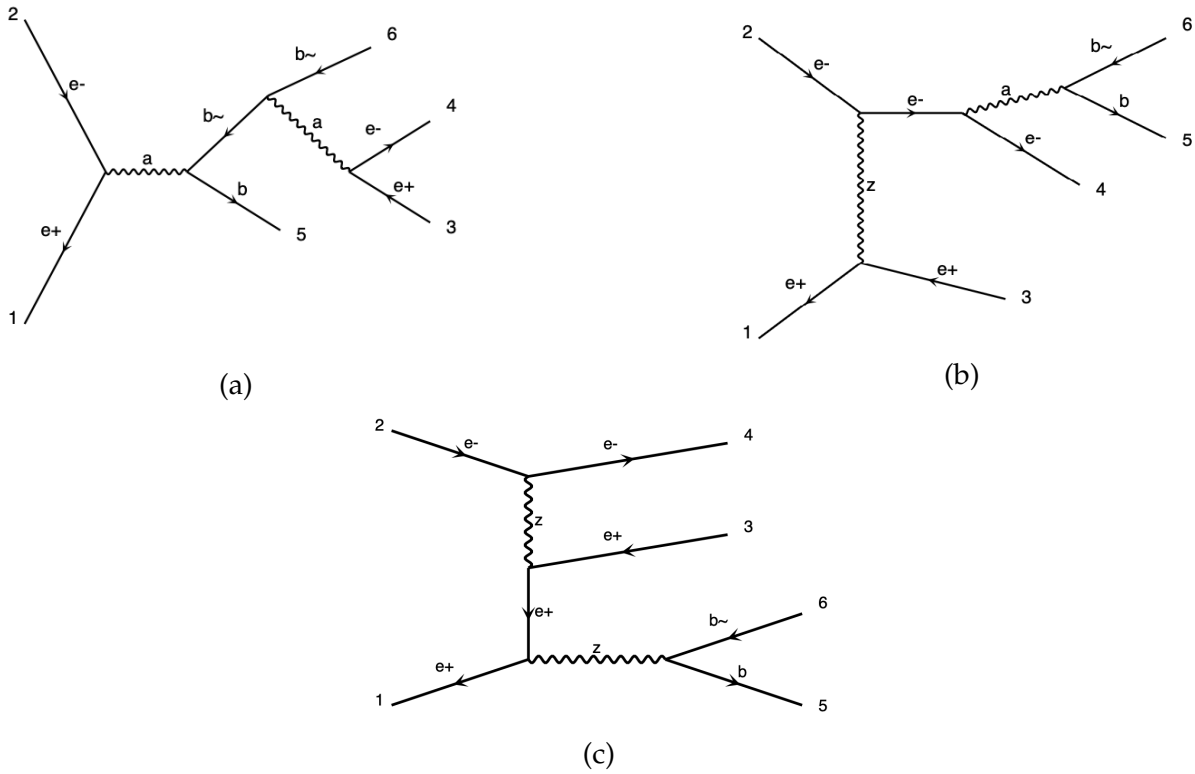
Figure 5.9: e+e-$b\bar{b}$ background.

(a)

(b)
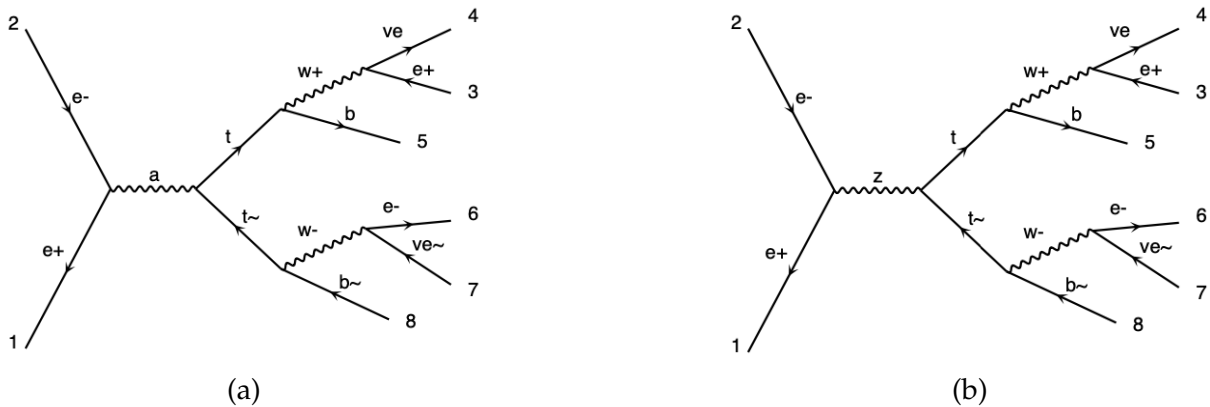
Figure 5.10: $t\bar{t}$ background.

The cross-sections for each background process are displayed in Table 5.4. At 240 GeV, the $t\bar{t}$ background has a negligible cross-section since the energy necessary to produce a top quark pair is at least 346 GeV.

	eebbee	$t\bar{t}$	$t\bar{t}$ w semileptonic decay
σ_{240GeV} [fb]	26.58(3)	X	X
σ_{365GeV} [fb]	22.83(3)	485.7(8)	3.380(4)

Table 5.4: Cross-sections for the background processes.

Chapter 6

Analysis

The analysis presented here uses the MC samples described in Chapter 5. The di-Higgs sample returned a cross-section so low that it is nearly impossible to detect in the middle of all the FCC-ee data. Only single-Higgs samples were considered in this analysis. Table 6.1 presents the samples used here for the signal and background and the nomenclature used.

Signal	
eeHee NLO	$e^+e^- \to e^+e^-h$, at NLO
eeZeeH	Higgsstrahlung
	Z-fusion
Background	
eebbee	$e^+e^- \to e^+e^-b\bar{b}$
eett	$e^+e^- \to t\bar{t} \to e^+e^-\nu_e\bar{\nu}_e b\bar{b}$
Background Global	Background Sum

Table 6.1: Signal and background samples

This work has as a target the Higgs boson factory at FCC-ee. We require additional information beyond the sample cross-sections to obtain accurate results. With the IDEA card, we can simulate the detector response. We will discuss this card and the changes we made to it in Section 6.1. The analysis of the IDEA response is explained in Sections 6.2 and 6.3 using the ROOT program from CERN [65].

6.1   Delphes: IDEA card

The IDEA card is a file in Delphes with the detector specifications from the layout to the efficiencies formulas and jet algorithms. This work used the default layout and efficiencies formulas while changing the jet algorithm and its parameters. The original jet algorithm in this card is the **Generalised k_t algorithm for e^+e^- collisions** discussed in Section 4.3.1 with 1.5, 1.0 GeV and -1 as the R, p_T^{min} and p parameters. This algorithm is identified as ee_genkt_Original for this work. While maintaining the algorithm, the first change made in this work was to change the previous parameters to 0.4 [82], 20 GeV, and -1.0, designated by ee_genkt. The last change was on the jet algorithm to

the anti-k_t algorithm while keeping the parameters from ee_genkt. A resume of the changes in the jet algorithm of the IDEA card is presented in Table 6.2.

Parameter	Original	Changed
Jet Algorithm	ee_genkt	anti-k_t/ee_genkt
Jet Radius	1. 5	0.4
PT min [GeV]	1.0	20.0
p parameter		-1.0

Table 6.2: Delphes IDEA parameters: Originals and Changed.

6.2 Pre-Selection

Following the Delphes simulation, the analysis was performed using the ROOT framework [65]. This Section presents the baseline analysis established on cuts on variables such as electrons and jets. Overlap Removal (OR) strategy used to avoid the double-counting and selection conditions in the particles p_T were evaluated.

An analysis based on cuts on kinematics variables is explained more forward. The examination at that level is based on the significance (S/$\sqrt{B}$) as a function of the cut region for a given variable.

6.2.1 ATLAS Overlap Removal

In experiments like ATLAS or CMS, the track efficiency, the resolution for leptons and charge hadron, the jet algorithm and its parameters, and many other components/parameters are optimized best to perform a high-quality reconstruction and analysis of the experiment. However, missing identifying and double-counting a particle object is always possible. For example, an electron object is identified as an electron and a jet, so in the final count, this electron is counted as an electron and a jet. In order to overcome this problem, the Overlap Removal procedure was created. This OR procedure compares two types of objects at a time and if there is geometric overlap, one is removed depending on a pre-defined priority.

Delphes simulation is no exception to this rule. In Figure6.1 to 6.2, it is possible to observe that the ΔR between two particles is lower than 0.5. This study considers that any particle with a ΔR lower than 0.4 is counted twice. An Overlap Removal based on the one used in Ref [82] was used to overcome this double count. It is defined as:

1. Any jet found within a ΔR of 0.2 of an electron is removed;

2. Any electron subsequently found within ΔR of of 0.4 of a jet is removed;

following this list of priorities. The Overlap Removal was implemented before selecting the desired electron, positron, and the two b-jets in the final state of our samples.

After the implementation of the Overlap Removal, in Figures 6.3 and 6.4, a cut for the particle p_T was applied. It is required for electrons to have a $p_T > 20$ GeV and

(a) 240 GeV

(b) 365 GeV
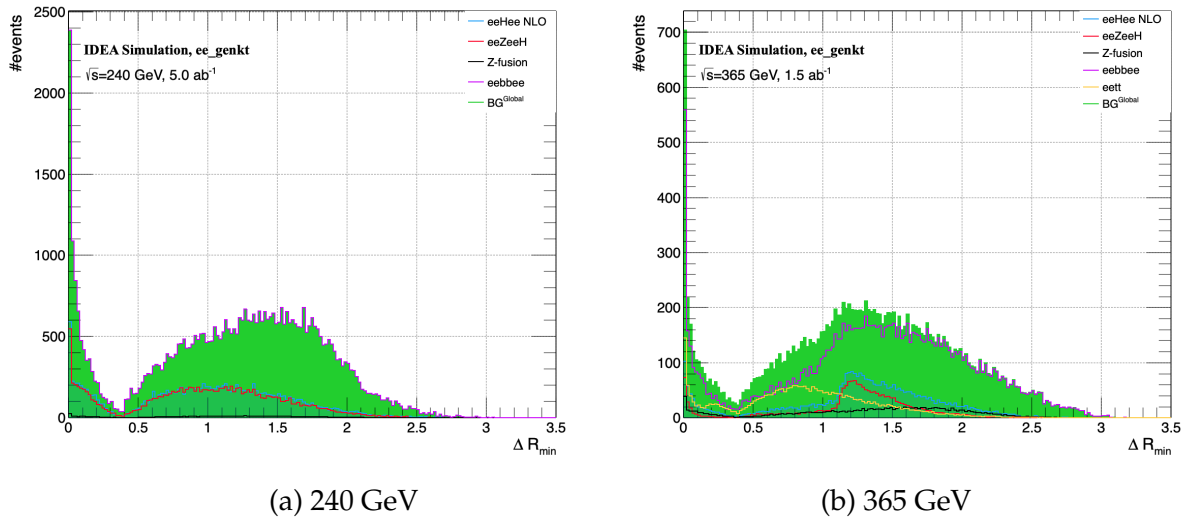
Figure 6.1: ΔR_{min}, before the OR, at both energies using the *ee_genkt* algorithm.

(a) 240 GeV

(b) 365 GeV
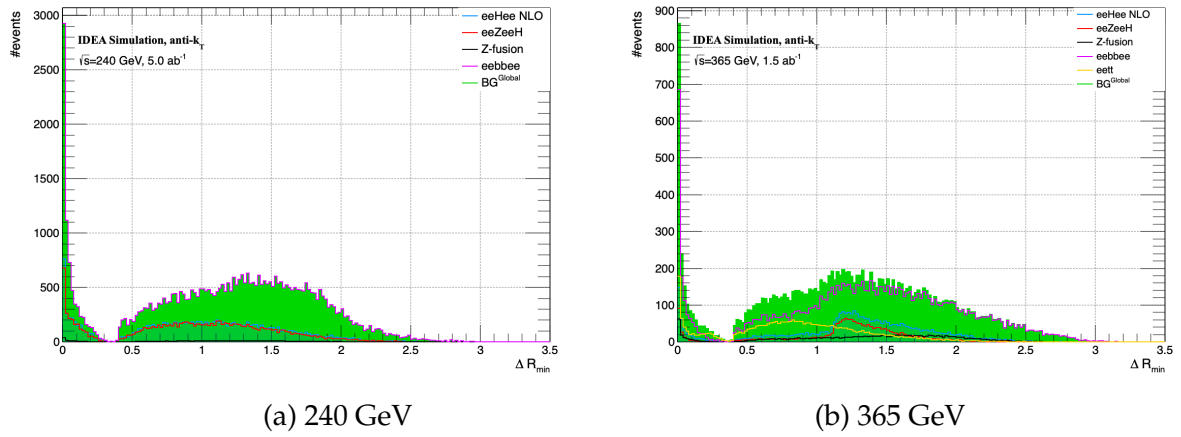
Figure 6.2: ΔR_{min}, before OR, at both energies using the *anti-k_T* algorithm.

(a) 240 GeV

(b) 365 GeV
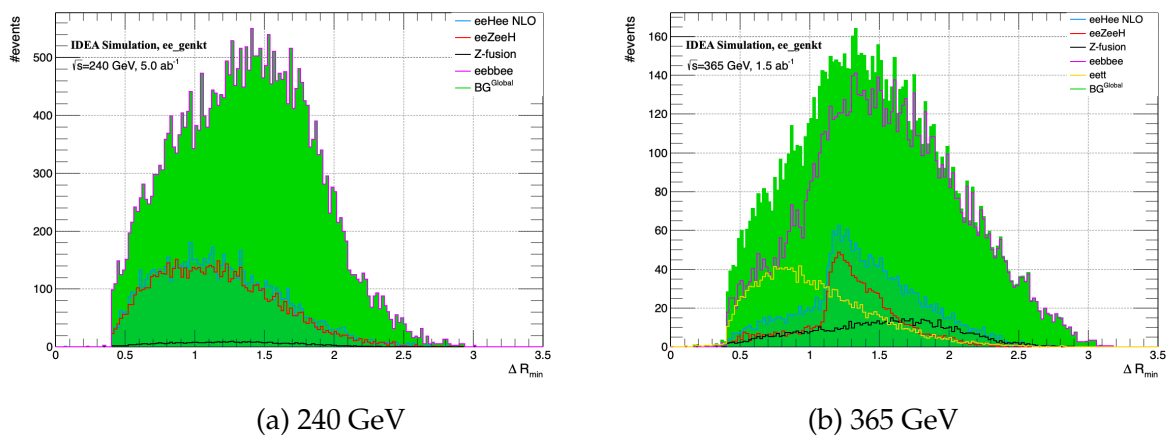
Figure 6.3: ΔR_{min}, after the OR, at both energies using the *ee_genkt* algorithm.

for all jets to have $p_T > 25$ GeV The effect of these cuts may be appreciated from the
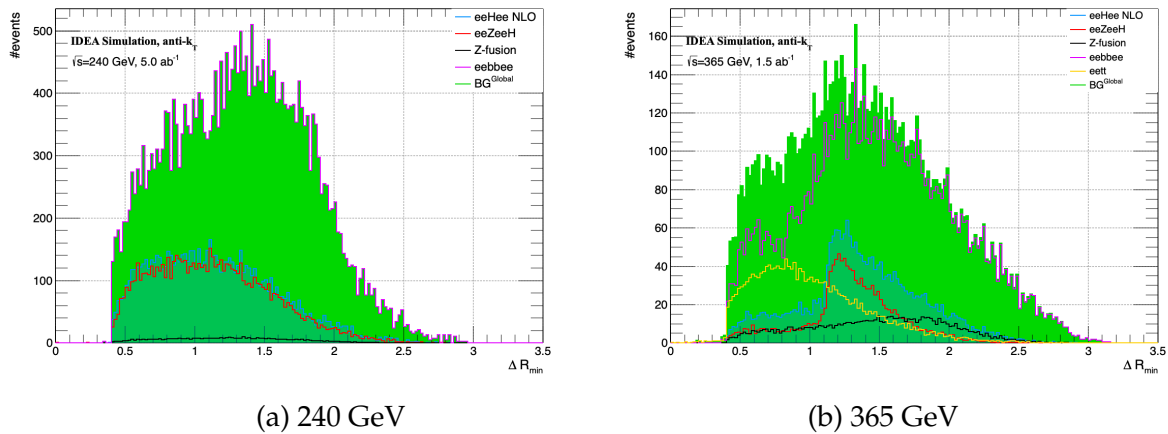
(a) 240 GeV

(b) 365 GeV

Figure 6.4: ΔR_{min}, after OR, at both energies using the *anti-k_T* algorithm.

(a)

(b)
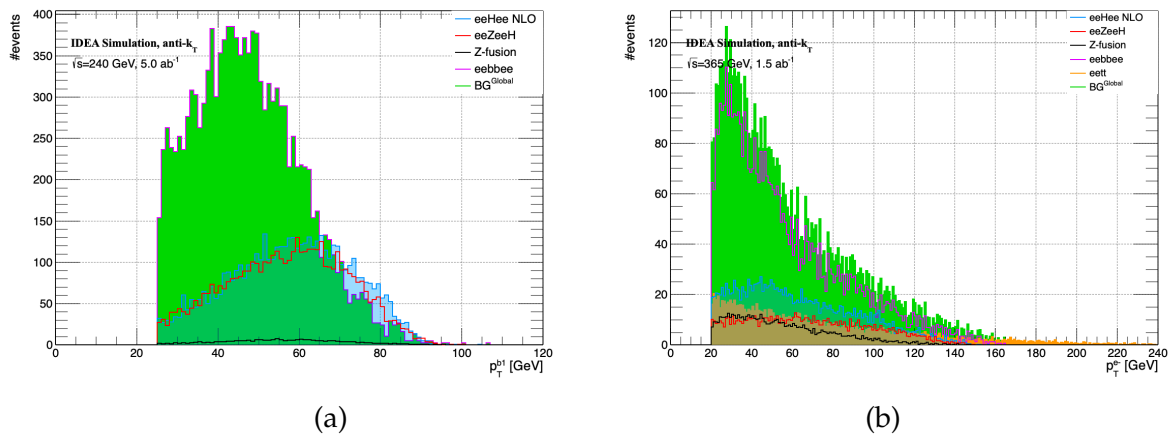
Figure 6.5: p_T distributions for (a) the leading b-jet at 240 GeV and (b) for the electron at 365 GeV. The histograms are normalized to the respective integrated luminosity.

distributions shown in Figures 6.5a and 6.5b.

The last step before the kinematics analysis was selecting the required reconstructed particles. For the leptons, a pair of electron-positrons with opposite charges, while for the jets, we required them to be identified by Delphes as a b-jet. The b-tag, c, and mistag probabilities in the IDEA card are presented in Table 6.3. Table 6.4 illustrates a resume of the pre-selection sorted according to their priority. The significance obtained after applying these selection cuts is presented in Table 6.5.

type	b-jet	c-jet	light mistag
probability	0.85	0.01	0.005

Table 6.3: B-tag, c, and light mistag probabilities.

Pre-selection	
ATLAS Overlap Removal	jet remove if $\Delta R_{jet,lepton}$<0.2
	lepton remove if $\Delta R_{lepton,jet}$<0.4
p$_T$	$p_T^{jets} > 25$ GeV
	$p_T^{lepton} > 20$ GeV
leptons	Single ee pair with charge 0
b-jets	single b-jet pair
$\mathbf{N}^{e^\pm(b-jets)}$	≥ 1 (2)

Table 6.4: Pre-selection.

$\sqrt{s}$ [GeV] \ Algorithm	anti-k_t	ee_genkt	ee_genkt_Original
240	45.48(67)	44.64(64)	17.67(47)
365	21.88(28)	21.48(27)	13.77(39)

Table 6.5: $S/\sqrt{B}$ obtained for 240 GeV and 365 GeV CM
energies from both jet algorithms after pre-selection.

6.3 Kinematic Analysis

The first optimization approach is based on applying successive cuts to the most relevant kinematic variables. The value of each cut is to optimize the significance after the cut. As for the baseline analysis, we start looking for variables capable of distinguishing the signal from the background. One of the advantages of working with a lepton collider is that the center of mass at the moment of collision is well-defined and is not described by a PDF. As it is in Ref [57, 83], we use the "recoil mass" method. This method works as follows:

1. In this simulation, we force the Z boson to decay into a pair of electron-positron. Although the Z dielectron branching ratio is low, this allows the eeHee events to be inclusive and efficiently selected independently of the Higgs boson decay mode;

2. From total energy-momentum conservation it is possible to retrieve the mass recoiling against the lepton pair:

$$m_{recoil}^2 = s + m_{ll}^2 - 2\sqrt{s}(E_{l^+} + E_{l^-}), \qquad (6.1)$$

where m_{ll} is the lepton pair invariant mass, and $E_{l^\pm}$ are the two lepton energies;

3. Towards a perfect determination of the lepton pair kinematics, and in the absence of initial state radiation, the m_{recoil} coincides precisely with the Higgs boson mass.

From the recoil mass, Figures 6.6a and 6.6c, it is possible to have an excellent way to distinguish the background from the signal. The main background is *eebb* at both
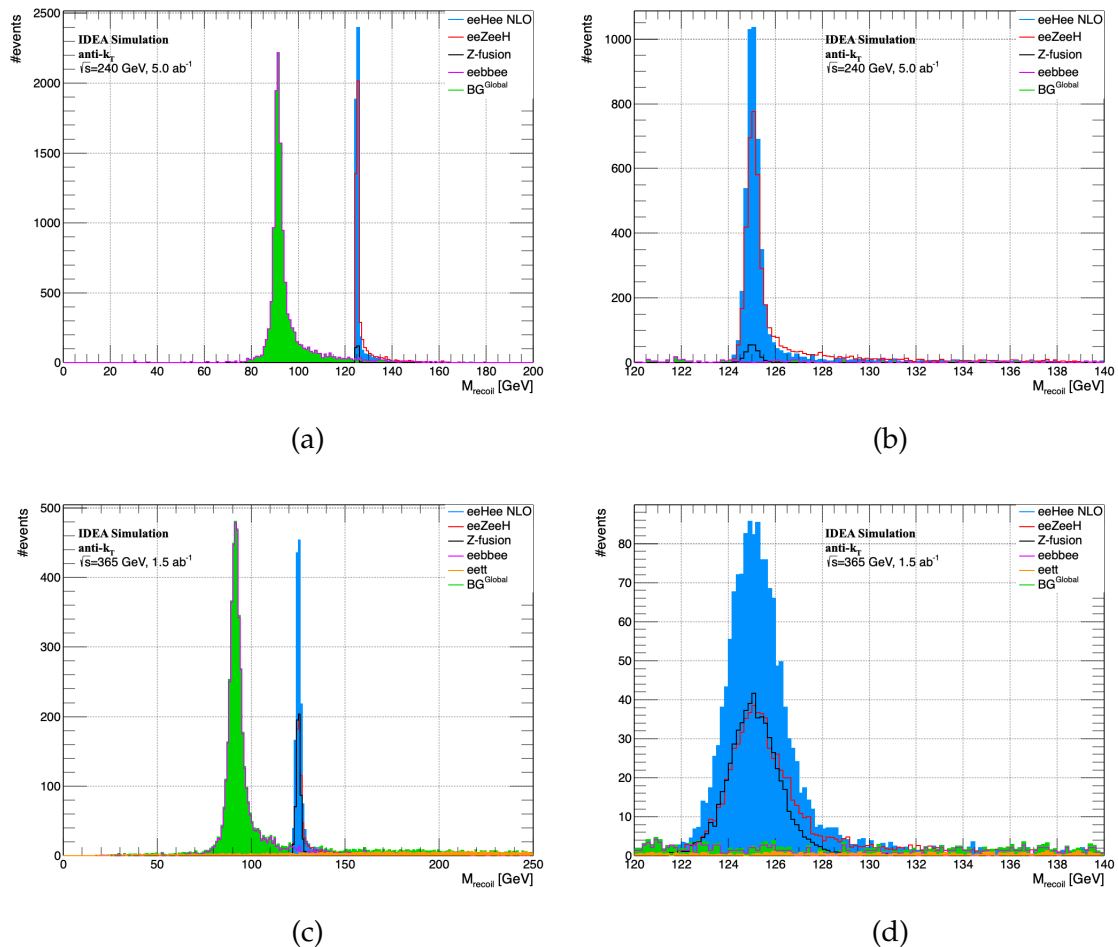
Figure 6.6: Inclusive m_{recoil} distribution for events with a Z decay into e^+e^-, displaying the Z peak from the eebb background and the H peak from the eeHee NLO, Higgsstrahlung, and Z-fusion samples at both energies. Expanded scale showing the m_{recoil} distribution in the region around m_H.

energies. This background was produced without any Higgs as a mediator particle, so the mass recoiling against the lepton pair is given by the Z boson mass. This kinematic variable is the best one to eliminate most of the *eebb* background. The *eett* background shows no peak, which makes sense since the electron-positron pair comes from different W bosons.

The selection of the cut in the m_{recoil} distribution was chosen to maximize the significance, $S/\sqrt{B}$[1]. As all samples with a Higgs boson peak centered at m_H in the m_{recoil} distribution, an $N\sigma$ window scan around the peak was calculated to get the significance. The peak and its sigma were extracted by fitting the eeHee NLO signal to a Bukin function, which is defined as

---
[1]The background present in the significance formula refers to the total background at that CM energy.

$$B_{Bukin}(x; \mathrm{n}, \mu, \sigma, \xi, \rho_L, \rho_R) = \begin{cases} n\mathrm{e}^{\frac{\xi\sqrt{\xi^2+1}(x-x_L)\sqrt{2\ln 2}}{\sigma\left(\sqrt{\xi^2+1}-\xi\right)^2\ln\left(\sqrt{\xi^2+1}+\xi\right)}+\rho_L\left(\frac{x-x_L}{\mu-x_L}\right)-\ln 2}, & x < x_L, \\[2em] n\mathrm{e}^{-\ln 2\left[\frac{\ln\left(1+2\xi\sqrt{\xi^2+1}\frac{x-\mu}{\sigma\sqrt{2\ln 2}}\right)}{\ln\left(1+2\xi^2-2|xi\sqrt{\xi^2+1}\right)}\right]^2}, & x_L \le x < x_R, \\[2em] n\mathrm{e}^{\frac{\xi\sqrt{\xi^2+1}(x-x_R)\sqrt{2\ln 2}}{\sigma\left(\sqrt{\xi^2+1}-\xi\right)^2\ln\left(\sqrt{\xi^2+1}+\xi\right)}+\rho_R\left(\frac{x-x_R}{\mu-x_R}\right)-\ln 2}, & x_R \le x, \end{cases} \tag{6.2}$$

where,

$$x_{L/R} = \mu + \sigma\sqrt{2\ln 2}\left(\frac{\xi}{\sqrt{\xi^2+1}} \mp 1\right), \tag{6.3}$$

and where μ and σ are the position and width of the peak, n is the amplitude, $\rho_{L/R}$ is the left/right tail exponential coefficients, and ξ parametrizes the asymmetry. All the parameters are floating variables and the mean, σ, and the ratio between χ^2 and the number of degrees of freedom (n.d.f) are presented in Table 6.6.
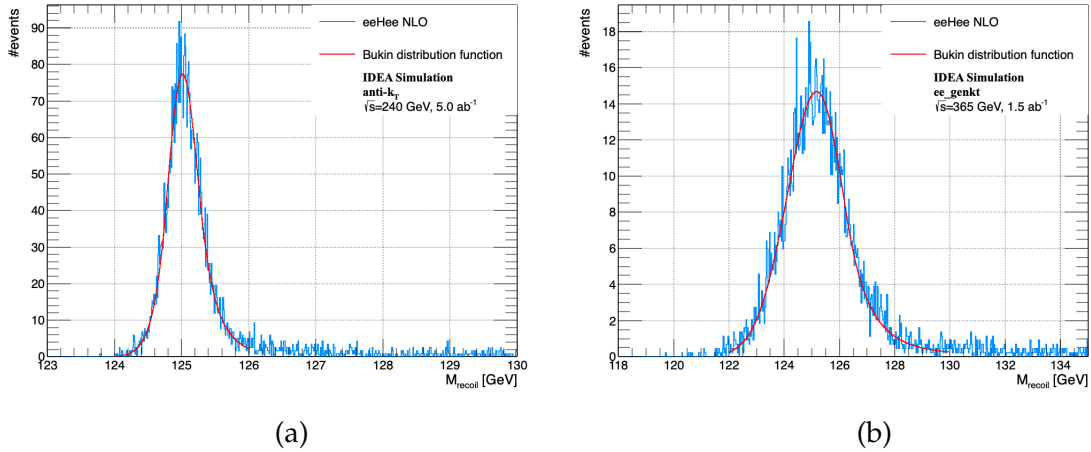
Figure 6.7: Recoil mass fit with Bukin distribution function (a) at 240 GeV with the anti-k_t and (b) at 365 GeV with the ee_genkt.

Algorithm	anti-k_t		ee_genkt	
$\sqrt{s}$ [GeV] Parameters	240	365	240	365
μ	125.015(9)	125.14(4)	125.024(7)	125.17(4)
σ	0.231(5)	1.052(22)	0.235(5)	1.02(2)
χ^2/n.d.f	0.975	0.924	0.95	0.927

Table 6.6: Peak, σ, and χ^2 divided by number of degrees of freedom (n.d.f) parameters from the m_{recoil} distribution using the anti-k_t and the ee_genkt algorithms.

(a) anti-k_t

(b) ee_genkt

(c) anti-k_t

(d) ee_genkt
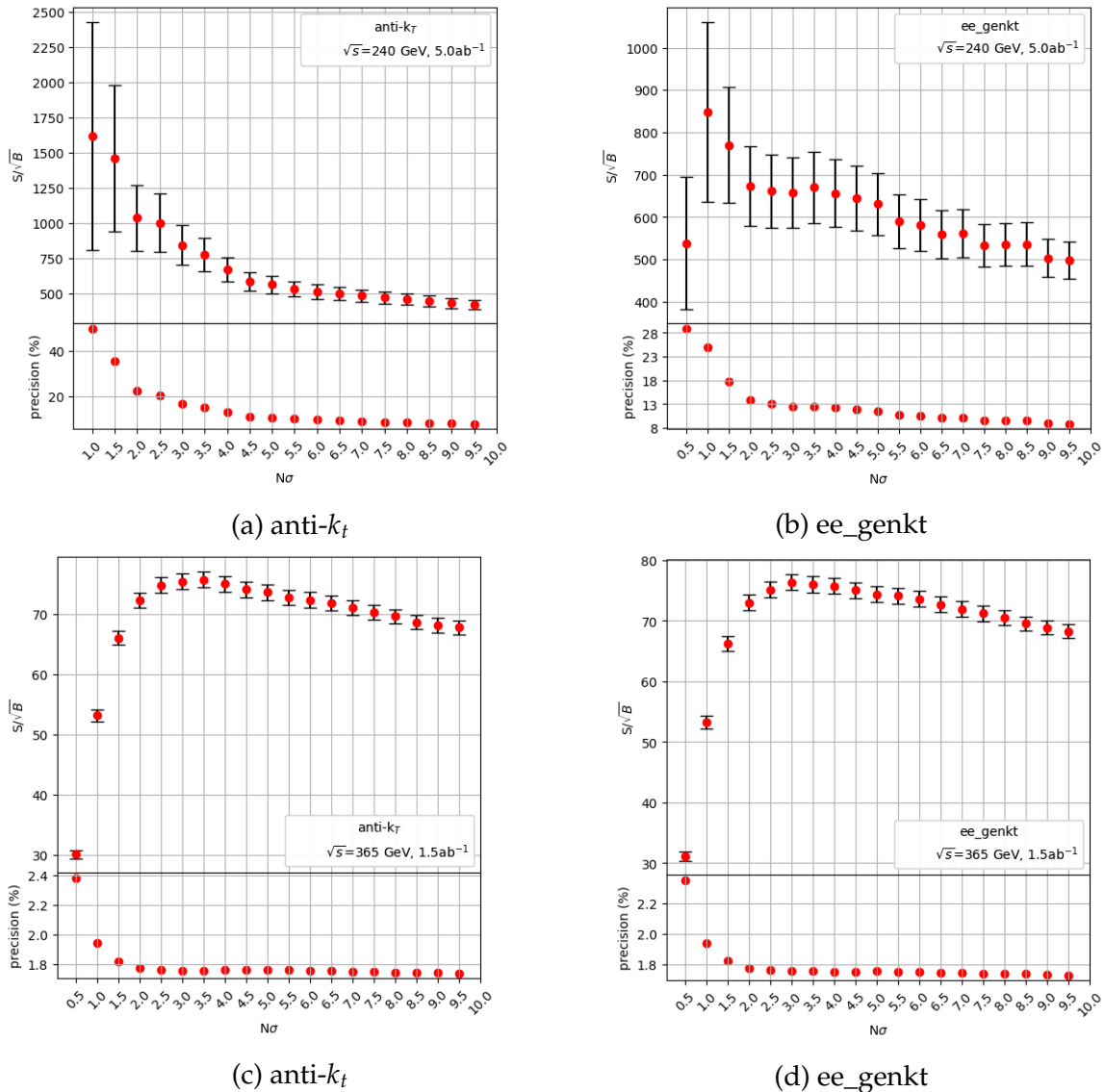
Figure 6.8: Signal significance as a function of the Nσ from the recoil mass fit at 240 GeV (a,b) and 365 GeV (c,d) for different jet algorithms.

For each value of σ, we obtained the expected number of signal and background events inside a window of Nσ, with N $\in$[0.5,9.5]. Using these numbers, we calculate the significance. The S/$\sqrt{B}$ as a function of the Nσ window is shown in Figure 6.8.

Based on these plots, we chose the 3σ window cut in both energies and algorithms.

After placing the cut on m_{recoil}, most background events are cut out, as seen from the electron-positron invariant mass plot in Figure 6.9. Although this cut isolates our signal from the background at 240 GeV, at 365 GeV we still have the background from the $t\bar{t}$ production. In this channel, electronic neutrinos are created from the top semileptonic decay. Since the neutrinos pass through the detector without detection, the missing transverse energy (MET) can be used to separate samples. The missing transverse energy is defined as:

$$E_T^{miss} = -\sum_i p_T^i, \tag{6.4}$$

where the index i runs over all visible particles.

(a)

(b)
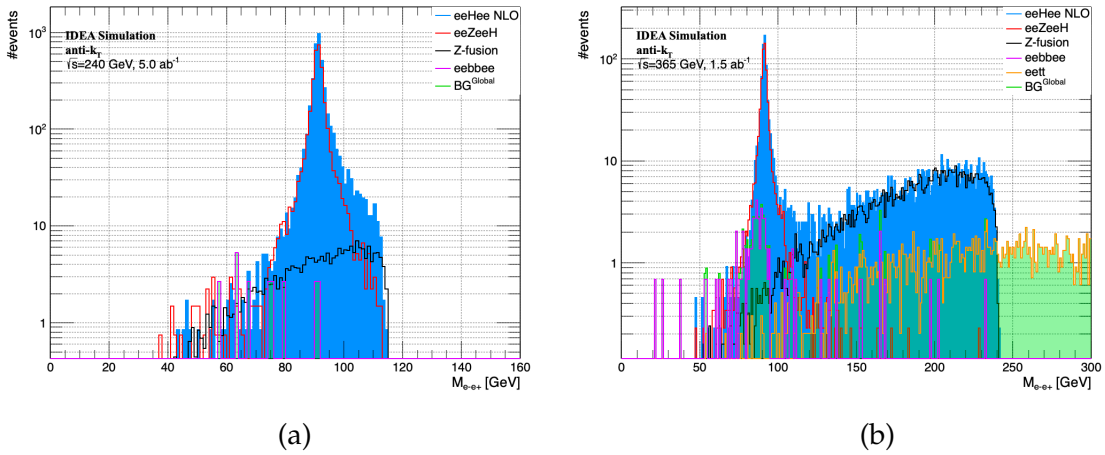
Figure 6.9: e^+e^- invariant mass after the m_{recoil} cut (a) at 240 GeV and (b) at 365 GeV.

(a)

(b)
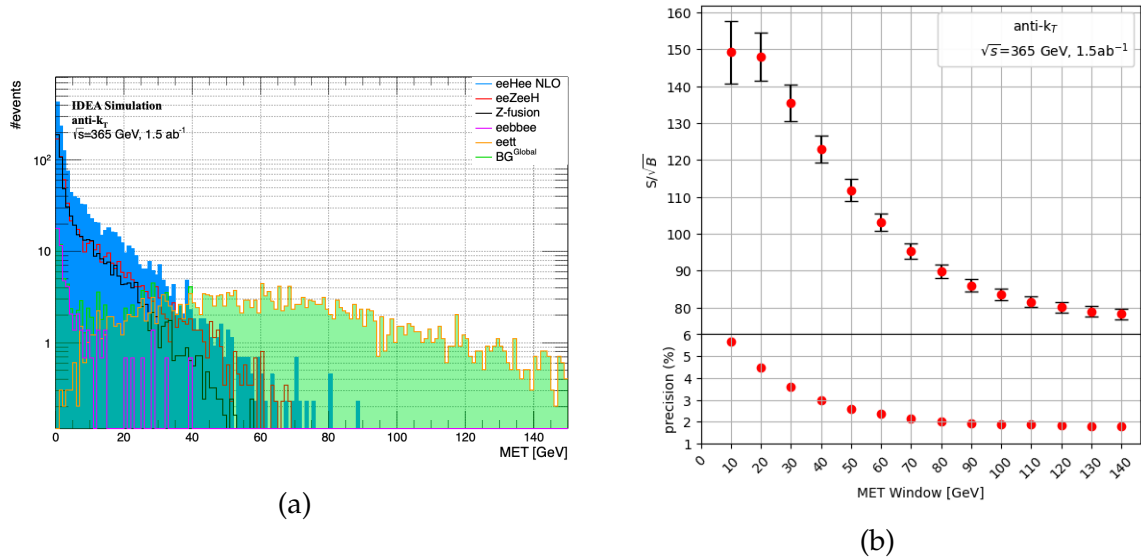
Figure 6.10: MET distribution after the m_{recoil} cut at 365 GeV
(left) and its significance as a function of MET's window (right).

The $t\bar{t}$ channel is the only one with neutrinos in the final state, so the MET total background at 365 GeV is expected to be higher than the signal, as shown in Figure 6.10a. Using the significance of the number of events from the MET distribution, we perform a scan by increasing the selection window from [0,10] to [0,140] GeV, and in parallel with the distribution plot, we choose the cut:

$$MET < 40\,GeV \tag{6.5}$$

At 240 GeV, since the background comes only from the eebb channel, the MET from all the channels will be low, as is possibly seen in Figure E.2. However, this cut was applied at both energies. Using the optimized analysis, we obtain the significance presented in Table 6.7 for each jet algorithm.

The percentage of improvement concerning the significance right after applying the pre-selection is in Table 6.8. The level of improvement was calculated using the

Algorithm $\sqrt{s}$ [GeV]	anti-k_t	ee_genkt	ee_genkt_Original
240	843.52±141.11	655.44±82.45	261.37±17.67
365	122.22±3.68	123.02±3.89	88.12±10.53

Table 6.7: $S/\sqrt{B}$ after the optimized analysis.

formula:

$$\left[\left((S/\sqrt{B})|_{opt} - (S/\sqrt{B})|_{pre} \right) / (S/\sqrt{B})|_{pre} \right] \times 100. \tag{6.6}$$

Algorithm $\sqrt{s}$ [GeV]	anti-k_t	ee_genkt	ee_genkt_Original
240	1754.54%	1368.33%	1379.06%
365	458.55%	472.80%	539.91%

Table 6.8: $S/\sqrt{B}$ improvement relative to its value after applying the pre-selection.

6.3.1 Higgsstrahlung and Z-fusion

The previous Section discussed selection cuts to avoid double-counting and the ones used to improve $S/\sqrt{B}$. Here are the cuts that can separate the Higgsstrahlung from the Z-fusion channel.

As it is possible to observe from the electron-positron invariant mass in Figures 6.9a and 6.9b, the Higgsstrahlung channel shows a peak around the Z boson mass. Instead of having that peak, the Z-fusion channel shows an asymmetric Gaussian-like distribution with a large left tail. Both of these distributions are not unexpected. In the first channel, the electron-positron pair is produced from the Z boson decay, Figure 5.5a, and the second is a scattering process, Figure 5.5b.

We count the number of events inside an invariant mass window to choose the best region to separate the channels. The window was increased in steps of 10 GeV. In Figures 6.11a and 6.11b, it is shown the significance between the s-channel and the t-channel, $S_{sch}/\sqrt{S_{tch}}$, versus the window max values.

As was discussed in Chapter 5, the Z-fusion channel becomes more dominant with the CM energy increase while, in the same sense, the Higgsstrahlung channel falls. This beginning of role change is shown clearly in Figures 6.12a and 6.12b. In parallel with the plots from Figure 6.11, we select the following regions:

$$\begin{cases} \text{if} \quad M_{e^+e^-}^{Inv} \in [80, 100] \text{ GeV}, & \text{Higgsstrahlung Region} \\ \\ \text{if} \quad M_{e^+e^-}^{Inv} > 100 \text{ GeV}, & \text{Z-fusion Region} \end{cases} \tag{6.7}$$

(a)

(b)
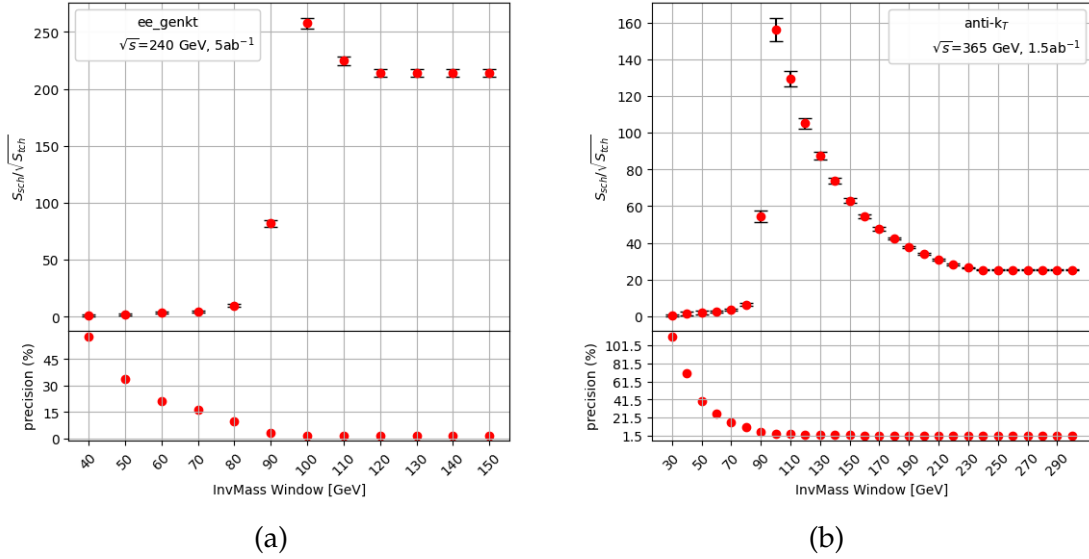
Figure 6.11: $S_{sch}/\sqrt{S_{tch}}$ as a function of the $M^{Inv}_{e^+e^-}$ window (a) at 240 GeV using the ee_genkt algorithm and (b) at 365 GeV using the anti-k_t algorithm.

(a)

(b)
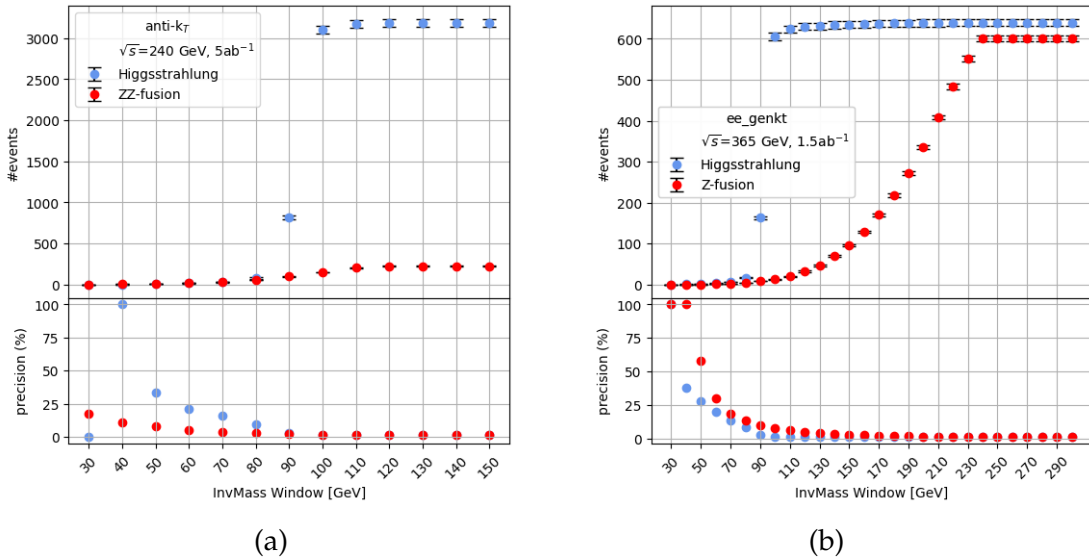
Figure 6.12: Number of events as a function of the $M^{Inv}_{e^+e^-}$ window (a) at 240 GeV using the anti-k_t algorithm and (b) at 365 GeV using the ee_genkt algorithm.

6.3.2 Statistical uncertainties

In detector experiments, the background has a much larger cross-section than the signal, meaning that the number of background events for a given integrated luminosity will be greater than the number of events for the signal. Although the cross-sections from MG5 agree with the first fact when passing through a detector simulator, the second fact shows up to disagree with the reality. To see this last point, Figure 6.13, the electron-positron invariant mass, is presented.

Like in actual experiments, these histograms are filled with weight 1. However, the number of events from eeHee NLO, Higgsstrahlung, and Z-fusion samples indicate higher than the background samples. In order to represent the data from detector experiments, we need to simulate the proper amount of events expected to have in
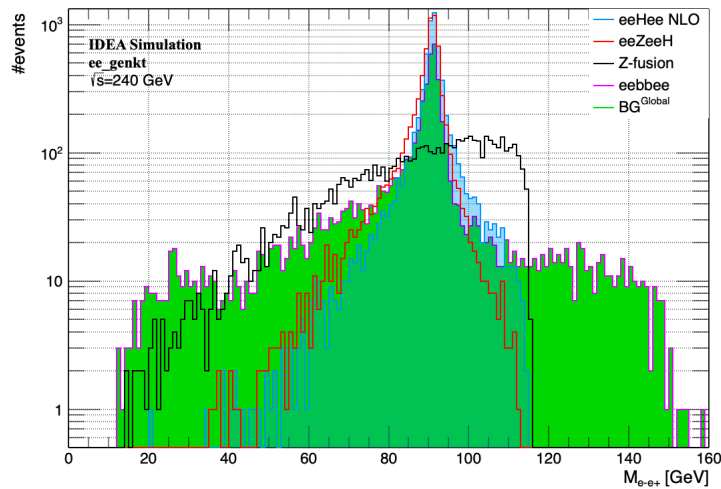
Figure 6.13: $M^{Inv}_{e^+e^-}$ after the selection condition and without any normalization

the FCC-ee, which is, at least, 10^6 HZ for an integrated luminosity of 5 ab^{-1}. Unfortunately, neither the MG5 can simulate this amount of events, of which the maximum value is 1 million events, nor do we have the computational power to generate them. Therefore, we apply different weights, w, according to the number of events from the MC simulation and to the cross-section for each sample. The weight is defined as

$$w = \frac{L_{FCC-ee} \times \sigma_{MG5}}{N_{MG5}}, \tag{6.8}$$

where L_{FCC-ee} is the integrated luminosity expected to have in the FCC-ee, N_{MG5} and σ_{MG5} are the number of events and cross-section, respectively, generated from Mad-Graph5.

Assuming that the number of events generated follows a Poisson distribution, the uncertainty is given by $\sqrt{N}$ where N is the number of events. To be capable of normalizing the number of events to a given luminosity, we multiplied the number of events and the uncertainty by the weight: $N_{Norm} \pm \Delta N_{Norm} = w \times (N_{MG5} \pm \Delta N_{MG5})$. The weighted number of events and their uncertainty can be used in standard error propagation to compute the statistical uncertainty associated with any expression, particularly with $S/\sqrt{B}$. The statistical error associated with the significance is given by:

$$\Delta \left(\frac{S}{\sqrt{B}} \right) = \sqrt{\left(\frac{\Delta S}{\sqrt{B}} \right)^2 + \left(-\frac{S \cdot \Delta B}{B^{3/2}} \cdot \frac{1}{2} \right)^2}, \tag{6.9}$$

where ΔS and ΔB are the uncertainties associated with the number of signal and total background events.

Chapter 7

Results

Chapter 6 discusses the pre-selection and kinematic analysis used at 240 and 365 GeV. In this chapter, we describe and compare the results of the signal optimization at FCC-ee for the different jet algorithms used on the detector response.

7.1 Single-Higgs Results

The results from the event selection of the single Higgs production at the FCC-ee with an integrated luminosity of 5.0 ab^{-1} are summarized in Tables 7.1to 7.3, and at 1.5 ab^{-1} are in Tables 7.4to 7.6 for the ee_genkt_Original, ee_genkt and anti-k_t algorithms. The double line in each table marks the reconstructed, the pre-selection, and the optimized level.

Selection	eeHee$_{NLO}$	Higgsstrahlung	Z-fusion	Background
Reconstruct	100%	100%	100%	100%
	42456(190)	37146(176)	2468(11)	132820(594)
ATLAS OR	96.800%	96.888%	97.553%	97.242%
p$_T^{jets(lept)}$ >25 (20) GeV	88.227%	89.136%	84.650%	77.844%
Q(e$^\pm$)=$\pm$1, b-tag	18.709%	20.299%	16.658%	25.701%
N$_{e^\pm}\geq 1$, N$_{b-jet}\geq 2$	3.348%	3.752%	3.400%	4.871%
	1421(35)	1394(34)	84(2)	6470(131)
$m_{Recoil}\in 3\,\sigma$ Window	2.662%	2.488%	2.856%	0.014%
MET < 40 GeV	2.656%	2.484%	2.850%	0.014%
	1127(31)	923(30)	70(2)	19(7)
$m_{e^+e^-}^{Inv}\in$[80,100] GeV	2.475%	2.338%	1.052%	0.000%
$m_{e^+e^-}^{Inv}$ > 100 GeV	0.102%	0.030%	0.508%	0.000%

Table 7.1: Cumulative efficiency, in percentage, of each event selection criterion of eeHee$_{NLO}$, Higgsstrahlung, Z-fusion, and Background. The absolute value of expected events is normalized to $\mathcal{L}$ = 5.0 ab^{-1}. These results were obtained using the IDEA detector design with the ee_genkt_Original algorithm.

Selection	eeHee$_{NLO}$	Higgsstrahlung	Z-fusion	Background
Reconstruct	100%	100%	100%	100%
	42420(190)	37138(166)	2464(11)	131638(592)
ATLAS OR	91.7%	91.1%	91.3%	84.6%
p$_T^{jets(lept)}$ >25 (20) GeV	85.1%	85.0%	82.8%	73.0%
Q(e$^\pm$)=$\pm$1, b-tag	32.3%	34.0%	27.5%	40.6%
N$_{e^\pm} \geq 1$, N$_{b-jet} \geq 2$	12.58%	12.92%	10.77%	10.85%
	5335(67)	4800(60)	265(4)	14287(195)
$m_{Recoil} \in 3\,\sigma$ Window	10.11%	8.87%	9.57%	0.03%
MET < 40 GeV	10.08%	8.84%	9.55%	0.03%
	4274(60)	3283(49)	235(3)	43(11)
$m_{e^+e^-}^{Inv} \in$[80,100] GeV	9.28%	8.45%	3.75%	0.012%
$m_{e^+e^-}^{Inv} \geq$100 GeV	0.64%	0.18%	3.22%	0.002%

Table 7.2: Cumulative efficiency, in percentage, of each event selection criterion of eeHee$_{NLO}$, Higgsstrahlung, Z-fusion, and Background. The absolute value of expected events is normalized to $\mathcal{L}$ = 5.0 ab^{-1}. These results were obtained using the IDEA detector design with the ee_genkt algorithm changed.

Selection	eeHee$_{NLO}$	Higgsstrahlung	Z-fusion	Background
Reconstruct	100%	100%	100%	100%
	42387(190)	37138(166)	2462(11)	131115(590)
ATLAS OR	90.33%	89.56%	89.44%	81.26%
p$_T^{jets(lept)}$ >25 (20) GeV	83.47%	82.90%	80.75%	70.07%
Q(e$^\pm$)=$\pm$1, b-tag	32.17%	33.74%	27.38%	39.20%
N$_{e^\pm} \geq 1$, N$_{b-jet} \geq 2$	12.15%	12.55%	10.24%	9.79%
	5152(66)	4659(59)	252(6)	12830(185)
$m_{Recoil} \in 3\,\sigma$ Window	9.76%	8.59%	9.13%	0.02%
MET < 40 GeV	9.73%	8.57%	9.11%	0.02%
	4126(59)	3182(49)	224(3)	24(8)
$m_{e^+e^-}^{Inv} \in$[80,100] GeV	8.94%	8.16%	3.55%	0.0041%
$m_{e^+e^-}^{Inv} >$ 100 GeV	0.62%	0.20%	3.18%	0.00%

Table 7.3: Cumulative efficiency, in percentage, of each event selection criterion of eeHee$_{NLO}$, Higgsstrahlung, Z-fusion, and Background. The absolute value of expected events is normalized to $\mathcal{L}$ = 5.0 ab^{-1}. These results were obtained using the IDEA detector design with the anti-k_t algorithm.

Considering the Higgs production in FCC-ee at 240 GeV and 365 GeV after applying the kinematics cuts, Table 6.7, the significance, independently of the jet algorithm

Selection	eeHee$_{NLO}$	Higgsstrahlung	Z-fusion	Background
Reconstruct	100%	100%	100%	100%
	11421(51)	5700(45	4003(18)	39305(155)
ATLAS OR	97.61%	99.11%	96.88%	97.17%
p$_T^{jets(lept)}$ >25 (20) GeV	91.19%	95.17%	90.77%	83.62%
Q(e$^\pm$)=$\pm$1, b-tag	16.35%	18.03%	17.38%	20.33%
N$_{e^\pm} \geq 1$, N$_{b-jet} \geq 2$	2.98%	3.49%	2.30%	1.55%
	340(9)	199(8)	92(3)	611(13)
$m_{Recoil} \in 3\,\sigma$ Window	2.28%	2.30%	2.12%	0.05%
MET < 40 GeV	2.21%	2.22%	2.03%	0.02%
	124(8)	133(7)	81(3)	8(2)
$m_{e^+e^-}^{Inv} \in$[80,100] GeV	1.23%	2.02%	0.05%	0.01%
$m_{e^+e^-}^{Inv}$ > 100 GeV	0.98%	0.17%	1.96%	0.01%

Table 7.4: Cumulative efficiency, in percentage, of each event selection criterion of eeHee$_{NLO}$, Higgsstrahlung, Z-fusion, and Background. The absolute value of expected events is normalized to $\mathcal{L} = 1.5$ ab^{-1}. These results were obtained using the IDEA detector design with the ee_genkt_Original algorithm.

Selection	eeHee$_{NLO}$	Higgsstrahlung	Z-fusion	Background
Reconstruct	100%	100%	100%	100%
	11412(51)	5701(25)	4004(18)	39293(155)
ATLAS OR	93.57%	93.62%	92.28%	88.18%
p$_T^{jets(lept)}$ >25 (20) GeV	89.98%	91.33%	88.69%	82.21%
Q(e$^\pm$)=$\pm$1, b-tag	37.20%	41.66%	40.24%	54.16%
N$_{e^\pm} \geq 1$, N$_{b-jet} \geq 2$	15.12%	16.51%	15.89%	16.43%
	1726(20)	941(10)	636(7)	6457(61)
$m_{Recoil} \in 3\,\sigma$ Window	12.48%	11.56%	15.14%	0.89%
MET < 40 GeV	12.24%	11.24%	15.02%	0.33%
	1397(18)	6341(9)	601(7)	129(7)
$m_{e^+e^-}^{Inv} \in$[80.100] GeV	5.72%	10.36%	0.22%	0.09%
$m_{e^+e^-}^{Inv}$ > 100 GeV	6.42%	0.59%	14.69%	0.20%

Table 7.5: Cumulative efficiency, in percentage, of each event selection criterion of eeHee$_{NLO}$, Higgsstrahlung, Z-fusion, and Background. The absolute value of expected events is normalized to $\mathcal{L} = 1.5$ ab^{-1}. These results were obtained using the IDEA detector design with the ee_genkt algorithm changed.

used, is above 5σ. This result indicates that the Higgs boson accumulated from the process $e^+e^- \rightarrow e^+e^-h$ is expected to be accumulated by the IDEA detector will be

Selection	eeHee$_{NLO}$	Higgsstrahlung	Z-fusion	Background
Reconstruct	100%	100%	100%	100%
	11416(51)	5701(25)	4003(18)	39287(155)
ATLAS OR	92.83%	93.11%	90.96%	84.65%
p$_T^{jets(lept)}$ >25 (20) GeV	89.03%	90.77%	86.88%	78.47%
Q(e$^\pm$)=$\pm$1, b-tag	37.35%	41.34%	40.94%	52.91%
N$_{e\pm} \geq 1$, N$_{b-jet} \geq 2$	14.62%	15.90%	15.64%	14.79%
	1668(20)	906(10)	626(7)	5811(57)
$m_{Recoil} \in 3\,\sigma$ Window	12.14%	11.22%	14.99%	0.87%
MET < 40 GeV	11.90%	10.88%	14.86%	0.32%
	1358(18)	620(8)	595(7)	123(7)
$m_{e^+e^-}^{Inv} \in [80,100]$ GeV	5.33%	10.04%	0.22%	0.08%
$m_{e^+e^-}^{Inv} > 100$ GeV	6.27%	0.58%	14.51%	0.20%

Table 7.6: Cumulative efficiency, in percentage, of each event selection criterion of eeHee$_{NLO}$, Higgsstrahlung, Z-fusion, and Background. The absolute value of expected events is normalized to $\mathcal{L} = 1.5$ ab^{-1}. These results were obtained using the IDEA detector design with the anti-k_t algorithm.

highly visible and distinguish from the background. This outcome should not be a surprise. Section 3.3 presents four points that one needs to consider about the type of collider to be built. In the second point, we stated that the signal-background ratio would not be a problem using a Lepton collider, meaning a clean environment. This clean environment can be observed from our significance even after the pre-selection.

Taking advantage of the elemental particles' properties from the beam and with the high-precision center of mass energy calibration, the recoil mass can be measured with extreme precision, which is our main step to reaching our goal. With the m_{recoil}, we can take almost 100% of our background, especially at $\sqrt{s}$=240 GeV. At $\sqrt{s}$=365 GeV $\sim$99% of our background is removed but can be reduced even more. Adding a cut in the missing transverse energy reduces the background to $\sim$0.03% for the anti-k_t and ee_genkt and $\sim$0.025% for the ee_genkt_Original.

7.1.1 Significance

In this work, we use three different jet algorithms: the one that already comes in the IDEA detector card where no parameters were changed (ee_genkt_Original), the same algorithm but with the parameters from the Ref[82] (ee_genkt), and the anti-k_t with the same parameters that this last one. All of them had delivered a high significance after the kinematics cuts. Table 7.7 presents the improvement, in percentage, caused by changing parameters in the ee_genkt algorithm, using Eq.(7.1).

$$\left[\left((S/\sqrt{B})|_{ee\_genkt} - (S/\sqrt{B})|_{ee\_genkt\_Original} \right) / (S/\sqrt{B})|_{ee\_genkt\_Original} \right] \times 100 \quad (7.1)$$

From Table 7.7, we observe that when considering the jet radius 0.4 instead of the

$\sqrt{s}$ [GeV] Algorithm	240	365
ee_genkt	150.77%	39.61%

Table 7.7: S/$\sqrt{B}$ improvement from the parameters change in ee_genkt algorithm.

original 1.5 with an increase of the jets' p_T^{min} from 1 to 20 GeV, the significance is improved, especially at 240 GeV. When considering a radius jet of 1.5, the reconstructed jet can have other particles that are not supposed to be classified as jets. The effect of the jet radius decrease is visible when jets with a BTag of 1 or 3 and leptons with opposite charges are selected. However, such variation vanishes when we compare the significance from ee_genkt with the anti-k_t algorithm.

$\sqrt{s}$ [GeV] Algorithm	240	365
anti-k_t	28.70%	-0.66%

Table 7.8: S/$\sqrt{B}$ improvement from the algorithm change from ee_genkt to anti-k_t.

$$\left[\left((S/\sqrt{B})|_{anti\text{-}k_T} - (S/\sqrt{B})|_{ee\_genkt} \right) / (S/\sqrt{B})|_{ee\_genkt} \right] \times 100 \qquad (7.2)$$

When we compare the ee_genkt with the anti-k_t algorithm, Table 7.8, the variation between significances shows no drastic variation like in Table 7.7. Therefore, using the anti-k_t algorithm for a detector like the IDEA simulation from Delphes, we expect an improvement of $\sim$29% at 240 GeV. At 365 GeV, the anti-k_t shows a significance of $\sim$0.23% lower than the one from the ee_genkt algorithm but nothing too extreme that does not allow us to use that algorithm.

7.1.2   eeHee: NLO and Loop

As can be observed in Table Table 7.9, the number of events from loop diagrams and their interference with the tree-level processes will be overshadowed by the number of events from the total signal process. The quantum contributions from loop processes correspond to the amounts of 3.6% and 4.24% at 5.0 and 1.5 ab^{-1} corresponding to a 2.3σ and 1.6σ for the standard deviation, respectively. Although the FCC-ee needs to reach an integrated luminosity of 23.4 and 15.4 ab^{-1} at 240 and 365 GeV of CM energy, it is possible to observe the effects of this quantum correction at some observables such as the M$_{b-jets}$ and E$_{b-jets}$, where, for their highest values it is possible to see some deviation when compare the signal at tree-level and at NLO Figures 7.1 and 7.2.

$\sqrt{s}$ [GeV]	240 (5.0 ab^{-1})	365 (1.5 ab^{-1})
Total signal events	4126	1358
Loop + interference events	149	58
Contributions from quantum effects (%)	3.6	4.24
Standard deviations	2.3	1.6
$L_{5\sigma}$ [ab^{-1}]	23.4	15.4

Table 7.9: Total signal and loop+interference events, quantum contributions, and standard deviations according to the integrated luminosities at the FCC-ee [39].
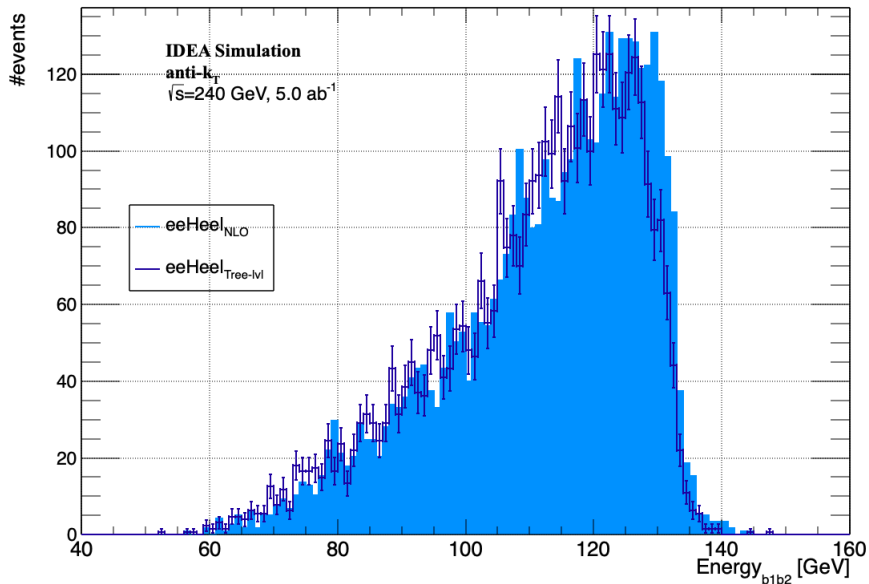
Figure 7.1: Energy of a pair of b-jets.
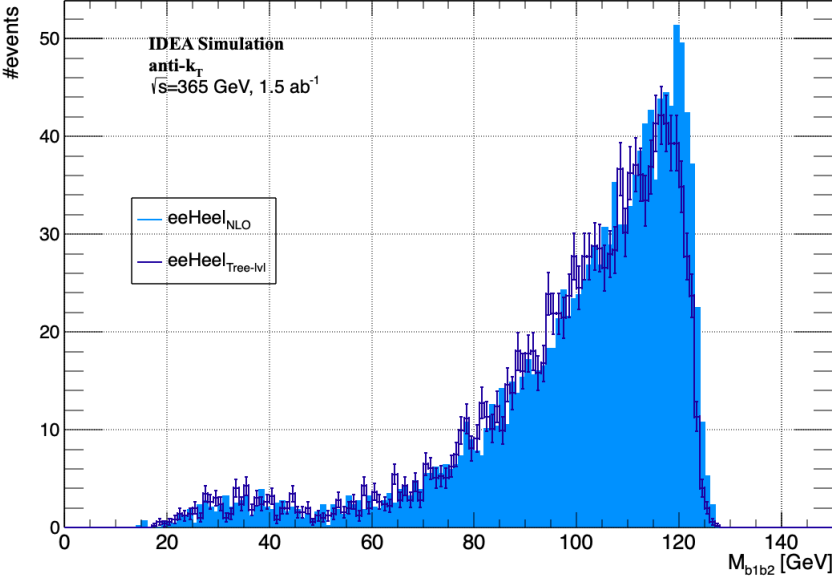
Figure 7.2: Mass of a pair of b-jets.

Chapter 8

Conclusion

This thesis presented a study targeting the FCC-ee sensitivity to the Higgs self-coupling constant. The analysis focused the FCC-ee phases where the Higgs boson will be studied, which corresponds to the periods with center of mass energies at 240 and 365 GeV with integrated luminosities of 5.0 and 1.5 ab^{-1}, respectively.

The first approach presented in this work was a direct measurement of the Higgs self-coupling through the di-Higgs production with both Higgs bosons decaying to b quarks, $e^+ e^- \to e^+ e^- h h, h \to b \bar{b}$. However, we have determined that the cross-section for this channels is too low, $4.523(15) \times 10^{-4}$ fb, leading to less that one event to be produced for the entire operation of the FCC-ee accelerator. After the previous finding, we have dedicated the rest of the work to an alternative analysis, focusing on $e^+ e^- \to e^+ e^- h$, single Higgs production, with the Higgs decaying to b quarks. The idea behind this analysis is to estimate if the effect from the triple Higgs coupling (λ_{hhh}) present in higher order diagrams would be enough to gain experimental sensitivity to this coupling. This follows an idea first proposed by F. Maltoni et al. [84].

Through MadGraph5, we simulate the samples for the Higgsstrahlung and Z-fusion processes individually and the samples considered as the signal was the combination of them with their interferences included. For the background, all the processes with $e^+ e^- b\bar{b}$ without any Higgs boson as a mediator and top pair production with a top decaying in a semileptonic way. The samples were hadronized with the Pythia8 simulated and the IDEA detector response through Delphes.

The next step was removing all the double-counting objects. For this, the overlap removal used in ATLAS experiment. After the overlap removal, at least two electrons with opposite charges from the Z decay and a pair of b-quarks produced by the Higgs decay were requested. From the optimized analysis, we found that the recoil mass system against the electron-positron pair was one of the best kinematic variables to be used to separate the signal from the background. Using the Bukin function for the fit, we retrieved the peak and the sigma values used for the recoil mass scan where the 3σ window was chosen to be the most suitable region. Taking into account the background at $\sqrt{s}$= 365 GeV, where the final state had neutrinos, the missing transverse energy variables need to be used and the region that improves the signal significance is between [0,40[GeV. Using the electron-positron invariant mass, it is possible to separate the contributions of the two production channels which allows us to study each process individually.

This analysis consisted of using two different jet algorithms: the Generalised k_T algorithm for $e^+ e^-$ collision and the anti-k_t algorithm. For the first algorithm, we use

61

two different sets of parameters: one where we did not change the IDEA card's original parameters, a jet radius of 1.5, and a transverse momentum minimum of 1 GeV for the jets, while for the second set, we chose 0.4 and 20 GeV for the jet radius and transverse momentum minimum. This last set of parameters was also used in the anti-k_t algorithm.

Some observables, such as E_{b1b2} and M_{b1b2}, show to have sensibility to the quantum effects from the loop diagrams at their highest values. We estimate that the measurement can be made at 2.3σ and 1.6σ at CM energies of 240 and 365 GeV, respectively.

As future work, performing a deeper study for observables sensible to the quantum effects by deviations of the Higgs self-coupling constant. This study can be carried out through more advanced techniques such as machine learning and with the use of other generators that allows to change the value of λ_{hhh} at NLO, in order to cross check the effects of new physics in this coupling.

Bibliography

[1] P. W. Higgs, "Spontaneous symmetry breakdown without massless bosons," *Physical review*, vol. 145, no. 4, p. 1156, 1966.

[2] C. Collaboration, "Observation of a new boson at a mass of 125 gev with the cms experiment at the lhc," *Physics Letters B*, vol. 716, no. 1, pp. 30–61, 2012, ISSN: 0370-2693. DOI: `https://doi.org/10.1016/j.physletb.2012.08.021`. [Online]. Available: `https://www.sciencedirect.com/science/article/pii/S0370269312008581`.

[3] T. A. Collaboration, "Observation of a new particle in the search for the standard model higgs boson with the ATLAS detector at the LHC," *Physics Letters B*, vol. 716, no. 1, pp. 1–29, 2012. DOI: `10.1016/j.physletb.2012.08.020`. [Online]. Available: `https://doi.org/10.1016%2Fj.physletb.2012.08.020`.

[4] M. McCullough, "Indirect model-dependent probe of the higgs self-coupling," *Physical Review D*, vol. 90, no. 1, 2014. DOI: `10.1103/physrevd.90.015001`. [Online]. Available: `https://doi.org/10.1103%2Fphysrevd.90.015001`.

[5] R. L. Workman and Others, "Review of Particle Physics," *PTEP*, vol. 2022, p. 083C01, 2022. DOI: `10.1093/ptep/ptac097`.

[6] P. Skands, "Introduction to QCD," in *Searching for New Physics at Small and Large Scales*, WORLD SCIENTIFIC, 2013. DOI: `10.1142/9789814525220_0008`. [Online]. Available: `https://doi.org/10.1142%2F9789814525220_0008`.

[7] M. H. Seymour, *Quantum chromodynamics*, 2010. arXiv: `hep-ph/0505192 [hep-ph]`.

[8] A. Pich, *Aspects of quantum chromodynamics*, 2000. arXiv: `hep-ph/0001118 [hep-ph]`.

[9] S. L. Glashow, "Partial-symmetries of weak interactions," *Nuclear physics*, vol. 22, no. 4, pp. 579–588, 1961.

[10] S. Weinberg, "A model of leptons," *Phys. Rev. Lett.*, vol. 19, pp. 1264–1266, 21 1967. DOI: `10.1103/PhysRevLett.19.1264`. [Online]. Available: `https://link.aps.org/doi/10.1103/PhysRevLett.19.1264`.

[11] *2010 European School of High-energy Physics: Raseborg, Finland 20 Jun - 3 Jul 2010. Proceedings of the 2010 European School of High-energy Physics, Raseborg, Finland, 20 Jun - 3 Jul 2010. 2010 European School of High-energy Physics*, CERN, Geneva: CERN, 2012. DOI: `10.5170/CERN-2012-001`. [Online]. Available: `https://cds.cern.ch/record/1226997`.

[12] J. Goldstone, A. Salam, and S. Weinberg, "Broken symmetries," *Phys. Rev.*, vol. 127, pp. 965–970, 3 1962. DOI: `10.1103/PhysRev.127.965`. [Online]. Available: `https://link.aps.org/doi/10.1103/PhysRev.127.965`.

[13] G. S. Guralnik, C. R. Hagen, and T. W. Kibble, "Broken symmetries and the goldstone theorem," *Advances in particle physics*, vol. 2, pp. 567–708, 1968.

[14] C. Collaboration, "A measurement of the higgs boson mass in the diphoton decay channel," *Physics Letters B*, vol. 805, p. 135 425, 2020. DOI: `10.1016/j.physletb.2020.135425`. [Online]. Available: `https://doi.org/10.1016%2Fj.physletb.2020.135425`.

[15] M. Aaboud *et al.*, "Search for top squarks in final states with one isolated lepton, jets, and missing transverse momentum in $\sqrt{s} = 13$ TeV pp collisions with the ATLAS detector," *Phys. Rev. D*, vol. 94, no. 5, p. 052 009, 2016. DOI: `10.1103/PhysRevD.94.052009`. arXiv: `1606.03903 [hep-ex]`.

[16] F. Englert and R. Brout, "Broken symmetry and the mass of gauge vector mesons," *Phys. Rev. Lett.*, vol. 13, pp. 321–323, 9 1964. DOI: `10.1103/PhysRevLett.13.321`. [Online]. Available: `https://link.aps.org/doi/10.1103/PhysRevLett.13.321`.

[17] P. W. Higgs, "Broken symmetries and the masses of gauge bosons," *Phys. Rev. Lett.*, vol. 13, pp. 508–509, 16 1964. DOI: `10.1103/PhysRevLett.13.508`. [Online]. Available: `https://link.aps.org/doi/10.1103/PhysRevLett.13.508`.

[18] G. S. Guralnik, C. R. Hagen, and T. W. B. Kibble, "Global conservation laws and massless particles," *Phys. Rev. Lett.*, vol. 13, pp. 585–587, 20 1964. DOI: `10.1103/PhysRevLett.13.585`. [Online]. Available: `https://link.aps.org/doi/10.1103/PhysRevLett.13.585`.

[19] "Search for the standard model higgs boson at LEP," *Physics Letters B*, vol. 565, pp. 61–75, 2003. DOI: `10.1016/s0370-2693(03)00614-2`. [Online]. Available: `https://doi.org/10.1016%2Fs0370-2693%2803%2900614-2`.

[20] T. T. W. Group, *Combined cdf and d0 search for standard model higgs boson production with up to 10.0 fb-1 of data*, 2012. arXiv: `1203.3774 [hep-ex]`.

[21] D. de Florian *et al.*, "Handbook of LHC Higgs Cross Sections: 4. Deciphering the Nature of the Higgs Sector," vol. 2/2017, 2016. DOI: `10.23731/CYRM-2017-002`. arXiv: `1610.07922 [hep-ph]`.

[22] S Dawson, R Tanaka, G Weiglein, M Weber, J Qian, *et al.*, *Handbook of lhc higgs cross sections: 1. inclusive observables*, en, 2011. DOI: `10.5170/CERN-2011-002`. [Online]. Available: `http://cds.cern.ch/record/1318996`.

[23] B Mellado, A. M. Cooper-Sarkar, M Kramer, G Ferrera, M. V. Garzelli, *et al.*, *Handbook of lhc higgs cross sections: 2. differential distributions*, en, 2012. DOI: `10.5170/CERN-2012-002`. [Online]. Available: `http://cds.cern.ch/record/1416519`.

[24] B. D. Micco, M. Gouzevitch, J. Mazzitelli, and C. Vernieri, "Higgs boson potential at colliders: Status and perspectives," *Reviews in Physics*, vol. 5, p. 100 045, 2020. DOI: `10.1016/j.revip.2020.100045`. [Online]. Available: `https://doi.org/10.1016%2Fj.revip.2020.100045`.

[25] B. D. Micco, M. Gouzevitch, J. Mazzitelli, and C. Vernieri, "Higgs boson potential at colliders: Status and perspectives," *Reviews in Physics*, vol. 5, p. 100 045, 2020. DOI: `10.1016/j.revip.2020.100045`. [Online]. Available: `https://doi.org/10.1016%2Fj.revip.2020.100045`.

[26] G. Aad *et al.*, "Combination of searches for Higgs boson pairs in pp collisions at $\sqrt{s} =13$ TeV with the ATLAS detector," *Phys. Lett. B*, vol. 800, p. 135 103, 2020. DOI: `10.1016/j.physletb.2019.135103`. arXiv: `1906.02025 [hep-ex]`.

[27] T. Cohen, D. E. Morrissey, and A. Pierce, "Electroweak baryogenesis and higgs signatures," *Physical Review D*, vol. 86, no. 1, 2012. DOI: 10.1103/physrevd.86.013009. [Online]. Available: https://doi.org/10.1103%2Fphysrevd.86.013009.

[28] T. Markkanen, A. Rajantie, and S. Stopyra, "Cosmological aspects of higgs vacuum metastability," *Frontiers in Astronomy and Space Sciences*, vol. 5, 2018. DOI: 10.3389/fspas.2018.00040. [Online]. Available: https://doi.org/10.3389%2Ffspas.2018.00040.

[29] N. Christensen, "Stochastic gravitational wave backgrounds," *Reports on Progress in Physics*, vol. 82, no. 1, p. 016903, 2018. DOI: 10.1088/1361-6633/aae6b5. [Online]. Available: https://doi.org/10.1088%2F1361-6633%2Faae6b5.

[30] C. Collaboration, "Combination of searches for Higgs boson pair production in proton-proton collisions at $\sqrt{s} = 13$ TeV," *Physical Review Letters*, vol. 122, no. 12, 2019. DOI: 10.1103/physrevlett.122.121803. [Online]. Available: https://doi.org/10.1103%2Fphysrevlett.122.121803.

[31] "Snowmass White Paper Contribution: Physics with the Phase-2 ATLAS and CMS Detectors," CERN, Geneva, Tech. Rep., 2022, All figures including auxiliary figures are available at https://atlas.web.cern.ch/Atlas/GROUPS/PHYSICS/PUBNOTES/AT PHYS-PUB-2022-018. [Online]. Available: https://cds.cern.ch/record/2805993.

[32] T. Behnke, J. E. Brau, B. Foster, J. Fuster, M. Harrison, *et al.*, *The International Linear Collider Technical Design Report - Volume 1: Executive Summary*, 2013. arXiv: 1306.6327 [physics.acc-ph].

[33] H. Baer, T. Barklow, K. Fujii, Y. Gao, A. Hoang, *et al.*, *The international linear collider technical design report - volume 2: Physics*, 2013. arXiv: 1306.6352 [hep-ph].

[34] M Aicheler, P Burrows, M Draper, T Garvey, P Lebrun, *et al.*, *A Multi-TeV Linear Collider Based on CLIC Technology: CLIC Conceptual Design Report* (CERN Yellow Reports: Monographs). Geneva: CERN, 2012. DOI: 10.5170/CERN-2012-007. [Online]. Available: https://cds.cern.ch/record/1500095.

[35] L. Linssen, A. Miyamoto, M. Stanitzki, and H. Weerts, *Physics and detectors at clic: Clic conceptual design report*, 2012. arXiv: 1202.5940 [physics.ins-det].

[36] T. C. S. Group, *Cepc conceptual design report: Volume 1 - accelerator*, 2018. arXiv: 1809.00285 [physics.acc-ph].

[37] M. Dong *et al.*, "CEPC Conceptual Design Report: Volume 2 - Physics & Detector," J. a. B. Guimarães da Costa *et al.*, Eds., 2018. arXiv: 1811.10545 [hep-ex].

[38] M. Mangano, P. Azzi, M. Benedikt, A. Blondel, D. A. Britzger, *et al.*, "FCC Physics Opportunities: Future Circular Collider Conceptual Design Report Volume 1. Future Circular Collider," CERN, Geneva, Tech. Rep. 6, 2019. DOI: 10.1140/epjc/s10052-019-6904-3. [Online]. Available: https://cds.cern.ch/record/2651294.

[39] M. Benedikt, A. Blondel, O. Brunner, M. Capeans Garrido, F. Cerutti, *et al.*, "FCC-ee: The Lepton Collider: Future Circular Collider Conceptual Design Report Volume 2. Future Circular Collider," CERN, Geneva, Tech. Rep. 2, 2019. DOI: 10.1140/epjst/e2019-900045-4. [Online]. Available: https://cds.cern.ch/record/2651299.

[40] M. Benedikt and F. Zimmermann, *FCC Feasibility Study Status*, 2023. [Online]. Available: https://indico.cern.ch/event/1202105/contributions/5423504/attachments/2659109/4606291/230605_FCC-FS-Status_ap.pdf.

[41] A. Abada *et al.*, "FCC-hh: The Hadron Collider: Future Circular Collider Conceptual Design Report Volume 3," *Eur. Phys. J. ST*, vol. 228, no. 4, pp. 755–1107, 2019. DOI: 10.1140/epjst/e2019-900087-0. [Online]. Available: https://cds.cern.ch/record/2653674.

[42] P. Janot, "Direct measurement of $\alpha_{QED}(m_Z^2)$ at the FCC-ee," *JHEP*, vol. 02, p. 053, 2016, [Erratum: JHEP 11, 164 (2017)]. DOI: 10.1007/JHEP02(2016)053. arXiv: 1512.05544 [hep-ph].

[43] J. A. Maestre, A. Blondel, M. Dam, and P. Janot, "The z lineshape challenge: Ppm and keV measurements," *The European Physical Journal Plus*, vol. 136, no. 8, 2021. DOI: 10.1140/epjp/s13360-021-01760-x. [Online]. Available: https://doi.org/10.1140%2Fepjp%2Fs13360-021-01760-x.

[44] C. Paus, *Precision Electroweak Measurements (FCCee)*, 2023. [Online]. Available: https://indico.cern.ch/event/1202105/contributions/5397070/attachments/2660249/4608264/fccee-ew-precision.pdf.

[45] P. Azzurri, *FCCee EW measurements at the Z pole and WW threshold*, 2017. [Online]. Available: https://indico.cern.ch/event/550509/contributions/2413294/attachments/1396834/2129754/EW_FCCee.pdf.

[46] P. Azzurri, "The w mass and width measurement challenge at FCC-ee," *The European Physical Journal Plus*, vol. 136, no. 12, 2021. DOI: 10.1140/epjp/s13360-021-02211-3. [Online]. Available: https://doi.org/10.1140%2Fepjp%2Fs13360-021-02211-3.

[47] Freya Blekman, *Top quark physics at FCC-ee*, 2019. [Online]. Available: https://indico.cern.ch/event/577856/contributions/3420352/attachments/1878810/3094850/top-fccee-eps2019-fblekman.pdf.

[48] J. Eysermans, *General Higgs performance overview*, 2023. [Online]. Available: https://indico.cern.ch/event/1202105/contributions/5396825/attachments/2661185/4610189/Higgs_Performance_FCCWeek_June2023.pdf.

[49] M. Selvaggi, *Detector Requirements from Physics*, 2023. [Online]. Available: https://indico.cern.ch/event/1202105/contributions/5396850/attachments/2659433/4606491/Detector%20Requirements%20from%20Physics.pdf.

[50] CERN Proceedings, *Cern proceedings, vol 1 (2017): Cern-binp workshop for young scientists in e+e- colliders*, en, 2017. DOI: 10.23727/CERN-PROCEEDINGS-2017-001. [Online]. Available: https://e-publishing.cern.ch/index.php/CP/issue/view/26.

[51] G. Gaudio, *The IDEA detector concept for FCC-ee and CepC*, 2022. [Online]. Available: https://agenda.infn.it/event/28874/contributions/169552/attachments/94486/129350/20220708_idea_gaudio.pdf.

[52] F. Reidt, "Upgrade of the ALICE ITS detector," *Nuclear Instruments and Methods in Physics Research Section A: Accelerators, Spectrometers, Detectors and Associated Equipment*, vol. 1032, p. 166632, 2022. DOI: 10.1016/j.nima.2022.166632. [Online]. Available: https://doi.org/10.1016%2Fj.nima.2022.166632.

[53] M Adinolfi, F Ambrosino, A Andryakov, A Antonelli, M Antonelli, *et al.*, "The tracking detector of the kloe experiment," *Nuclear Instruments and Methods in Physics Research Section A: Accelerators, Spectrometers, Detectors and Associated Equipment*, vol. 488, no. 1, pp. 51–73, 2002, ISSN: 0168-9002. DOI: `https://doi.org/10.1016/S0168-9002(02)00514-4`. [Online]. Available: `https://www.sciencedirect.com/science/article/pii/S0168900202005144`.

[54] A. M. Baldini, F. Cei, C. Cerri, S. Dussoni, L. Galli, *et al.*, *MEG upgrade proposal*, 2013. arXiv: `1301.7225 [physics.ins-det]`.

[55] M. Meucci, *MEG II experiment status and prospect*, 2022. arXiv: `2201.08200 [hep-ex]`.

[56] M. Dam, *Physics at FCC: Overviw of the FCC Conceptual Design Report*. [Online]. Available: `https://indico.cern.ch/event/789349/contributions/3298691/attachments/1805339/2946724/FCCCDR4March-MD.pdf`.

[57] P. Azzurri, G. Bernardi, S. Braibant, D. d'Enterria, J. Eysermans, *et al.*, "A special higgs challenge: Measuring the mass and production cross section with ultimate precision at FCC-ee," *The European Physical Journal Plus*, vol. 137, no. 1, 2021. DOI: `10.1140/epjp/s13360-021-02202-4`. [Online]. Available: `https://arxiv.org/abs/2106.15438`.

[58] J. de Blas, M. Cepeda, J. D'Hondt, R. Ellis, C. Grojean, *et al.*, "Higgs boson studies at future particle colliders," *Journal of High Energy Physics*, vol. 2020, no. 1, 2020. DOI: `10.1007/jhep01(2020)139`. [Online]. Available: `https://doi.org/10.1007%2Fjhep01%282020%29139`.

[59] J. Alwall, M. Herquet, F. Maltoni, O. Mattelaer, and T. Stelzer, "MadGraph 5: Going beyond," *Journal of High Energy Physics*, vol. 2011, no. 6, 2011. DOI: `10.1007/jhep06(2011)128`. [Online]. Available: `https://doi.org/10.1007%2Fjhep06%282011%29128`.

[60] T. Sjöstrand, S. Ask, J. R. Christiansen, R. Corke, N. Desai, *et al.*, "An introduction to PYTHIA 8.2," *Computer Physics Communications*, vol. 191, pp. 159–177, 2015. DOI: `10.1016/j.cpc.2015.01.024`. [Online]. Available: `https://doi.org/10.1016%2Fj.cpc.2015.01.024`.

[61] J. de Favereau, C. Delaere, P. Demin, A. Giammanco, *et al.*, "DELPHES 3: A modular framework for fast simulation of a generic collider experiment," *Journal of High Energy Physics*, vol. 2014, no. 2, 2014. DOI: `10.1007/jhep02(2014)057`. [Online]. Available: `https://doi.org/10.1007%2Fjhep02%282014%29057`.

[62] V. Bertone, M. Cacciari, S. Frixione, G. Stagnitto, M. Zaro, and X. Zhao, *Improving methods and predictions at high-energy e^+e^- colliders within collinear factorisation*, 2022. arXiv: `2207.03265 [hep-ph]`. [Online]. Available: `https://arxiv.org/abs/2207.03265`.

[63] S. P. Torbjörn Sjöstrand Peter Skands, *PYTHIA 8 Worksheet*, 2014. [Online]. Available: `https://pythia.org/download/pdf/worksheet8183.pdf`.

[64] A. Buckley, P. Ilten, D. Konstantinov, L. Lönnblad, J. Monk, *et al.*, "The HepMC3 event record library for monte carlo event generators," *Computer Physics Communications*, vol. 260, p. 107 310, 2021. DOI: `10.1016/j.cpc.2020.107310`. [Online]. Available: `https://doi.org/10.1016%2Fj.cpc.2020.107310`.

[65] R. Brun and F. Rademakers, "ROOT: An object oriented data analysis framework," *Nucl. Instrum. Meth. A*, vol. 389, M. Werlen and D. Perret-Gallix, Eds., pp. 81–86, 1997. DOI: `10.1016/S0168-9002(97)00048-X`.

[66] I. Antcheva, M. Ballintijn, B. Bellenot, M. Biskup, R. Brun, *et al.*, "Root—a c++ framework for petabyte data storage, statistical analysis and visualization," *Computer Physics Communications*, vol. 180, no. 12, pp. 2499–2512, 2009.

[67] A. Abulencia, D. Acosta, J. Adelman, T. Affolder, T. Akimoto, *et al.*, "Measurement of the inclusive jet cross section using the k_T algorithm in $p\bar{p}$ collisions at $\sqrt{s} = 1.96$ TeV," *Phys. Rev. Lett.*, vol. 96, p. 122 001, 12 2006. DOI: `10.1103/PhysRevLett.96.122001`. [Online]. Available: `https://link.aps.org/doi/10.1103/PhysRevLett.96.122001`.

[68] R. Gauld, A. Huss, and G. Stagnitto, *A dress of flavour to suit any jet*, 2022. arXiv: `2208.11138 [hep-ph]`.

[69] S. Bentvelsen and I. Meyer, "The cambridge jet algorithm: Features and applications," *The European Physical Journal C*, vol. 4, no. 4, pp. 623–629, 1998. DOI: `10.1007/s100520050232`. [Online]. Available: `https://doi.org/10.1007%2Fs100520050232`.

[70] M. Cacciari, G. P. Salam, and G. Soyez, "FastJet user manual," *The European Physical Journal C*, vol. 72, no. 3, 2012. DOI: `10.1140/epjc/s10052-012-1896-2`. [Online]. Available: `https://doi.org/10.1140%2Fepjc%2Fs10052-012-1896-2`.

[71] M. Boronat, J. Fuster, I. García, E. Ros, and M. Vos, "A robust jet reconstruction algorithm for high-energy lepton colliders," *Physics Letters B*, vol. 750, pp. 95–99, 2015. DOI: `10.1016/j.physletb.2015.08.055`. [Online]. Available: `https://doi.org/10.1016%2Fj.physletb.2015.08.055`.

[72] F. Boudjema, J. Fujimoto, T. Ishikawa, T. Kaneko, K. Kato, *et al.*, *Electroweak corrections for the study of the higgs potential at the lc*, 2005. arXiv: `hep-ph/0510184 [hep-ph]`.

[73] S. Dittmaier and M. Schumacher, "The higgs boson in the standard model—from LEP to LHC: Expectations, searches, and discovery of a candidate," *Progress in Particle and Nuclear Physics*, vol. 70, pp. 1–54, 2013. DOI: `10.1016/j.ppnp.2013.02.001`. [Online]. Available: `https://doi.org/10.1016%2Fj.ppnp.2013.02.001`.

[74] T. Han, Z. Liu, Z. Qian, and J. Sayre, "Improving Higgs Coupling Measurements Through ZZ Fusion at the ILC," *Phys. Rev. D*, vol. 91, p. 113 007, 2015. DOI: `10.1103/PhysRevD.91.113007`. arXiv: `1504.01399 [hep-ph]`.

[75] F. Boudjema, J. Fujimoto, T. Ishikawa, T. Kaneko, K. Kato, *et al.*, "Electroweak corrections to higgs production through ZZ fusion at the linear collider," *Physics Letters B*, vol. 600, no. 1-2, pp. 65–76, 2004. DOI: `10.1016/j.physletb.2004.08.062`. [Online]. Available: `https://doi.org/10.1016%2Fj.physletb.2004.08.062`.

[76] S. D. Vita, C. Grojean, G. Panico, M. Riembau, and T. Vantalon, "A global view on the higgs self-coupling," *Journal of High Energy Physics*, vol. 2017, no. 9, 2017. DOI: `10.1007/jhep09(2017)069`. [Online]. Available: `https://doi.org/10.1007%2Fjhep09%282017%29069`.

[77] V. Hirschi and O. Mattelaer, *Automated event generation for loop-induced processes*, 2015. arXiv: `1507.00020 [hep-ph]`.

[78] R. Frederix, S. Frixione, V. Hirschi, D. Pagani, H.-S. Shao, and M. Zaro, "The automation of next-to-leading order electroweak calculations," *Journal of High Energy Physics*, vol. 2018, no. 7, 2018. DOI: 10.1007/jhep07(2018)185. [Online]. Available: https://doi.org/10.1007%2Fjhep07%282018%29185.

[79] V. Bertone, M. Cacciari, S. Frixione, and G. Stagnitto, "The partonic structure of the electron at the next-to-leading logarithmic accuracy in QED," *Journal of High Energy Physics*, vol. 2020, no. 3, 2020. DOI: 10.1007/jhep03(2020)135. [Online]. Available: https://doi.org/10.1007%2Fjhep03%282020%29135.

[80] S. Frixione, "On factorisation schemes for the electron parton distribution functions in QED," *Journal of High Energy Physics*, vol. 2021, no. 7, 2021. DOI: 10.1007/jhep07(2021)180. [Online]. Available: https://doi.org/10.1007%2Fjhep07%282021%29180.

[81] S. Frixione, "Initial conditions for electron and photon structure and fragmentation functions," *Journal of High Energy Physics*, vol. 2019, no. 11, 2019. DOI: 10.1007/jhep11(2019)158. [Online]. Available: https://doi.org/10.1007%2Fjhep11%282019%29158.

[82] A. Collaboration, *Measurement of the inclusive $t\bar{t}$ production cross section in the lepton+jets channel in pp collisions at $\sqrt{s}$= 7 TeV with the ATLAS detector using support vector machines*, 2022. arXiv: 2212.00571 [hep-ex].

[83] J. Eysermans, P. Azzi, G. Bernardi, S. Braibant-Giacomelli, V. Diolaiti, *et al.*, *Higgs mass and cross-section studies using ZH recoil with $Z \to \mu\mu$*, 2021. [Online]. Available: https://indico.cern.ch/event/995850/contributions/4415989/attachments/2272945/3860610/ZHRecoilAnalysis_FCCWeek_29062021.pdf.

[84] F. Maltoni, D. Pagani, A. Shivaji, and X. Zhao, "Trilinear higgs coupling determination via single-higgs differential measurements at the LHC," *The European Physical Journal C*, vol. 77, no. 12, 2017. DOI: 10.1140/epjc/s10052-017-5410-8. [Online]. Available: https://doi.org/10.1140%2Fepjc%2Fs10052-017-5410-8.

[85] D. H. Perkins, *Introduction to High Energy Physics*, 4th ed. Cambridge University Press, 2000. DOI: 10.1017/CBO9780511809040.

Appendices

Appendix A

Breit-Wigner formula

For a collision process between two particles, A and B, forming exclusively a unstable state 'X', which then decay to the final state, C and D, where the width of the intermediated state is not to high compare to their own mass, the cross-section is given by the **Breit-Wigner** formula [85]:

$$\sigma_{i \to X \to f} = \sigma_{max} \frac{\Gamma_i \Gamma_f}{(E - E_R)^2 + \Gamma^2/4} \tag{A.1}$$

where:

- $\Gamma_{i/f} \to$ *partial width* of the intermediate state to the initial/final state;

- $\Gamma \to$ *full width* of the unstable particle;

- $E \to$ center of mass energy;

- $E_R \to$ rest mass energy of the resonance;

- $\sigma_{max} \to$ peak cross-section;

and if the final state particles decay into other particles, additional Branching Ratio are add to the formula.

Appendix B

Total Width problem

In Appendix A, we presented the Breit-Wigner formula, which MadGraph5 uses to calculate the cross-section. This formula shows us a total width dependency, which can cause problems if the width is too small.

In this appendix, we show an example of where this happened. Consider the two processes: e+ e- > e+ e- h (eeHee) and the same one plus the Higgs decay into a b-quark pair (eeHee, H > b b) at the models' sm (MG5 default model) and loop_qcd_qed_sm-with-b-mass[1] at $\sqrt{s}$=240 GeV. For each process in each model, we change the Higgs total width between the two values mentioned above.

Process Γ_H	eeHee	eeHee, H > b b
3.58 MeV	7.90	10.9
6.38 MeV	7.91	6.38

Table B.1: Cross-sections [pb] at **loop_qcd_qed_sm-with-b-mass** model.

Process Γ_H	eeHee	eeHee, H > b b
3.58 MeV	7.88	10.9
6.38 MeV	7.88	6.52

Table B.2: Cross-sections [pb] at **sm** model.

From Tables B.1 and B.2, it is possible to notice that for small values of the total width, the process with the Higgs decay exhibits a higher cross-section than the same process without the decay, which makes no logic. With this in mind, it was decided, for this study, to use the default Γ_H from the sm MG5.

---

[1]It is the same model as the loop_qcd_qed_sm but at the four flavor scheme.

Appendix C

Flowchart

```
                        ┌─────────────────┐
                        │    Level 1:     │
                        │  N_jets  N_e    │
                        └─────────────────┘
     ATLAS overlap removal       │
                        ┌─────────────────┐
                        │    Level 2:     │
                        │  N_jets  N_e    │
                        └─────────────────┘
                                 │
  p_T^jets ≥25GeV      ◇ p_T cuts ◇      p_T^min=0
┌──────────────┐                          ┌──────────────┐
│  Level 4:    │◄──────           ──────►│  Level 3:    │
│ N_Jets N_lept│       p_T^lept ≥20 GeV  │ N_Jets N_lept│
└──────────────┘                          └──────────────┘
```

Level 1:
N_{jets} N_e

ATLAS overlap removal

Level 2:
N_{jets} N_e

$p_T^{jets} \geq 25 \text{GeV}$

p_T cuts

$p_T^{min}=0$

Level 4:
N_{Jets} N_{lept}

Level 3:
N_{Jets} N_{lept}

$p_T^{lept} \geq 20$ GeV

Level 5:
N_{b-jets},
N_{e+}, N_{e-}

B-tag: 1 or 3
$Q(e^-)= -1$, $Q(e^+)= 1$

B-tag: 1 or 3
$Q(e^-)= -1$, $Q(e^+)= 1$

Min: $1e^{\pm}$ and 2 b-jets

Level 6
All variables

Recoil Mass cuts

Level 7:
All variables

MET< 40 GeV

Level 8:
All variables

M_{Inv}^{ee} cuts

Level 9:
All variables

Level 10:
All variables

$M_{ee} \in [80,100]$ GeV

$M_{ee} > 100$ GeV

Appendix D

IDEA b-tag

The output file from Delphes is a ROOT file, where the data is stored in a ROOT tree format [66]. ROOT tree objects are constructed from the particles generated by a Monte-Carlo generator and from objects produced by Delphes, such as jets, electrons, muons, and others. Each object is split into different branches, and their properties (like p_T, mass, electric charge, b-tag, and others) can be accessed by the branch's ramifications called leaves.

The b-tag variable (BTag) in the Jet branch can store up to 32 bits. It allows the user to specify the BitNumber parameter, which points to the position where that bit will be stored. By default, its value is 0, meaning the b-tag bit is stored in the first position. From Fig D.1, it is indicated that BTag=$\{0, 1, 2, 3\}$. Turning this into binary language
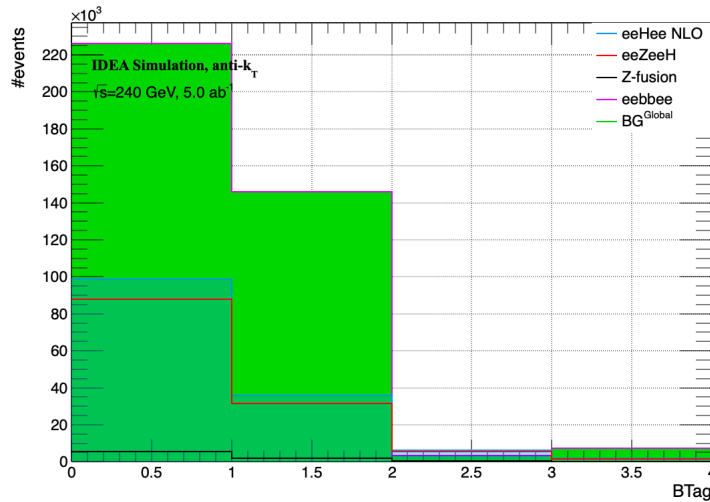

Figure D.1: IDEA card b-tag.

and using the BitNumber 0, it is possible to understand the meaning behind the BTag values:
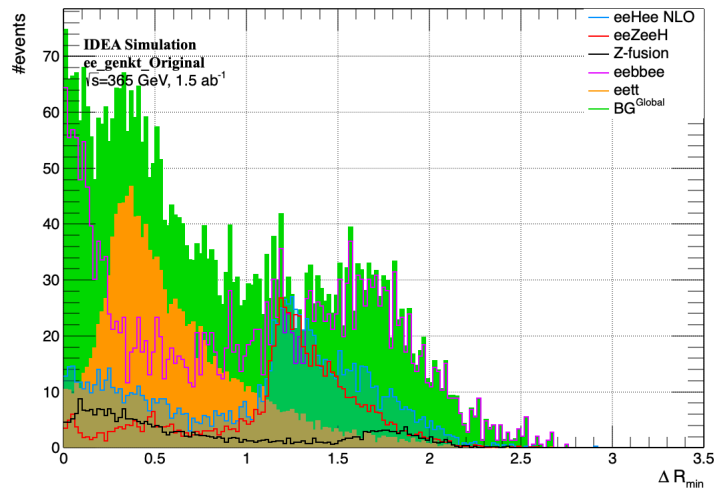
75

BTag value	0	1	2	3
BTag binary	00	01	10	11
(bit 0) & BTag	F	T	F	T

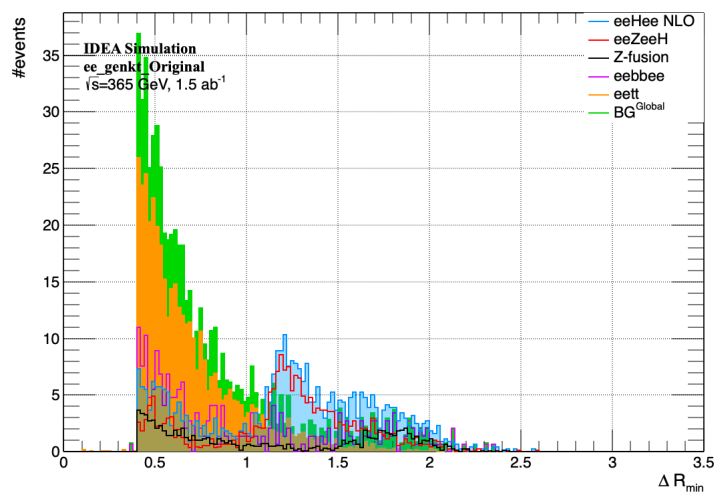Table D.1: B-tagging in bit-wise code with T for True and F for false.

Table D.1 shows its binary representation for each BTag value. As the default Bit-Number was used, the b-tag bit is contained in the first position. In order to select the b-jets, the BTag should be 1 or 3.
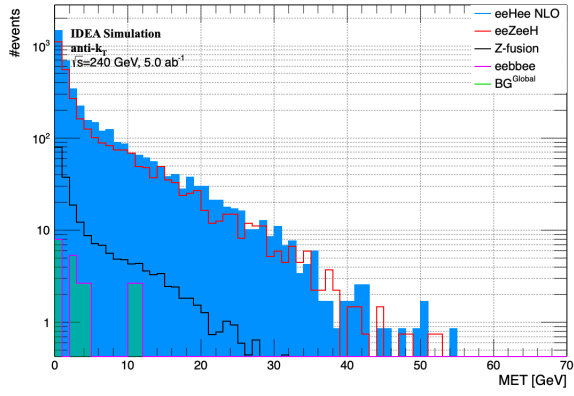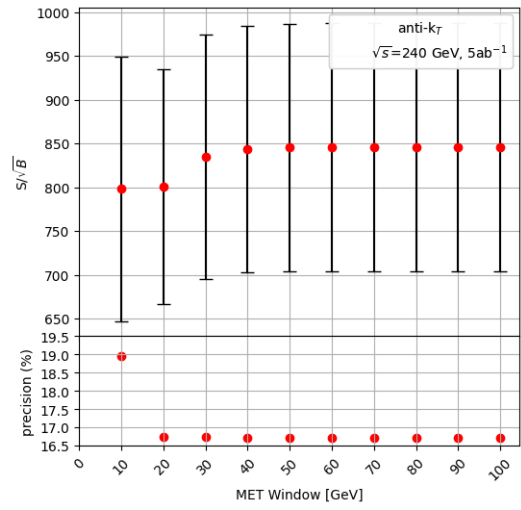
Appendix E

Extra Plots

(a)

(b)

Figure E.1: ΔR_{min}, before (a) and after (b) OR, at 365 GeV using the *ee_genkt_Original*.

(a)

(b)

Figure E.2: MET distribution after the m_{recoil} cut at 240 GeV (left) and its significance as a function of MET's window (right).